July 2017

Vitreous Gel Physics

Svetlana Morozova
University of Massachusetts - Amherst

VITREOUS GEL PHYSICS

A Dissertation Presented

by

SVETLANA MOROZOVA

Submitted to the Graduate School of the

University of Massachusetts Amherst in partial fulfillment

of the requirements for the degree of

DOCTOR OF PHILOSOPHY

May 2017

Polymer Science and Engineering

VITREOUS GEL PHSYICS

A Dissertation Presented

by

SVETLANA MOROZOVA

Approved as to style and content by:

_____

Murugappan Muthukumar, Chair

_____

David Hoagland, Member

_____

Alfred Crosby, Member

_____

Sarah Perry, Outside Member

_____

Bryan Coughlin, Department Head

Polymer Science and Engineering

DEDICATION

To all the failure

ACKNOWLEDGMENTS

One summer afternoon in 2010 I took a bus to Boston to spend an afternoon at MIT with Professor George Benedek. I wanted to work with him during that summer break. I had a great time discussing how cataracts form and eating delicious imported chocolate, which Professor Benedek mentioned he enjoyed daily with lunch. I did not end up working for him, but the idea of contributing to the physical understanding of vision lingered. My summer afternoon conversation became my reason for applying to Polymer Science and Engineering department to work for Professor Muthukumar. I'm so glad it worked out. I'm really thankful for his encouragement and his support on this project throughout all these years. He guided me and empowered me as a scientist and a human being and I'll be forever grateful.

I knew about the department because of my earlier work with Professor Crosby. As a freshman back in 2008, he let me into his lab and developed my love for research and applied science. He has also been a fantastic committee member, with extremely helpful suggestions and encouragements. My other committee members, Professor David Hoagland and Professor Sarah Perry have been just as supportive. I am really grateful for their crucial input and discussions, and for the great conversations.

I would also like to thank my family, my sister Olga and my parents. Olga is there for me probably too often, and I learn something from her every day, whether it is about the world or about myself. And I could not have made any accomplishments without my parents. My dad is always there for interesting lateral thinking discussions and my mom is the most understanding and encouraging person I know. I hope they live forever.

And thank you friends, you know who you are. But Ryan especially for your discussions and your time.

ABSTRACT

VITREOUS GEL PHYSICS

MAY 2017

SVETLANA MOROZOVS, B.A., CORNELL UNIVERSITY

M.S., UNIVERSITY OF MASSACHUSETTS AMHERST

Ph.D., UNIVERSITY OF MASSACHUSETTS AMHERST

Directed by: Professor Murugappan Muthukumar

Chances are you know someone who wears glasses. Glass-wearers like me know very well that vision should not be taken for granted. All we have to do is to take our glasses off and the world becomes one big, disorienting blur. Problems only worsen with age. Vision is only possible through macromolecular principles, charged components, adhesion, and transfer of light and ions. The transparent vitreous, which fills the posterior cavity of the eye, is incredibly engineered. The charged polyelectrolyte hyaluronic acid (HA) network swells to maintain the pressure in the eye, while stiff collagen type II bundles help absorb any external mechanical shock. Our investigations have contributed to a few key developments related to the physical properties of the vitreous:

(1) The stiff collagen network that supports the soft gel network is self-assembled from single triple-helix collagen proteins. Electrostatic interactions drive this assembly, such that the size and concentration are optimized at physiological salt concentrations. The width of the assemblies remarkably changes from 60 nm to 800 nm with only a 50 mM change in the salt concentration.

(2) A soft (~ 2 - 200 Pa) negative polyelectrolyte network swells to support the microscopic and tough collagen bundles. The equilibrium swelling behavior and the response to external manipulation is driven by the charged components of the gel. We have developed a way to determine the thermodynamic quantities responsible for this phenomenon, such as the chemical miss-match parameter of the backbone, the ionizability of the network, and the Poisson's ratio. We show that these parameters are enough to predict the equilibrium linear-elastic elasticity of polyelectrolyte gels for a range of strand lengths and salt concentrations.

(3) Finally, using these principles, in collaboration with Dr. Paul Hamilton, and Dr. Nathan Ravi at Washington University, We have developed a new synthetic injectable vitreous substitute for use as a novel double-network therapeutic material.

The vitreous can phase-separate and detach from the retina. This disease is poorly studied and has few treatment options. By studying biomimetic models of the vitreous in vitro, we hope to understand vision-related diseases, the mechanism for collagen fiber formation, intrinsic soft tissue properties, and to formulate therapeutic materials.

TABLE OF CONTENTS

Page

LIST OF TABLES

Table Page

LIST OF FIGURES

Figure Page

CHAPTER 1

INTRODUCTION

1.1 The Vitreous

The vitreous is a gelatinous tissue that fills the posterior cavity of the eye[1]. It is responsible for maintaining the shape of the eye, absorbing shock, and transmitting light and ions. Although the exact composition is much more complex, the hydrogel can be simply thought of as two dilute, interpenetrating networks. The glycosaminoglycan, hyaluronan (hyaluronic acid, HA), forms a highly entangled mesh that swells to suspend a network of collagen fibers (Figure 1.1). HA is ionizable, which contributes to the internal osmotic pressure. Collagen spontaneously forms rigid microscopic fibers, which reinforce the soft hyaluronan network. The concentration of the structural components is reported to be remarkably low, between 0.4-0.7 mg/mL. The rest of the vitreous, which is composed of primarily water and dissolved salts, glucose, proteins, and other small molecules accounts for 99.94% of the volume.[2] The gel's transport and optical properties are related to the density of the structural components. Less dense networks are more clear and porous than more dense ones. The swelling and dynamic response properties are linked to the internal pressure of the system, which is dictated by the structure of collagen, charge density, cross-link density, and hydrophobicity of HA.[2–6]

The exact thermodynamic quantities such as HA backbone hydrophobicity and fraction of ionized monomers are unknown for the vitreous. Theoretically in thermodynamic equilibrium with an external solution these quantities, along with chain length, are directly responsible for the elasticity [7–11]. In general the theoretical description of polyelectrolyte gel swelling has never been fully experimentally tested.[12–14] Below we describe an experimental method based on established equilibrium theories, which we use to determine thermodynamic properties for highly swollen

polyelectrolyte gels in high salt solutions. We show that these parameters fully describe the elasticity of hyaluronic acid gels as a function of salt concentration and strand length.

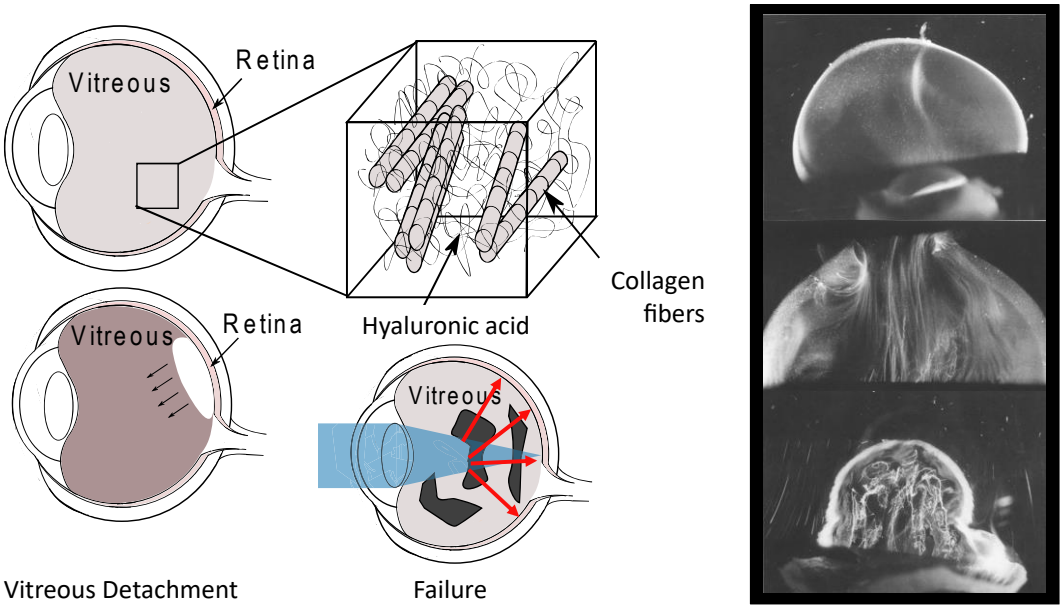

Figure 1.1: The vitreous. The vitreous is a swollen hydrogel responsible for maintaining the shape of the eye. It is composed of an anionic polysaccharide, hyaluronic acid, and rigid collagen fibers. With age the vitreous loses its structure as pockets of inhomogeneities grow. This can result in a total detachment of the vitreous or obscured vision. On the right- micrograph of vitreous at three stages in life: 4 years old, 20 years old, and 84 years old. As the tissue ages, it becomes more inhomogeneous.[6]

Collagen type II assembles into large, well ordered fibers.[15–19] The fibers reinforce the soft HA matrix and provide mechanical integrity.[20–24] The mechanism and criteria of this process is still debated. It has been shown that ionic strength and pH are crucial for the equilibrium structure, but the role of electrostatics in this mechanism is still largely neglected.[17,19,25–29] Using both experimental evidence and numerical modeling, we investigate the role of pair-wise electrostatic interactions between two parallel collagen triple helices. We find that the phase space and structure are very sensitive to the pH, ionic strength, and temperature of the solution.

The mutual interactions between collagen and HA also contributes to the physical properties of the tissue.[7,30,31] The strength of the interactions, if they are present, will influence the swelling behavior of HA and structure collagen fibers. We investigate the swelling equilibrium,

collagen structure and kinetics as a function of the composite composition and find that the two networks do not interact strongly and are mutually reinforcing in an additive way.

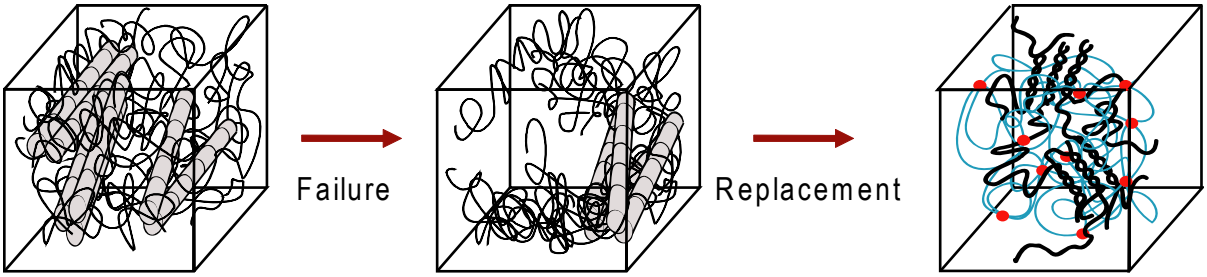

Figure 2.2: As the vitreous ages, it fails. The failure results in permanent inhomogeneities, which are responsible for obstruction and eventually loss of vision. One solution is to synthesize therapeutic tissues to replace the failed vitreous.

The fundamental insights into the origins of the physical properties of the vitreous is important for the development of synthetic therapeutic materials.[1,32–38] The vitreous fails eventually as we get older (Figure 1.1). The tissue loses its structural integrity and separates from the back of the eye.[39] This causes inhomogeneities that scatter light and obscure vision as well as more serious diseases such a retinal detachment. The mechanism of failure is unknown, and long-lasting therapeutic materials that could replace the broken vitreous do not yet exist.[1,4] Using the fundamental insights from our systematic investigations of each component of the vitreous, we create a list of necessary criteria for the replacement injectable tissue (Figure 1.2).

1.2 Hyaluronic Acid

The modulus of HA polyelectrolyte networks depends on the structure of the gels, just as it does for dry rubber networks.[7–11] For a rubber, the conformational entropy of a polymer strand between cross-links is lower upon stretching. This results in a restoring force, causing the polymer chains to contract back to their original configuration. The restoring force is proportional to the elastic shear modulus (G'), which depends on the density of crosslinks or alternatively, the inverse of N:[7,11,40]

$$G' = \frac{k_B T}{N v_1} \qquad (1.2.1)$$

with v_1 the solvent molecular volume, k_B the Boltzmann constant, and T the absolute temperature. Upon network swelling, the mechanical properties become complicated. Added solvent decreases the modulus of polyelectrolyte gels. The dependence on the polymer concentration follows from classical arguments as:[7,11,14,40]

$$G' = \frac{k_B T}{N v_1}\left(\alpha_0^2 \phi^{\frac{1}{3}} - \frac{\phi}{2}\right) \qquad (1.2.2)$$

where α_0 is a parameter that references a hypothetical un-deformed state in which the network obeys Gaussian chain statistics, $\alpha_0^3 = \phi_0 = V_d/V_0$, where V_d is the volume of a dried network, and V_0 is the volume of an undeformed network with Guassian chain statistics.

For polyelectrolyte gels, the equilibrium swelling volume fraction is a function of both the solvent quality and the salt concentration of the solution. Due to the added complexity, this field has attracted several theoretical arguments relying on scaling arguments. The elastic behavior of gels has been historically described by Eq. 1.2.2.[12–14,41] The abundant use of the $\frac{1}{3}$ power law is due to its simplicity; the law is universal and the pre-factor depends only on the molecular structure of the network. These trends are experimentally checked by several groups, but do not predict the modulus dependence on the volume fraction for highly swollen polyelectrolyte networks as a function of the salt concentration.

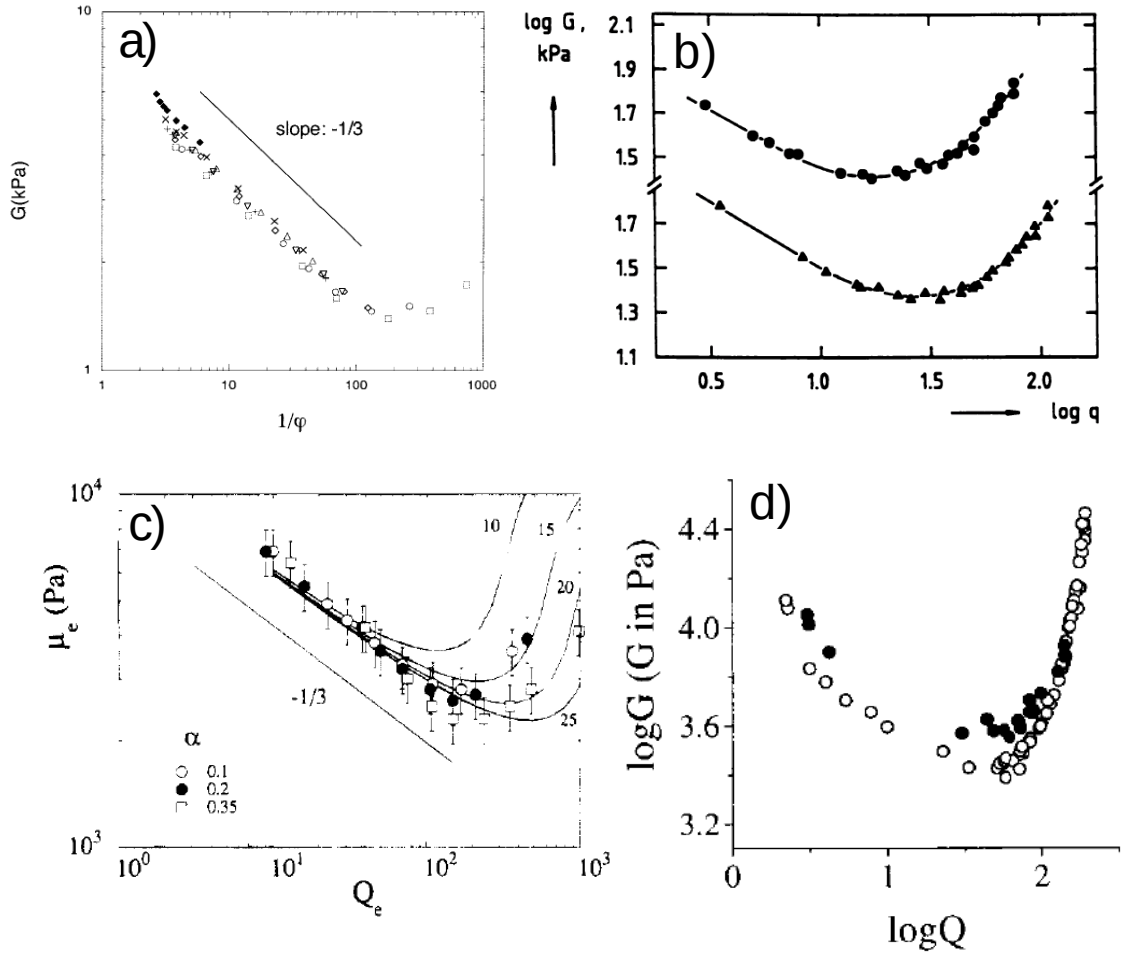

Figure 3.3: The swelling of polyelectrolyte networks. a) The shear modulus G as a function of one over the polymer volume fraction ϕ reproduced from Horkey et al.[14] The modulus decreases with swelling for more dense gels, and increases as the gels swell beyond $\frac{1}{\phi} > 100$. b)-d) Similar graphs reproduced from Oppermann et al.[42], Skouri et al.[41], and Zaroslov et al.[43]. With $q = 1/\phi$ and $\mu = G$.

Recently there has been a push for more sophisticated descriptive trends that consider the ionizability of the backbone and the salt concentration. For example, Barrat *et al*[44]., Skouri *et al.*[41], and Rubinstein *et al.*[45], predict that the modulus will have several power law dependence regimes for different solution conditions and extension ratios. Notably, Rubinstein *et al.*[45] predict a new scaling theory for the modulus of polyelectrolyte gels in the weak stretching regime. For low salt concentrations, they expect the modulus to be a power law of the ionization and the volume fraction: $G' \sim \left(\frac{1}{\alpha}\right)^{\frac{2}{7}} \phi^{\frac{5}{6}}$. In high salt concentrations, they expect the modulus to have a

slightly weaker dependence on the polymer volume fraction, $G' \sim \phi^{\frac{7}{12}}$. However, these results do not agree with experimental findings, as tested by Nisato *et al.*[12,13] .Nisato *et al.* find that the modulus scales close to $\left(\frac{1}{\alpha}\right)^{\frac{2}{7}}$, and close to $\phi^{\frac{1}{3}}$ for higher volume fractions and is a decreasing function at lower salt concentrations for a constant N. Other findings suggest different scaling relations. For example Skouri *et al.*[41] postulate their own power laws for gels in high salt in swelling equilibrium. They predict that in these conditions, $G' \sim \phi^2$, which agreed well with their experimental data.

Similar scaling laws have been proposed in an effort to predict the response of polyelectrolyte networks in the context of dynamic light scattering (DLS). The relaxations of the density fluctuations measured from the scattered intensity are related linearly to the longitudinal modulus (K), and inversely to the solvent friction against the polymer strands (f), $D = K/f$.[41,44,46–49] Barrat *et al.*[44] predict that in the case of high salt, $K \sim \frac{\phi^2}{I}$ .They show that at lower salt concentrations (I) when the electrostatic interaction length is comparable to the mesh size of the gel, counterion pressure dominates and increases the tension of gel strands. At higher salt concentrations, they predict that the modulus and correspondingly the elastic diffusion (D), will scale as the inverse ionic strength. Skouri *et al.*[41] predict that the elastic diffusion coefficient measured with DLS is related to the volume fraction as $\phi^{\frac{1}{2}}$ .Similarly Rasmark *et al.*[49] and Joosten *et al.*[46] have shown experimental evidence that at a constant salt concentration $D \sim \phi^{\frac{1}{2}}$ for polyelectrolyte gels.

In general scaling laws are idealized and only predict an increasing function of the modulus with the volume fraction of polymer. In practice, it has been observed by several groups that at lower ionic strength, there is a cross-over salt concentration after which G' becomes a decreasing function of the volume fraction (Figure 1.3).[12,41–43,50] At low ionic strengths the

polyelectrolyte gels are reported to swell, yet stiffen. This has been thought of as non-Gaussian behavior and is usually described by an inverse Langevin function.[11] However, the finite extensibility regime description has never been effectively fit to experimental measurements.[41]

1.3 Collagen

Collagens are identified by their specific biochemistry. Out of the 28 different collagen, collagen types I, II, III, V, and XI self-assemble into larger structures in a staggered way.[15,16,19,51] Typically, the fibrous proteins are formed from the hydrogen bonding of three peptides into a triple helix. Collagens type I, II, III, V, and XI each have a unique structure.[16,18,52–59] Collagen type II is a triple helix with three left-handed helical chains that are hydrogen-bonded together in a right-handed manner. The rigid molecule is 1.5 nm in diameter and 300 nm in length. Every chain contains the repeating amino acid sequence Gly-X-Y, with Pro and Hyp mainly occupying the X and Y positions. The glycine residues are responsible for the stability of the triple helix through hydrogen bonds (N-H •• O=C), and are buried, facing into the triple helix axis and away from the solvent. In contrast, the rest of the X and Y residues are highly exposed to the solvent and are responsible for maintaining the collagen fiber structure.[19,58] Approximately 18% of the overall amino acid sequence is ionizable and the isoelectric point of collagen type II is at pH 8.5. Charged residues such as Lys, Glu, and Arg are asymmetrically distributed along the molecule, but about 40% of every Gly-X-Y triplet has at least one positive or negative charge at pH 7.4.[28,60] Positive residues are more often found in the Y positions, and the negative residues are more often found in the X positions.[28,61,62] At the ends of each collagen type II triple helix, there are globular domains. These domains are mainly responsible for covalently linking the collagen fiber assemblies together, and are unnecessary for fiber formation.[63]

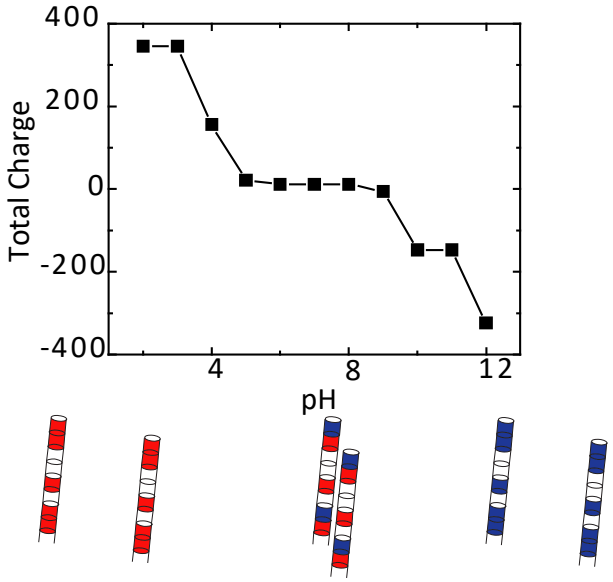

Figure 4.4: The theoretical surface charge of a collagen type II triple helix based on amino acid sequence. At low pH, the helices are homogeneously positively charged, at high pH the fibers are homogeneously negatively charged. At intermediate pH, both positive and negative residues are ionizable, so that total charge is zero.

The surface charge of collagen type II triple helices is highly dependent on the pH of the solution (Figure 1.4). From the theoretical titration curve based on the pKa's of the charged residues, at pH below 4, the collagen triple helix surface charge density is composed entirely of positive charges, with a linear charge density of 1.15 positive charges/nm in the helical region. And at pH above 10, the collagen triple helix surface charge is negative, with a charge density of 1.08 negative charges/nm in the helical region. At intermediate pH ($4 < pH < 10$), the collagen type II triple helix region is decorated with both positive and negative ions. At pH 4, there are 345 positive and 324 negative ionized residues. At pH 5, there are 345 positive and 324 negative ionized residues. At pH 6-8, there are 336 positive and 324 negative residues. At pH 9 the charge density becomes negative, with 318 positive and 324 negative ionized residues. In the intermediate pH conditions, the proteins assemble into fibers at salt concentrations below 250 mM.

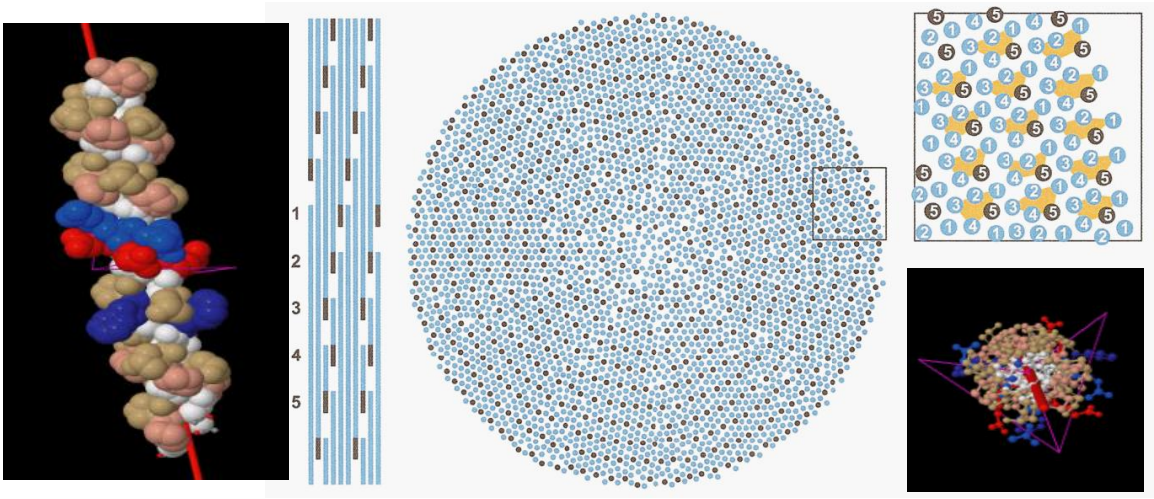

Figure 5.5: The structure of collagen type II triple helices and their organization within a fiber. Collagen type II triple helices are supported by hydrogen bonding inside the helix, with charged amino acids symmetrically arranged facing the surrounding solution. In the fiber, they self-organize in a staggered quasi-hexagonal way as reproduced from Hulmes et al.[15,16]

Collagen is organized in a very specific way within the fibers. The triple helices wind around each other in a staggered, quasi-hexagon way (Figure 1.5). From x-ray scattering data, Hulmes *et al.*[15],Ottani *et al.*[56], Orgel *et al.*[53], Holmes *et al.*[64], and Antipova *et al.*[54] have deduced the radial and lateral order for collagen fibers. Laterally, collagen triple helices associate in a staggered way. For collagen type II, Antipova et al.[54] have found that the stagger length is 234 animo acids. Hulmes et al.[15] have found that radially, the triple helices are arranged in lateral unit cells which contain five collagen triple helices in cross-section. They have found a radial periodicity outward from the center that corresponds to ~4 nm, which they attribute to the concentric organization collagen bundles. Confirming data by Holmes *et al.*[64], and Ottani *et al.*[56], Hulmes *et al.*[15] argue that collagen molecules are arranged in a helical way, such that the molecules are titled obliquely in plane, oriented 30º to the fiber surface.

Despite its importance, the data describing the phase space and mechanism for collagen type II assemblies is incomplete, and is limited to comparisons to a much more widely studied protein, collagen type I.[19,65–67] There are substantial differences between collagen type I and

collagen type II. Although both molecules share the Gly-X-Y triplet motif, each has a unique amino acid composition and surface charge density. The total number of ionizable groups for collagen type I triple-helix is 535 amino acids, and for collagen type II is 669 amino acids. Collagen type I has a lower isoelectric point at pH 7.2, whereas collagen type II is net neutral at pH 8.5. The nucleation and growth rates of fibers are faster for collagen type II, suggesting that the intermolecular interactions are much stronger for this molecule than for collagen type I.[66] The single-molecule collagen densities in the fibers formed are also distinct. Collagen type I fibers have a smaller mass per unit length, and are generally thinner. This distinction also suggests a difference in the interactions between the triple-helices in the fiber formation.[66]

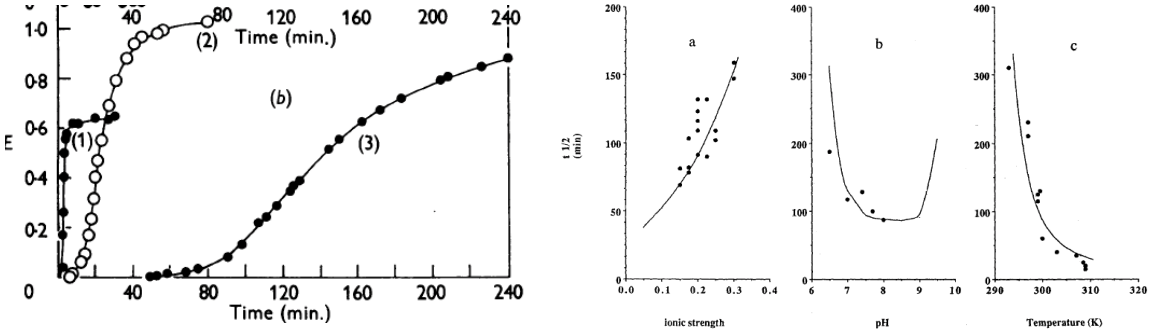

Figure 6.6: Previous results on the salt, pH, and temperature dependence of collagen fiber formation. a) Data from Wood et al.[17] showing the total light scattered from the solution (*E*) for (1), (2), and (3), corresponding to 0.13, 0.23 and 0.31 [I]. With added salt collagen fiber formation is slowed. b) Data from Wallace et al.[27] showing theoretical fits to fiber formation kinetics as a function of ionic strength, pH and temperature. The kinetics are fastest at low ionic strengths, highest temperatures, and intermediate pH.

Although still debated, the most widely accepted mechanism for collagen fiber assemblies is that it is an entropically driven process. This mechanism is based entirely on collagen type I data, and is assumed analogous to other fiber forming collagens.[19] As the collagen single molecules come together, bound water on the surface is released, which increases the entropy.[25,63,68–71] By observing the temperature dependence of the critical concentration for fibril formation, Kadler *et al*.[63], and Cooper *et al*.[25] estimated both the enthalpic and entropic contributions to collagen type I fiber formation. They found that the total Gibbs free energy of

fiber formation at a fairly high ionic strength of 0.2 M is -13 kcal/mol, with the enthalpic contribution of 53 kcal/mol, and the entropic contribution of 220 kcal/mol. While Cooper *et al.*[25] did notice a solubility increase of collagen type I triple helices with salt concentration, he was unable to quantify the effect due to experimental limitations. By measuring how the solution osmotic pressure changes the inter-molecular distance Leikin *et al.*[70] found that there are two types of forces that could possible contribute to the stability of collagen fibers. The short range repulsive force is balanced with a long range attractive force, which is enhanced with temperature, and is responsible collagen self-assembly. They attribute these forces to the entropic release of water during collagen fiber formation. Cassel *et al.*[68] and Silver *et al.*[72] make a distinction between lateral and linear growth of collagen type I fibers, and argue that the two growth steps have different mechanisms. The smaller microfibers assemble through electrostatic interactions, and then bundle together in an entropically – driven process. Both steps are essential for stabilizing collagen fibers. Since the kinetics data and phase space data for collagen type II fibril formation is limited, there has been no discussion on specifically collagen type II mechanism in the literature.

Most collagen researchers agree that electrostatic interactions contribute to the fibrillization process, but the specifics of this process are unclear and are still controversial. It has been postulated that the relatively high ampiphilic charge density on the surface of collagen type I triple helices has to contribute to the intermolecular ion-pair formation.[27,61,72–75] The large number of charged residues has made it difficult to isolate and determine specific interactions. From rheological studies at lower ionic strengths, at which there is no evidence of fiber formation, Cassel *et al.* noted an increased viscosity from relative to soluble collagen triple helix solutions.[68] This evidence for extremely thin microfibers in non-ionic solutions suggests some ionic complexation for collagen type I. From the collagen type I amino acid sequence Silver *et al.*[72] proposed a mechanism for the charged pair interactions in collagen fibers, suggesting that there

are on the order of 40 -150 intermolecular charge pairs in physiological conditions that can stabilize collagen assembles. In contrast, in 1990, Wallace *et al.*[27] estimated the contribution of the charged pair interactions for collagen type I assemblies by applying a model for the total electrostatic interactions present in the assembly (Figure 1.6). He estimated that the driving force will be due to ion-pairs between two collagen molecules and that the electrostatic contribution to the overall bulk energy of formation is about -1 kcal/mol, or one charged pair per triple-helix pair. Still, no such data is available for collagen type II assemblies.

1.4 Vitreous detachment

The strategy to create a more appropriate vitreous substitute is to synthesize injectable biocompatible hydrogels, the components of which are inspired by the natural vitreous. The ideal vitreous substitute must be composed of a charged polymer network which mimics hyaluronan and is responsible for providing osmotic pressure to the gel, and a rigid fibrous network which reinforces the swollen charged matrix just as collagen does in the eye. The modulus of these composite hydrogel materials must be close to the native tissue, which is reported to have a modulus of 50-120 Pa in vitro.[1] The volume fraction of the structural components must also match that of the native tissue, since this value directly impacts the transport properties of gels.[76]

In the past few decades, there has been a push to research more appropriate vitreous substitutes. These are outlined in detail in several reviews by Swindle *et al.*[1], Baino[33], Chirila *et al.*[34,35], Donati *et al.*[36], and Kleinberg *et al.*[37] Substitutes have been created using natural polymers, natural and synthetic polymer composites, collagen, hyaluronic acid, gellan gum, and various synthetic polymers in an effort to mimic the vitreous structure.[33–37] None of these has been able to match the necessary criteria for an injectable biomimetic hydrogel materials suitable for a vitreous substitute.

Inspired by the structural composition of the natural tissue, gellan gum has been suggested as a vitreous substitute in a hyaluronan matrix.[77,78] Gellan is a linear heterocopolysaccharide that is negatively charged and composed of glucose, glucuronic acid, and rhamnose in a 2:1:1 ratio.[79,80] The polysaccharide spontaneously gels at lower temperatures due to the formation of associating helixes in the presence of cations.[81,82] The fibrous content created by the associated helices is very reminiscent of collagen fibers and support the hyaluronan network. In addition, gellan gels are great candidates for injectable materials, since at higher temperatures the associated helices melt and can be passed through a syringe needle. Suri *et al.*[77,78] report that the cell viability of hyaluronan-gellan gels was greater than 90%, but due to a lack of chemical cross-linking and degradation the materials are not suitable for long-term substitutes. Du *et al.*[83] have synthesized thiolated gellan molecules which are able to form both chemically and physically cross-linked networks. They were found to be injectable and biocompatible, but have yet to be used in the design of injectable vitreous substitutes.

To mimic the hyaluronan network component of the vitreous, methylacrylamide (MAm) gels have been copolymerized with bismethacryloylcystamine (BMAC) disulfide crosslinkers.[84–87] The redox-active disulfide bonds enable versatility in handling and injection of the gels. The copolymers are easily dialyzed to get rid of toxic monomer content and the gels are formed in the eye through the natural oxidative environment in the ocular cavity. Swindle *et al.*[84,87] have confirmed that the gels are easily cross-linkable in situ, are bio-compatible, and optically similar to the natural tissue. In another study, however, they have shown that the dynamic response of copolymer did not match the vitreous, and that the modulus is more than 5 times higher than the bovine vitreous modulus. Although the material has been shown to be biocompatible and injectable, the lack of ionizable monomers leads to stiffer gels.

The copolymerization of methylacrylic acid (MAA) to the MAm-BMAC gels has shown a great impact on the polymer chain flexibility. Liang *et al.*[88] have demonstrated that the

composition of the resulting copolymer of MAm, MAA, and BMAC can be changed to match the modulus of the vitreous. In this case, however, even though increasing the number of cross-links leads to stiffer gels, the increased amount of BMAC decreases the biocompatibility of these networks. In a cell line, the cells much more favored the 2%BMAC gels, which are too soft to be compatible vitreous substitutes, with a modulus of 1.5-45 Pa.[88] The fibrous content, corresponding to the collagen structures in the vitreous is lacking in these materials, and must be incorporated to improve their function.

CHAPTER 2

POLYELECTROLYTES AND POLYAMPHOLYTES IN AQEOUS SOLUTIONS

2.1 Introduction

The vitreous is a swollen composite gel, the components of which have ionizable monomers.[5] The polysaccharide hyaluronic acid has a carboxylic acid moiety at each monomer. In aqueous solutions, the carboxylic acid is full negatively charged above the pH of the log of its acid dissociation constant (pK_a=2.8). Similarly, a single collagen triple helix peptide has 3180 amino acids, including positively ionizable amino acids such as arginine (pK_a = 12.1), histidine (pK_a = 6.04), and lysine (pK_a = 10.57), and including negatively ionizable amino acids such as aspartic acid (pK_a = 3.71), and glutamic acid (pK_a = 4.15). The isoelectric point of collagen type II is at pH 8.3. At this pH, the number of positively ionizable amino acids equals the number of negatively ionizable amino acids. The presence of charges on both of the major components of the vitreous establishes long-range interactions in aqueous solutions and strongly contributes to the physical properties of each macromolecule such as the chain stiffness and attraction potential.[89–94] The addition of salt to the aqueous solutions reduces the range of the interactions. By changing the ionic strength of the solution, we probe the strength of electrostatic interactions in dilute systems.

2.2 Debye – Hückel screening effects and chain dimensions in salt solutions

Occupying 99.9% of the volume, water is arguably the most important component of the vitreous. The solvent contributes in a crucial way to the electrostatic potential between the charged species of the tissue. The dielectric constant (ϵ) of water is close to 80 in physically relevant temperatures, which allows for long range electrostatic interactions.[90] Therefore, upon addition of a small amount of electrolyte such as NaCl or $CaCl_2$, the molecules completely dissociate into cations and anions. For our discussion, the charges of the ions are denoted as $z_a e$, where z_a is the

electronic charge of ion a and e is unit of one electronic charge. In water each dissociated ion feels a potential from other ions, but no matter how much salt is added, the bulk charge is always zero, such that the system is completely electrically neutral.[90]

The electrical potential at a radial distance $r = |\boldsymbol{r}|$, $\psi(\boldsymbol{r})$, is simply given by the Coulomb law:[90]

$$\psi(\boldsymbol{r}) = \frac{ez_a}{4\pi\epsilon_0\epsilon}\frac{1}{r} \qquad (2.2.1)$$

where ϵ_0 is the permittivity of a vacuum. The electrostatic energy of a pair of ions a and b then is:[90]

$$u_{ab}(\boldsymbol{r}) = \frac{e^2 z_a z_b}{4\pi\epsilon_0\epsilon}\frac{1}{r} \qquad (2.2.2)$$

The electrostatic potential and energy of dissociated ions in solution decay slowly as $\sim 1/r$ and are therefore long range. The prefactor $\frac{e^2 z_a z_b}{4\pi\epsilon_0\epsilon}$ sets the magnitude of the energy. When compared to thermal energy, estimated as $k_B T$, a convenient measure of the length of the electrostatic interactions emerges. This length scale is defined as the Bjerrum length, l_B:[90]

$$l_B = \frac{e^2 z_a z_b}{4\pi\epsilon_0\epsilon k_B T} \qquad (2.2.3)$$

At a distance smaller than l_B electrostatics dominate all interactions, and at distances beyond l_B, thermal motion is a more dominant force. It is this length scale that makes water a unique medium. The relatively high dielectric constant sets the Bjerrum length at aroun 0.7 nm in physiologically relevant temperatures. In water, as long as the salt concentration is low enough, electrostatic forces contribute highly.

The addition of salt adjusts the range of electrostatic interactions. As the number of anions and cations increases in solution, so does the molar ionic strength of the solution, defined as:[90,95–97]

$$I = \frac{1}{2}\sum_{i=1}^{n} n_i z_i^2 \qquad (2.2.4)$$

where n_i is the molar concentration of the ith ion. This equation accounts for the velancy of electrolytes in solution. Generally multivalent ions such as calsium or magnesium contribute strongly to the ionic strength of the solution.

As soon as there is more than one cation and one anion in solution, the electrostatic potential an electrolyte feels is no longer pair-wise. A single ion is correlated to all the other ions in solution and all the possible interactions have to be considered. The electric potential around a labeled ion in an electrolyte solution at a distance $\boldsymbol{r}$ is determined by the Poisson's equation:[90,96–98]

$$\nabla^2\psi(\boldsymbol{r}) = -\frac{\rho(\boldsymbol{r})}{\epsilon_0\epsilon} \qquad (2.2.5)$$

where $\rho(\boldsymbol{r})$ is the local charge density of ions at a radial distance $\boldsymbol{r}$. Following previous derivations, if we assume a Boltzmann distribution of the number of ions, Eq. 2.2.5 becomes:[90,96–98]

$$\nabla^2\psi(\boldsymbol{r}) = -\frac{e}{\epsilon_0\epsilon}\sum_a z_a\, n'_a \exp[-\frac{ez_a}{k_BT}\,\psi(\boldsymbol{r})] \qquad (2.2.6)$$

where n'_a is the local number concentration of charged species a. For dilute salt concentrations, Eq. 2.2.6 is simplified by taking into account only the leading terms of the exponential for small enough $-\frac{ez_a}{k_BT}\,\psi(\boldsymbol{r})$. In this case, the electrostatic potential $ez_a\psi(\boldsymbol{r})$ is small in comparison to the thermal energy. This approximation leads to the linearized Poisson-Boltzmann equation, also known as the Debye-Hückel equation:[90,96–98]

$$\nabla^2\psi(\boldsymbol{r}) = -\frac{e}{\epsilon_0\epsilon}\sum_a z_a\, n'_a \left[1 - \frac{ez_a}{k_BT}\,\psi(\boldsymbol{r}) + \cdots\right] \qquad (2.2.7)$$

or taking advantage of net neutrality, which forces the sum of all ionic species to equal 0:

$$\nabla^2\psi(\boldsymbol{r}) = \kappa^2\psi(\boldsymbol{r}) \qquad (2.2.8)$$

where the constant

$$\kappa^2 = \frac{e^2}{\epsilon_0 \epsilon k_B T} \sum_a z_a^2 \, n'_a \qquad (2.2.9)$$

The constant κ^2 is related to the polarizability of the solvent as well as the ionic strength of the solution. Using Eq. 2.2.4, we rewrite the above expression:

$$\kappa = \sqrt{\frac{e^2 I}{\epsilon_0 \epsilon k_B T}} \qquad (2.2.10)$$

κ is directly related to the square root of the ionic strength of the solution. Following previous derivations, for a point-like charged ion in water, the solution to Eq. 2.2.8 is:[90,96]

$$\psi(r) = \frac{e z_i}{4\pi\epsilon_0 \epsilon} \frac{e^{-\kappa r}}{r} \qquad (2.2.11)$$

For a more physical ion with a finite radiua a, the potential for $r > a$ is:[90,96]

$$\psi(r) = \frac{e z_i}{4\pi\epsilon_0 \epsilon} \frac{e^{-\kappa(r-a)}}{r(1+\kappa a)} \qquad (2.2.12)$$

For a charged cylinder of radius a, the potential for $r > a$:[90,93,94,96]

$$\psi(r) = \frac{e z_i}{4\pi\epsilon_0 \epsilon} \frac{K_0(\kappa r)}{\kappa a K_1(\kappa a)} \qquad (2.2.13)$$

where K_n is the modified Bessel function of the *n*th order.

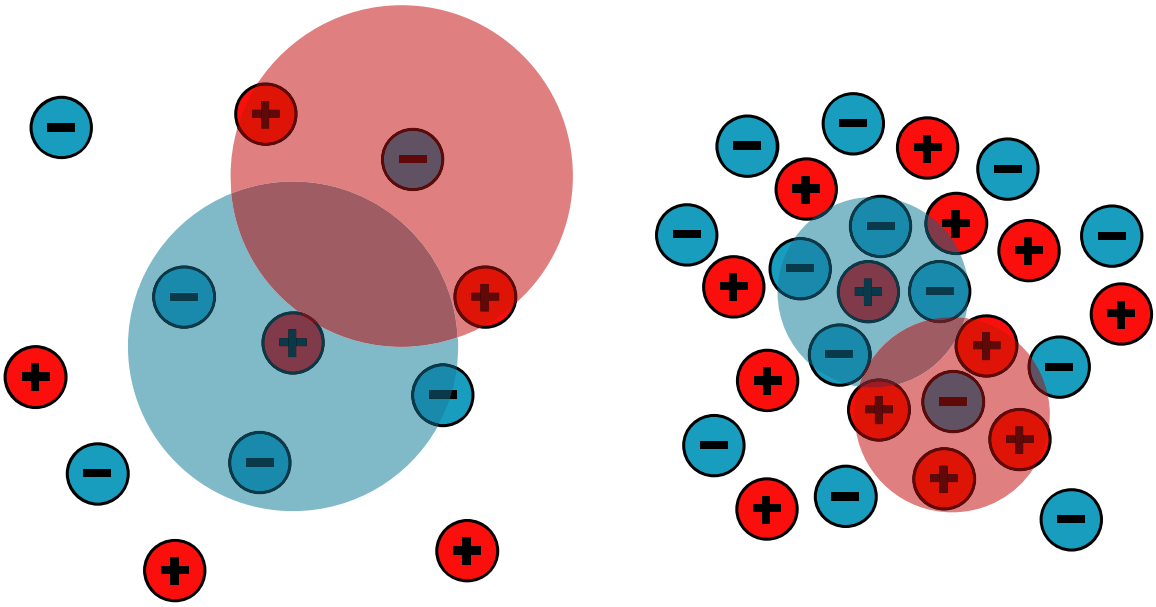

Figure 7.1: A schematic of the prediction of Debye-Hückle theory on effect of ionic strength on the range of electrostatic interactions in solutions. At low ionic strength, electrostatics are long range, at high ionic strength the interactions are screened.

For all three cases, regardless of geometric complications, the potential decays as a function of the radial distance r. The characteristic lengthscale of this decay is set by the screening length, κ^{-1}. As derived above, this lengthscale is proportional to $\frac{1}{\sqrt{I}}$ and $\frac{1}{\sqrt{l_B}}$. While l_B is the property of the solvent, κ^{-1} is the property of the salt solution. The effect of ionic strength on the range of electrostatic interactions is demonstrated in Figure 2.1. The electrostatic interaction between ions in dilute salt concentrations is long range. With the addition of salt, κ^{-1} decreases as salt screens electrostatic intrections.

Ionic strength changes the magnitude of the work needed to bring two ions together from infinity to a distance d apart, and is used to probe electrostatic interactions in solution. Molecules that repel each other strongly have a higher osmotic pressure at low salt concentrations. Alternatively, molecules that attrack each other experience a higher magnitude of attraction at lower salt concentrations. At higher salt concentrations, the interactions are screened.

2.3 Dipoles in aqueous solutions

For proteins such as collagen at pH 8.3, the total charge on the surface of the molecule is zero, but dipolar electrostatic interactions are still possible. For a zero total charge, Q, the Taylor expansion of the electric potential for an arbitrary bounded charge distribution confined to some region R is:[99]

$$\psi(\boldsymbol{r}) = \frac{1}{4\pi\epsilon_0}\int dV' \frac{\rho(\boldsymbol{r}')}{|\boldsymbol{r}-\boldsymbol{r}'|} \qquad (2.3.1)$$

$$\psi(\boldsymbol{r}) \sim \frac{1}{4\pi\epsilon_0}\int dV' \rho(\boldsymbol{r}') \left[\frac{1}{\boldsymbol{r}} + \frac{\hat{r}\cdot\boldsymbol{r}'}{\boldsymbol{r}^2} + \cdots\right] \qquad (2.3.2)$$

$$\psi(\boldsymbol{r}) \sim \frac{1}{4\pi\epsilon_0}\frac{Q}{r} + \frac{1}{4\pi\epsilon_0}\frac{\hat{r}\cdot\boldsymbol{p}}{r^2} \qquad (2.3.3)$$

where $\boldsymbol{p}$ is the vector that represents the dipole moment of magnitude $2z_a ed$ if the oppositely charged ions are a distance d apart. For a dipole Q is zero, but the electrostatic potential is still present and long range ($1/r^2$).

A single collagen molecule has both positively and negatively ionizable amino acids. As mentioned in Chapter 1, below pH 4, a collagen type II triple helix is strongly positively charged. Above pH 10, the molecule is strongly negatively charged. At intermediate pH values, both positive and negative amino acids are ionized, but the total charge is close to zero. We therefore expect that the interaction between two parallel collagen triple helices to be a function of pH and salt concentration, as illustrated in Figure 2.2. At extreme pH, the triple helices repel each other. At intermediate pH, the total charge is close to zero, but dipole-dipole interactions are responsible for an overall attraction between collagen triple helices.

The electrostatic energy between two collagen triple helices located parallel to each other a distance r_{ij} away at extreme pH is estimated from the arguments presented in the previous section. The energy between two homogeneously charged cylinders is:

$$u_{ij}(r_{ij}) = \frac{e^2 z^2}{4\pi\epsilon_0\epsilon} \frac{K_0(\kappa r)}{\kappa a K_1(\kappa a)} \qquad (2.3.4)$$

Since the number of interacting charges on the cylinders is large and equal for both molecules, the energy is large and positive. In these conditions, collagen triple helices strongly repel each other.

At intermediate pH, the total charge density is close to zero. It is not trivial to calculate the attractive dipole-dipole Debye-Hückel interaction for these molecules analytically, but we can estimate the interaction numerically by summing all the possible amino acid interactions between the molecules. In this case, each radially symmetric group of amino acids on the triple helix is estimated as a homogeneously charged cylinder, such that the interaction between two cylinders a distance r_{ij} apart is:

$$u_{ij}(r_{ij}) = \frac{e^2 z_i z_j}{4\pi\epsilon_0\epsilon} \frac{K_0(\kappa r)}{\kappa a K_1(\kappa a)} \qquad (2.3.5)$$

For the right distribution of charged amino acids, we expect the sum of all the possible interactions to be large and negative. Their attraction becomes less negative as salt is added to the solution, as illustrated in Figure 2.2. At high enough salt, the interactions are screened.

Just like proteins, zwitterions are connected dipoles and are able to interact in solution. For zwitterions however, the dipole is not along the backbone of the macromolecule, but at each monomer, oriented either towards or away from the backbone. The orientation as well as the local dielectric constant determines the self-assembly behavior of these molecules. For further discussion on this topic, see Appendix A.[100–102]

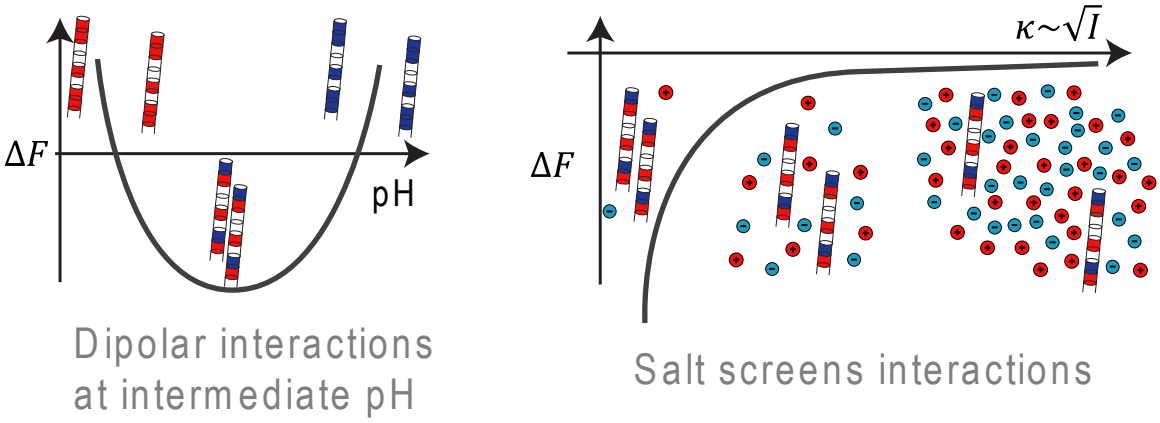

Figure 8.2: The expected effect of pH and ionic strength on the electrostatic interaction of two collagen type II triple helices. At extreme pH collagen is homogeneously charged and the molecules repel each other. At intermediate pH the molecules attract, and the attraction is screened with added salt as predicted by Debye-Hückel theory.

2.4 Polyelectrolyte networks and the importance of Donnan potential

The vitreous of the eye is supported by a swollen, negatively charged hyaluronic acid (HA) network. As for all polyelectrolyte networks, the degree of ionization (α), the hydrophobicity of the backbone (χ), the number of monomers between crosslinks (N), and concentration of added salt (c_s) control the material response.[7,10,11,103]

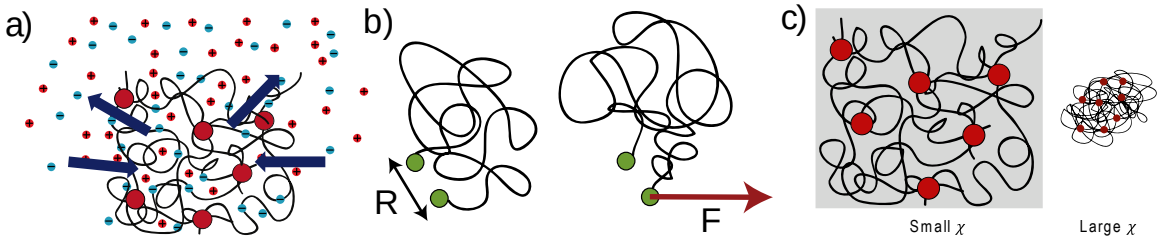

Figure 9.3: Internal pressure is responsible for the equilibrium swelling polymer fraction of polyelectrolyte gels. a) The free counterions present in polyelectrolyte gels have to remain in the network to preserve net neutrality. To alleviate the chemical potential difference between the interior of the gel and the external solution, the gel swells. This effect is not as strong in high salt

Gels exist in a swollen state, so that the total volume of the network consists of both polymer and solvent. The volume fraction of the polymer inside the network, $\phi = \frac{V_{polymer}}{V_{solvent}+V_{polymer}}$, defined as the volume of polymer divided by the total volume of solvent and polymer, describes

the inverse degree of swelling. For lower ϕ the network is highly swollen, and for higher ϕ the network is more concentrated with polymer.

The swelling of polyelectrolyte gels is due to the internal pressure of the network.[7,14,104] The thermodynamic properties that contribute to this pressure are: (i) the number of ionized charges on the backbone, (ii) the hydrophobicity of the backbone, and (iii) the length of the chain between crosslinks. The effects of each pressure is illustrated in Figure 2.3.

In equilibrium, the pressure due to counterions,Π_{ion}, is balanced by the pressure due to the elasticity of the polymer chains, Π_{el}, and the mixing of the polymer chains with the solvent, Π_{mix} such that:

$$\Pi_{tot} = 0 = \Pi_{ion} + \Pi_{el} + \Pi_{mix} \qquad (2.4.1)$$

The pressure from the counterions, in the units of the Boltzmann constant, k_B and absolute temperature, T, is described by Donnan equilibrium: [10,92,103,105]

$$\frac{\Pi_{ion}}{k_B T} = \sqrt{\alpha^2 \phi^2 + 4v_1^2 c_s^2} - 2v_1 c_s \qquad (2.4.2)$$

Where α is the degree of ionization, c_s is the number of salt ions, and v_1 is the molar volume of the solvent. Gels in equilibrium with pure (ion-free) water swell due to the chemical potential of counterions. To preserve net neutrality, these counterions can't leave the network, so the gel swells in response to the salt concentration imbalance between the interior of the gel and the surrounding solvent. The addition of permanent ions to the network always increases the degree of swelling. The addition of salt to the solution reduces the Donnan pressure, such that the gels do not swell as much as in ion-free water. The effect is schematically shown in Figure 2.3a. There is a chemical potential equilibrium of ions between the interior of the gel and the surrounding solvent. If the concentration of ions inside the gel is higher that the solvent, the gel will swell to reduce that imbalance.

The pressure due to the elastic nature of the network is related to the number of monomers between the crosslinks, N:[7,11,92,103]

$$\frac{\Pi_{el}}{k_B T} = -\frac{1}{N}(\alpha_0^2 \phi^{\frac{1}{3}} - \frac{\phi}{2}) \qquad (2.4.3)$$

Here α_0 is parameter that references a hypothetical un-deformed state in which the network obeys Gaussian chain statistics, $\alpha_0^3 = \phi_0 = V_d/V_0$, where V_d is the volume of a dried network, and V_0 is the volume of an undeformed network with Guassian chain statistics. Qualitatively, the elasticity of the network depends only on the length of the strands between crosslinks and the volume fraction of the polymer. If the strands are short (N small), the network is tight and does not swell as much as when the strands are long (N large). The effect of elasticity is schematically presented in Figure 2.3b. The force required to pull an end of a polymer chain is proportional to the entropy of the chain. Chains with higher entropy (N large such that the number of possible configurations is large), are easier to pull. Conversely, chains with a small N are stiffer.

The final pressure for a polymer network takes into account the hydrophobicity of the backbones of the chains, in terms of the chemical mismatch parameter, χ:[7]

$$\frac{\Pi_{mix}}{k_B T} = -\ln(1-\phi) - \phi - \chi\phi^2 \qquad (2.4.4)$$

For really swollen gels, $\phi \ll 1$, and Eq. 2.4.4 reduces to $\left(\frac{1}{2} - \chi\right)\phi^2$. For χ really close to 0.5, the equation becomes third order in ϕ, and does not contribute considerably to the total internal pressure. For favorable solvents, when χ is considerably less than 0.5, the gel swells as compared to when χ is large. The effect of solvent quality is illustrated in Figure 2.3c. For small χ the interaction between the polymer and the solvent is favorable and overcomes the polymer-polymer interactions. In this case, the gels swell. For large χ values, the opposite is true. Polymer-polymer interactions are much stronger than polymer-solvent interactions and the gels remain dense.

Combining Eq. 2.4.1-2.4.4, we rewrite the internal pressure of a hydrogel in equilibrium:

$$\Pi_{tot} = 0 = \sqrt{\alpha^2\phi^2 + 4v_1^2c_s^2} - 2v_1c_s - \frac{1}{N}(\alpha_0^2\phi^{\frac{1}{3}} - \frac{\phi}{2}) - \ln(1-\phi) - \phi - \chi\phi^2 \qquad (2.4.5)$$

From which we can arrive with an expression for the structural component of the gel, the number of monomers between crosslinks, N:

$$N = \frac{\left(\alpha_0^2\phi^{\frac{1}{3}} - \frac{\phi}{2}\right)}{-\ln(1-\phi) - \phi - \chi\phi^2 + \sqrt{\alpha^2\phi^2 + 4v_1c_s} - 2v_1c_s} \qquad (2.4.6)$$

For some gels, Eq. 2.4.6 is not completely accurate, since it does not take into account structural defects such as potential loops or dangling ends. Flory (1943) has modified the theory to allow for such ineffective chains, arriving at:[7–9]

$$\frac{1}{N'} = \frac{1}{N}\left(1 + \frac{2M_c}{M}\right) \qquad (2.4.7)$$

where M_c is the molecular weight between crosslinks, and M is the molecular weight of the polymers prior to cross-linking.

The modulus of polyelectrolyte gels depends on the structure of the gels, just as it does for dry rubber networks. For a rubber, the conformational entropy of a polymer strand between cross-links is lower upon stretching. This results in a restoring force, causing the polymer chains to contract back to its original configuration. The restoring force is proportional to the elastic shear modulus (G'), which depends on the density of crosslinks or alternatively, the inverse of N:[7,11]

$$G' = \frac{k_BT}{N'v_1} \qquad (2.4.8)$$

with v_1 the solvent molecular volume, k_B the Boltzmann constant, and T the absolute temperature. Upon network swelling, the mechanical properties become complicated. Added solvent decreases the modulus of polyelectrolyte gels by decreasing the density of cross-links. The dependence on the polymer concentration follows from classical arguments as:[7,11,103]

$$G' = \frac{k_B T}{N' v_1} \alpha_0^2 \phi^{\frac{1}{3}} = G'^* \alpha_0^2 \phi^{\frac{1}{3}} \qquad (2.4.9)$$

where G'^* is the shear modulus of a dry network. G' can be fully expressed in terms of just the polymer volume fraction by substituting Eq. 2.4.9 into Eq. 2.4.5 and solving for G':

$$G' = \frac{k_B T}{v_1}\left(-\ln(1-\phi) - \phi - \chi\phi^2 + \sqrt{\alpha^2\phi^2 + 4v_1^2 c_s^2} - 2v_1 c_s - \frac{\phi}{2N'}\right) \qquad (2.4.10)$$

For the case of highly swollen gels, $\phi \ll 1$, for any salt concentration, Eq.2.4.10 reduces simply to:

$$G' = \frac{k_B T}{v_1}\left(\left(\frac{1}{2} - \chi\right)\phi^2 + \sqrt{\alpha^2\phi^2 + 4v_1^2 c_s^2} - 2v_1 c_s\right) \qquad (2.4.11)$$

At higher salt concentrations, the $4v_1^2 c_s^2$ term dominates in the square root and Eq. 2.4.11 reduces to:

$$G' = \frac{k_B T}{v_1}\left(\frac{1}{2} - \chi + \frac{\alpha^2}{4v_1 c_s}\right)\phi^2 \qquad (2.4.12)$$

For high ionic strengths and low volume fraction, if we independently measure the volume fraction, ϕ, and the shear modulus, G', we experimentally determine the thermodynamic properties χ and α and predict the full dynamic response as a function of the salt concentration for highly-swollen polyelectrolyte gels.

The derivation of the dynamic light scattering of gels is similar. The elastic diffusion coefficient measured from the relaxation time of the gels as a function of the dynamic light scattering angle is equal to the longitudinal modulus, K, divided by the viscous friction coefficient of the gel strands against the solvent, f:[44,47]

$$D = K/f \qquad (2.4.13)$$

The longitudinal modulus is related to the shear modulus through the Poisson's ration, v:

$$K = \frac{2(1-v)}{1-2v} G' \qquad (2.4.14)$$

and the fiction coefficient is known to scale with the volume fraction of the gel as $\phi^{1.5}$:[76]

$$f = A\phi^{1.5} \qquad (2.4.15)$$

With A as a scaling factor. Combining Eq. 2.4.12-2.4.15 we arrive at an expression for the elastic diffusion coefficient as a function of the volume fraction of the gel, the ionic strength, Poisson's ratio, hydrophobicity, and ionizability of the gel strands:

$$D = \frac{2(1-v)}{1-2v}\left(\frac{k_B T}{A v_1}\right)\left(\frac{1}{2} - \chi + \frac{\alpha^2}{4 v_1 c_s}\right)\phi^{0.5} \qquad (2.4.16)$$

We expect the elastic diffusion coefficient to be a monotonically increasing function of the polymer volume fraction of a gel at a constant salt concentration. For a constant polymer volume fraction, the diffusion coefficient will scale inversely with the number of salt ions present in the equilibrating solution.

2.5 Summary

Electrostatic interactions contribute to the physical properties of both of the major components of the vitreous in the eye and should be considered and studied further. The vitreous is highly swollen with water. The solvent is polar and facilitates long range electrostatic interactions and the dissociation of electrolytes. For collagen molecules in neutral pH conditions, dipolar interactions are expected to contribute to the attractive interactions between molecules. With increased salt the interaction is screened.

Dissociated ions also contribute to the swelling of polyelectrolyte networks. The presence of free counterions in the volume of the gel leads to a Donnan equilibrium pressure. In low salt concentrations this pressure is responsible for swelling the gels of a constant N. At higher salt concentrations, the Donnan pressure has a lower contribution to swelling. This effect is expected

to contribute to both the elastic shear modulus of hydrogels as well as the elastic diffusion coefficient of these systems as measured by dynamic light scattering.

CHAPTER 3

LIGHT SCATTERING

3.1 Introduction

The components of the vitreous are small by design. The tissue has to remain optically clear. As a consequence, the size and shape of the macromolecules cannot be resolved with a microscope and we must rely on indirect measurements like light scattering experiments. Dynamic and Static Light scattering (DLS and SLS) are powerful tools for probing structure of nanometer length scales in solutions. The incident electromagnetic laser beam is scattered from the solution of macromolecules if the solute has a different index of refraction than the solvent.[96,106] The intensity of the scattered beam measured by a detector a distance r away is related to the difference in polarizability of the macromolecule and the solvent and increases with the size and concentration. The wavelength of light is between 400 and 650 nm, which is ideal to study the Rayleigh scattering of macromolecules smaller than 100 nm for a range of scattering angles. Small angle light scattering (SALS) is used to determine the structure of larger molecules or the mesh size of more dense, solutions of overlapping polymers or particles. Dynamic light scattering results from density fluctuations of the solution. As polymers diffuse in and out of the scattering volume or as gel strands oscillate about some equilibrium, the intensity fluctuates. The relaxation rate of the correlated intensity is related to the diffusion coefficient of polymer chains and the longitudinal modulus of polymer networks.[107,108] Below, each relevant light scattering experiment is discussed from a theoretical point of view.

3.2 Turbidity

Light interacts with a solution of macromolecules in two ways: it is either scattered or absorbed.[96,106,109] Light is scattered when the incident electromagnetic wave interacts with the

dissolved polymer or particle purely elastically. If the interaction is inelastic, some energy is absorbed and dissipated as either heat or another form of electromagnetic energy.[110] Scattered light depends on the structure, contrast, and concentration of the scattering entity.[106,107,111]

Oftentimes it is experimentally convenient to track transmitted intensity, which is defined as the light that is neither scattered nor absorbed.[106,112] For purely elastic light scattering, the difference between incident and transmitted light is calculated by integrating the scattered intensity over all possible directions at an angle, θ between the beam and the scattering direction. For a primary beam of intensity I_0, the scattered intensity $I_{solute}(\theta)$, and distance between the scattering cross-section and the detector r, the Rayleigh ratio R_θ of the sample is:[106,113,114]

$$R_\theta = \int_0^\pi 2\pi r^2 \left(\frac{I_{solute}}{I_0}\right) \sin(\theta)\, d\theta \qquad (3.2.1)$$

$$\frac{I_{solute}}{I_0} = S(q)(1 + \cos^2\theta)/r^2 \qquad (3.2.2)$$

where $S(q)$ is related to the structure of the particle or polymer in solution. For a sphere of diameter D at a scattering vector $q = \frac{4\pi n}{\lambda}\sin\frac{\theta}{2}$ with the refractive index of the solvent n and wavelength of incident light λ:[106,113,115]

$$S(q) = \left[\frac{3}{x^3}(\sin x - x\cos x)\right]^2 \qquad x = \frac{qD}{2} \qquad (3.2.2)$$

For a rod of length L:

$$S(q) = \frac{1}{x}\int_0^{2x}\frac{\sin z}{z}dz\ - \left(\frac{\sin x}{x}\right)^2 \qquad x = \frac{qL}{2} \qquad (3.2.3)$$

And for a coil of root mean square of the end-to-end distance R:

$$S(q) = \frac{1}{x^2}[e^{-x} - (1 - x)] \qquad x = \frac{q^2R^2}{6} \qquad (3.2.4)$$

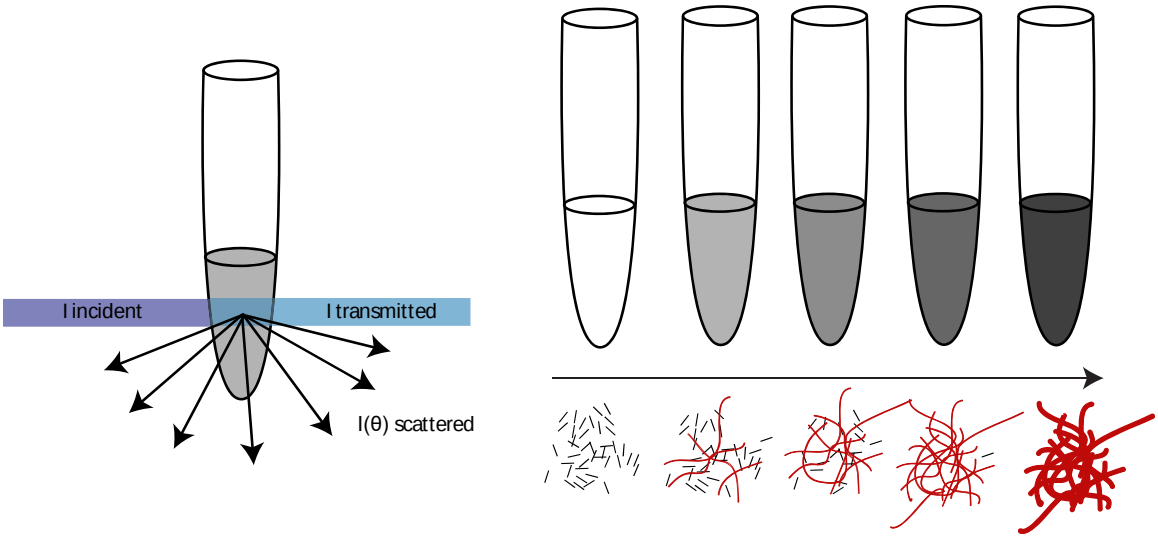

Figure 10.1: Turbidity is a measure of the total light scattered from a solution, or in other words, the intensity of light scattered at each angle, integrated from the angle of incidence to the angle of transmittance. Turbidity increases with the concentration and with the size scale of the scattering particle or molecule.

In general for all geometries however, the total light scattering depends on the concentration and the size of the particles. For dilute samples, the concentration dependence on the Rayleigh ratio is:[96,106]

$$R_\theta = \frac{HcMQ}{1+2BMc} \qquad (3.2.5)$$

where $H = \frac{32\pi^2 n_0^2}{3N_A\lambda^4}\left(\frac{dn}{dc}\right)^2$ is a constant with N_A the Avogadro's number, n_0 the solvent index of refraction, and $Q = \frac{3}{8}\int_0^\pi S(q)(1+\cos^2\theta)\sin\theta\, d\theta$ takes into account internal interference due to structure. The value B in equation 3.2.5 is the second virial coefficient, which accounts for the deviation from van't Hoff behavior. For the extreme condition of infinitely dilute particles or polymers, $c \to 0$ and Eq. 3.2.5 becomes linear in concentration:

$$R_\theta = HcMQ \qquad (3.2.6)$$

The turbidity, or alternatively the optical density, measured from a cuvette of length l is:[106]

$$\mathrm{T} = \frac{R_\theta l}{\log 100} \qquad (3.2.7)$$

The effect of structure and behavior on turbidity is shown schematically in Figure 3.1. Qualitatively if a solution of ~100 nm sized rods (black) is in equilibrium with ~10000 nm sized fibers (red), the total light scattering intensity depends on both the smaller rods and bigger fibers. In principle though, the scattered intensity from the fibers will be 100 times greater than from the rods, such that to a good approximation, only the fibers contribute to the turbidity. For a solution of fibers, the total light scattered depends on the total concentration of fibers as well as the fiber structure.

3.3 Static light scattering

Measuring the average intensity at each angle probes both the molecular weight and the structure of macromolecules. For dilute solutions of coils, the intensity of the solution depends on both the concentration and the structure factor. For small coils, such that $qR \ll 1$, Eq. 3.2.5 with the structure factor described by 3.2.2 is:[96,113,114]

$$\frac{Hc}{R_\theta} = \frac{1}{M}\left(1 + 2BMc + \frac{R^2q^2}{3} + \cdots\right) \qquad (3.3.1)$$

To determine the molecular weight of the coils, M, the second virial coefficient, B, and the radius of gyration, R, we measure the quantity $\frac{Hc}{R_\theta}$ of the solution as an independent function of both the coil concentration and the scattering angle. The set-up of the experiment is shown schematically in Figure 3.2. For a solution of a constant concentration, the scattered intensity is averaged at the detector for different angles and plotted against $c + q^2$. Repeating the procedure for different concentrations results in a Zimm plot. From the independent concentration and angle trends, two extrapolations are made, one for zero angle ($q \to 0$) and the other for zero concentration ($c \to 0$). The zero angle line for the assumptions outlined above is linear, with a y-intercept equal to $\frac{1}{M}$, and

slope $2B$. The zero concentration line is also linear, with a y-intercept equal to $\frac{1}{M}$, and slope $\frac{R^2}{3M}$. From the slopes and intercept of both trends, the quantities, B, M, and R are determined.[90,113,114]

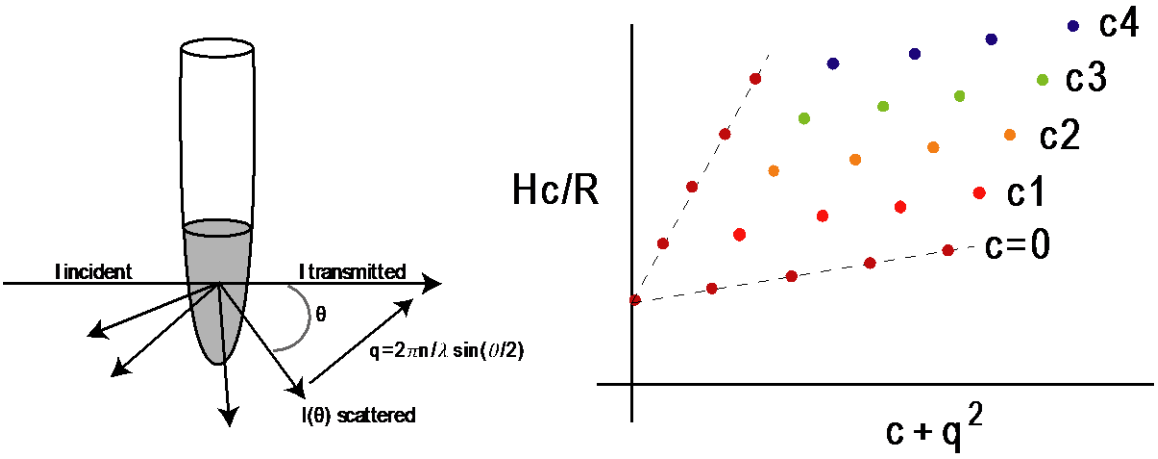

Figure 11.2: Zimm plot for a solution of polymers or particles. To construct a Zimm plot, intensity is averaged for a series of scattering vectors, q, and concentrations, c, independently. From the independent trends, the extrapolated lines at $q = 0$ and $c = 0$, are used to determine the structural information of the solute, such as R, M, and B.

3.4 Dynamic light scattering of polymer solutions

The temporal fluctuations of the scattered intensity are also used to determine the structure of macromolecules in solution.[100,107,108,116–119] The time dependence of the intensity is related to the density fluctuations of the macromolecules in the scattering volume, and the associated time scales probe the diffusive nature of the solute. Dynamic Light Scattering (DLS) is a technique that analyzes the dynamic information of macromolecules in solution from an autocorrelation of the intensity trace recorded during the experiment. The measured diffusion coefficient is related to the hydrodynamic radius of the diffusive coil or particle.[107,108]

The spatially averaged intensity-intensity correlation function, $g_2(q,t) = \frac{<I(t)I(t+\tau)>}{<I(t)>^2}$, at a specific scattering vector q and lag time τ, is related to the electric field autocorrelation function $g_1(q,t)$by the Seigert relation:[107,108]

$$g_2(q,t) = a(1 + \beta|g_1(q,t)|^2) \qquad (3.4.1)$$

Here a is a baseline and β is related to the non-zero cross-sections of the scattering volume and detector pinhole. The field autocorrelation function $g_1(q,t)$ for a solution of independently diffusing molecules is a single exponential of decay rate Γ and decay time τ:[107,108]

$$g_1(q,t) = \exp(-\Gamma t) = \exp\left(-\frac{t}{\tau}\right) \qquad (3.4.2)$$

The decay rate is related to the diffusion coefficient D:

$$\Gamma = Dq^2 \qquad (3.4.3)$$

We estimate the hydrodynamic radius R_H of the solute from the diffusion coefficient by modeling the solution as a suspension of spheres and assuming that the Stokes-Einstein equation holds:

$$D = \frac{k_B T}{6\pi\eta R_H} \qquad (3.4.4)$$

Here η is the viscosity of the solution, and k_B is the Boltzmann constant. The underlining assumption of Eq.3.4.4 is that the system is monodisperse. In reality, most solutions are polydisperse, so we have to re-formulate the electric field autocorrelation as a sum of exponentials. Each exponential is multiplied by its contribution:[120]

$$g_1(q,t) = \int P(\Gamma) e^{-\Gamma t} d\Gamma \qquad (3.4.5)$$

There are two ways to determine the decay time of g_1 and therefore the decay time of the experimentally achievable g_2. First is directly fitting an exponential decay to the correlation function. In this case $g_1(q,t) = a_0 + a_1 \exp(-\Gamma_1 t)$. The second method is CONTIN analysis, for which we take the inverse transform of Eq. 3.4.5 to calculate the function $P(\Gamma)$. From this, the distribution function of decay times $A(\tau)$ is obtained, which we can relate to the most probably decay time, and therefore from Eq. 3.4.4, the most probably hydrodynamic radius.

3.5 Dynamic light scattering of polymer networks

Density fluctuations in swollen networks are also determined by DLS.[41,46,47,49,121–129] In general for gels, the electric field correlation function follows from the displacement of the strands, U_q. There are several relaxation times or modes that can contribute to gel dynamics, but we can only probe the slower modes with dynamic light scattering. The normalized electric field correlation function is written as:[47,128]

$$g_1(q,\tau) = \frac{<E_q(0)E_q^*(t)>}{<E^2(0)>} \sim < U_q(0)U_q(t) > = < U_q(0) >^2 e^{-\frac{Kq^2t}{f}} \quad (3.5.1)$$

for which f is the solvent drag, and K is the longitudinal modulus. The perfect network should show electric field correlations that decay at long times. Most gels however are non-ergodic and have frozen-in structures. These inhomogeneities show up as a static electric field, which interferes directly with the scattered electric field from the gel modes. For real, imperfect gel systems, the electric field correlations are:[125,128,129]

$$g_2(q,\tau) - 1 = X^2[g_1(q,\tau)]^2 + 2X(1-X)g_1(\tau) \quad (3.5.2)$$

$X = \frac{<I>_F}{<I>_S + <I>_F}$ is the ratio of the intensity due to the fluctuating component, $< I >_F$ to the total intensity, $< I >_S + < I >_F$, which is a sum of the intensity of the static and fluctuating components. In general for these systems:[125,128,129]

$$g_2(q,\tau) - 1 = \beta \exp(-2D_A q^2 \tau) \quad (3.5.3)$$

D_A is the apparent elastic diffusion coefficient related to the true elastic diffusion coefficient by the value X: [125,128,129]

$$D_A = D/(2-X) \quad (3.5.4)$$

To evaluate the characteristic relaxation rate at each angle, multiple analysis methods are available. CONTIN analysis fits a weighted distribution of relaxation times:[120]

$$g_2(\tau) - 1 = \int_0^\infty P(\Gamma) \exp(-\Gamma\tau)\, d\Gamma \qquad (3.5.5)$$

where $P(\Gamma)$ is the weight of each relaxation rate, Γ, as determined by an inverse Laplace transform. Using this method, both the true and apparent elastic diffusion coefficient are extracted by fitting either Eq. 3.5.2 or Eq. 3.5.3. Multiple exponential fits of the correlation functions are also used in the analysis of decay rates as a function of angle. For a system of three distinct decay rates, $\Gamma_1 = b_1 q^2, \Gamma_2 = b_2 q^2, \Gamma_3 = b_3 q^2$:

$$g_1(\tau, q) = a_1 e^{-b_1 \tau q^2} + a_2 e^{-b_2 \tau q^2} + a_3 e^{-b_3 \tau q^2} \qquad (3.5.6)$$

In this case, the coefficients, b_1, b_2, b_3 will equal the apparent diffusion coefficients in the system, D_{A1}, D_{A2}, D_{A3} if the decay rates are linear with q^2 for all angles. As described by Eq. 3.5.4, the apparent diffusion coefficient is related to the true coefficient through the factor, X.

3.6 Small angle light scattering

If the macromolecules dissolved in solution are too large for a Zimm plot analysis or DLS, small angle light scattering (SALS) is used to determine any structural length scales.[119,130–135] SALS is also used to determine the sizescales of denser, interpenetrating, solutions. Above the overlap concentration, c^*, the scattered intensity at small angles probes the meshsize (ξ) of the macromolecule solution. The meshsize is defined as the average length between two overlapping macromolecules. The structure factor in this case is estimated by the Ornstein-Zernke approximation:[134–136]

$$S(q) = \frac{J}{1+q^2\xi^2} \qquad (3.6.1)$$

$$\text{with } J = \frac{k_B T}{\phi \frac{\partial \Pi}{\partial \phi}} \qquad (3.6.2)$$

where ϕ is the volume fraction of the overlapping molecules. Π is the osmotic pressure of the collagen fibers.

SALS can capture the time resolved structure of a growing fiber. Large molecules such as collagen fibers are to a good approximation rigid rods, for which the radius of gyration is just a function of geometrical constants, the radius R, and the length, L:[137,138]

$$R_g^2 = \sqrt{\frac{R^2}{2} + \frac{L^2}{12}} \qquad (3.6.3)$$

For collagen fibers of radius 100 nm, R_g is around 5774 nm. For collagen triple helices not assembled in solution the R_g is equal to 86 nm.

To measure the correlation lengths of collagen type II, the fibers have to be in the semi-dilute regime, and the concentrations above the overlap concentration: $c^* \sim \frac{M_w}{L^3 N_A}$.[139] The overlap concentration for collagen fibers is 3E-3 mg/mL. The physiological concentration of collagen is 0.3 mg/mL, well above the overlap concentration. The estimated correlation length, ξ, will depend on the concentration, c, and we estimate this dependence as:[30]

$$\xi \sim R_g \left(\frac{c}{c^*}\right)^{-\frac{1}{2}} \qquad (3.6.4)$$

The correlation length range therefore for possible collagen fiber concentrations (0.1 g/L – 1 g/L) is 30000 – 105000 nm. The corresponding q value range for this system is $0.0002 - 0.00006\ \mathrm{nm}^{-1}$. Below this q-value range, the intensity, $I(q)$, will be related to the correlation length and the thermodynamic properties of collagen.

3.7 Summary

Light scattering offers powerful and diverse tools for probing the structure of nanometer-sized macromolecules to micron-sized assemblies. The transmitted solution intensity from

solutions is related to both the concentration and size of the solute. Collagen fibers self-assemble into large rod-like structure. Monitoring turbidity of the solution allows the investigation of the assembly kinetics. Assuming homogeneous nucleation, the time dependent total light scattering intensity is only a function of the structure factor of the self-assembling rods. As the radius and length of the rods increases, so does scattered light intensity. For smaller, soluble proteins or synthetic polymers, the exact dimensions of the solute are determined by a Zimm Plot. The average intensity at specific angles and concentration is directly related to the structural information such as the radius of gyration, R, the molecular weight M, and the second virial coefficient, B. For larger, overlapping structures, such as a solution of collagen rods, SALS is used to investigate the meshsize of the solution. The meshsize for rods is related to the overlap concentration. Finally, DLS is used to determine the dynamic information of the solution, whether it is the diffusion coefficient of polymers or gel strand relaxation. We use these techniques to study the molecular structure and relaxations of the components of the vitreous.

CHAPTER 4

ELASTICITY OF POLYELECTROLYTE GELS IN EQUILIBRIUM

4.1 Introduction

Hyaluronic acid is responsible for swelling and elastic support of the vitreous. The charges that are part of each repeat unit dissociate into a charged monomer and a counter-ion. As described in Chapter 2, three pressures dictate the final state in equilibrium with a surrounding solution: (i) the chemical potential of counter-ions termed Donnan potential, (ii) the pressure due to elasticity of the polymer strands, (ii) and the pressure from the chemical mismatch between the gel and the solvent. The counter-ions permanently present in the network lead to an internal pressure that swells the network at lower salt concentrations. With added salt, the gels shrink because of the reduction in Donnan pressure relative to the background electrolyte solution. The elasticity of the network, which originates from the entropic penalty of deforming the polymeric strands counteracts swelling. Finally, if the polymer-polymer interactions are stronger than the polymer-solvent interactions, the gel remains polymer dense. If polymer-solvent interactions are stronger, the network tends to swell. The equilibrium polymer density of polyelectrolyte gels arises from the balance of the three pressures. The elastic modulus of these networks depends on the cross-link density, and therefore on the swelling conditions.[7–10,140]The specific relationships are discussed in detail in Chapter 2. For all polyelectrolyte networks, the degree of ionization (α), the hydrophobicity of the backbone (χ), the number of monomers between crosslinks (N), and concentration of added salt (c_s) control the material response.

Below, we show that the elastic modulus of highly swollen networks in high salt concentrations is consistent with the prediction of Eq. 2.4.12 without relying on scaling laws. There are only two unknown parameters, χ and α. The rest are known constants and measurable quantities

such as ϕ and c_s. Therefore to calculate χ and α, we have measured two independent trends, the modulus as a function of the volume fraction for a constant salt concentration, and the modulus as a function of the salt concentration for a constant volume fraction. The two thermodynamic parameters are enough to predict the full mechanical response of polyelectrolyte gels for high salt and high swelling conditions in a self – consistent way.

To fully determine all the material properties of the system, we establish the relationship between the longitudinal modulus and shear modulus. The elastic diffusion coefficient measured using DLS, is expressed in terms of Eq. 2.4.16, and is related to the shear modulus measured in a rheological experiment by f and v. To relate the two trends, we have measured the friction coefficient by following the earlier strategy by Tokita *et al*.[76] We show that the modulus calculated from DLS and measured from rheology are proportional to each other. From the proportionality quantity, we have determined the Poisson's ratio of the polyelectrolyte gels used in our study.

In a self-consistent way we show how to determine all the thermodynamic quantities that control the swelling and therefore the elasticity of hyaluronic acid gels pertinent to the vitreous of the eye (Figure 4.1). The self-consistent determination of swelling equilibrium, longitudinal modulus, shear modulus, friction coefficient, and Poisson's ratio as a function of α, ϕ, N, and c_s allows a complete description of ionic hydrogels.

4.2 Synthesis

To synthesize chemically cross-linked HA networks, we take advantage of the chemical structure of the polysaccharide. The carboxylic acid reacts with primary amines with the help of a coupling reagent. A convenient cross-linking molecule is cystamine. The thiol bridges of cystamine act as redox-active cross-links. A reducing agent easily reduces the bonds, and the presence of oxygen reforms them. At the same time, modifying the carboxylic acid groups does not disturb the

overall ionizability to any significant extent. In most cases, because of the high molecular weight of HA, percolating a network requires only 0.5-2% cross-links.

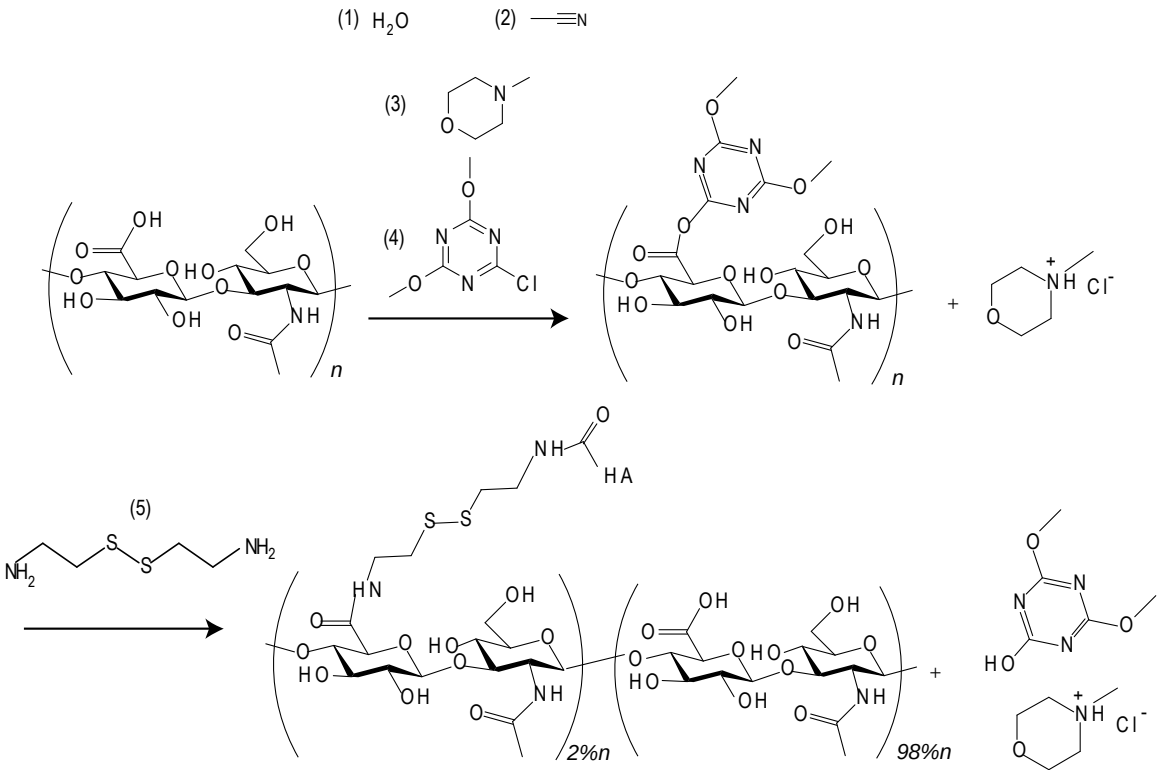

Figure 12.1: Synthesis of hyaluronic acid gels using triazene coupling.

For the synthesis, and subsequent experiments, all salts and reagents with the exception of HA were purchased from Sigma Aldrich and used without further purification. For every sample water was purified and de-ionized using a Milli-Q water purification system. The residual ionic strength of the purified water was estimated from conductivity measurements (12.8 MΩ cm^{-1}). HA was purchased from Life Science Pharmaceuticals. All experiments were performed at room temperature, 20°C, unless otherwise specified.

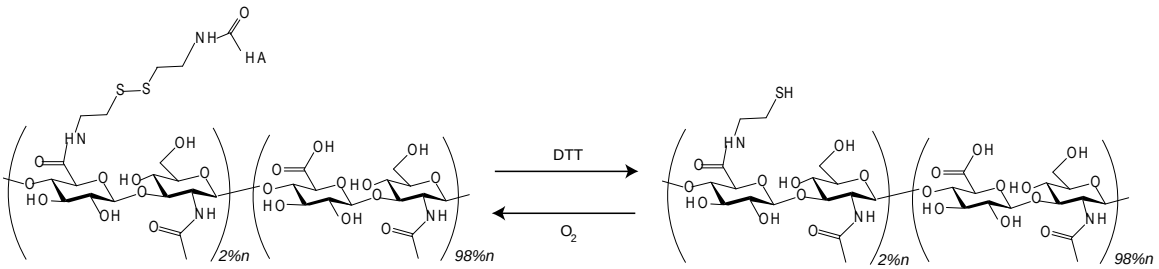

Figure 13.2: HA gels are redox active.

We use triazine-mediated amidation to functionalize HA with redox-active cystamine cross-links. Several groups have reported the optimized synthesis methodology for reactions of this type. While Bergman *et al.*[141] added small functional groups to HA, Borke *et al.*[142] report extensively the kinetics and the role of different amine reagents, which includes cystamine. Here we employ their general reaction schemes. 80 mg of 1.5 million g/mol HA was dissolved in 10 mL of water. After 24 hours of solvation time, 6.665 mL of acetonitrile was added drop-wise to the reaction. Next, 0.01 µL of N-Methylmorpholine (NMM) was added. After the solution was stirred for 1 hour, 25mg of 2-chloro-4,6-dimethoxy-1,3,5-triazine was added along with 0.1µL of 1M NaOH to make sure the solution was at pH 7. After stirring for 24 hours, 0.05 - 0.3 mL of 10mg/ml solution of cystamine hydrochloride was added and mixed overnight. The pH was maintained at 7 by titrating either NaOH or HCl. The variation of added cystamine resulted in controlled percent cross-linking. The covalent addition of cystamine cross-linked hyaluronic acid in the presence of oxygen (Figure 4.2). To control the gelation, we break up the existing bonds with excess dithiothreitol, which acts as a reducing agent (Figure 4.3). Finally the re-solubilized modified hyaluronic acid is dialyzed against a 40 mM NaCl, pH 3 buffer. The acidic buffer prevents the thiol bridges from forming. The modified hyaluronic acid solutions in 40 mM NaCl, pH 3 solution were then cross-linked in petri dishes by bringing the pH up to 8 by adding buffer or HCl. Modified HA was cross-linked only when exposed to excess oxygen or in the presence of 0.03 % hydrogen peroxide. Care is taken with the addition of peroxide since too much will degrade HA.

The modification of HA was assessed using rheological techniques described below, ^{1}H nuclear magnetic resonance (NMR), and a simple upside-down vial test. For NMR imaging, the modified HA samples were lyophilized after dialysis. The samples were flash frozen using liquid nitrogen, and put under vacuum to slowly sublimate the liquid overnight. The remaining white polymer sample was re-dissolved in D_2O for NMR imagining to 10 mg/mL. Avance300 NMR spectrometer was used to examine the magnetic field response of the sample. The resulting chemical shifts are plotted in Figure 4.3. The pure HA spectrum is consistent with previously published data.[141,142] The spectrum of a 2% modified shows a slight modification, which is consistent with the beta hydrogens of the thiol group.

Once the modified HA is cross-linked, the fluid solution turns into a soft gel. To assess the solid nature of the network, the vial was flipped upside down in a crude experiment. The absence of flow due to gravity affirms the success of the modification synthesis. A photo of such an experiment is shown in Figure 4.3.

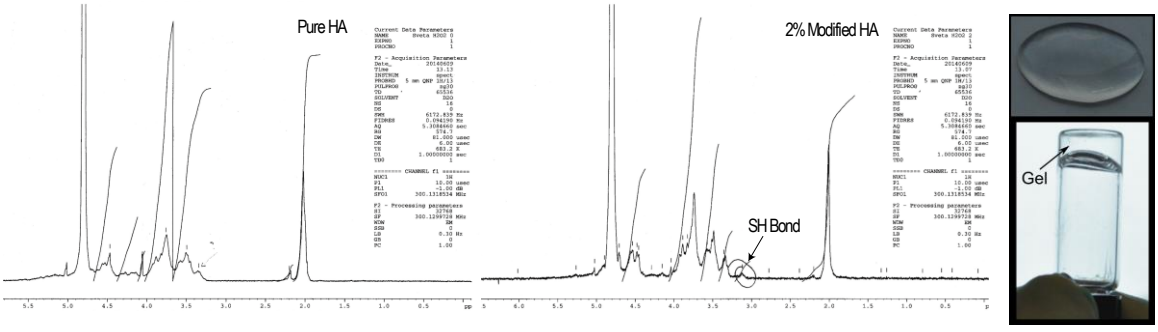

Figure 14.3: Affirmation of successful chemical crosslinking. NMR pre- and post-modification and photo of resulting soft transparent gels

4.3 Swelling equilibrium

For polyelectrolyte gels like cross-linked HA, the swelling equilibrium volume fraction is a complicated function of the salt concentration and the molecular weight between cross-links. For all systems however, the polymer concentration is an increasing function of the salt concentration. At zero salt, counter-ions in the network increase the internal pressure, which swells the gels. At

higher salt concentrations, the gels shrink because the chemical potential pressure of the counter-ions is reduced. The degree of swelling depends on the molecular weight between cross-links. Tightly cross-linked gels do not swell as much as gels with a higher molecular weights of elastically active strands.

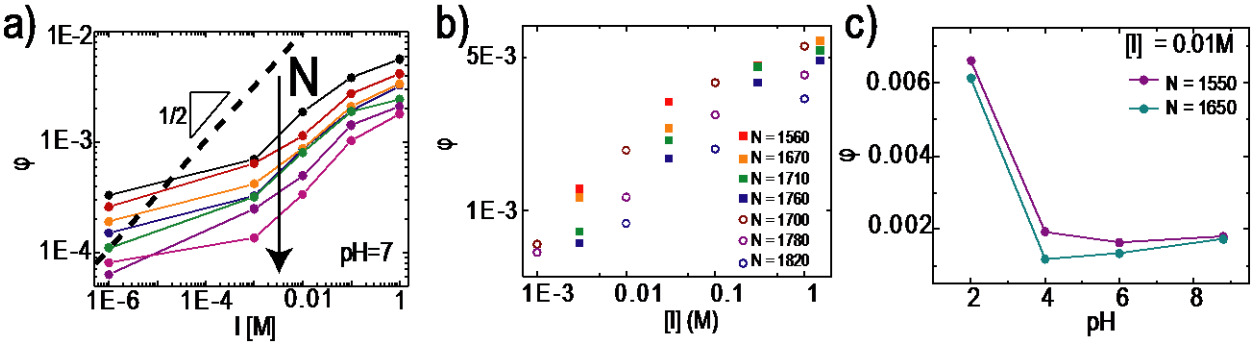

Figure 15.4: Swelling of HA gels at 20 °C. a) The measured volume fraction as a function of NaCl concentration I, and the number of monomers between cross-links *N* at pH 7. The volume fraction, or the polymer concentration, increases monotonically with ionic strength, and is controllable within two orders of magnitude by changing both the *I* and *N*. In this case, $N = 1670$ (black), $N = 1780$ (red), $N = 1820$ (organge), $N = 1830$ (blue), $N = 1830$ (green), $N = 1850$ (purple), $N = 1860$ (violet) as determined in the Supplementary Information. The black dashed like indicates a power law of 0.5. b) The effect of valency on the swelling of HA gels. ϕ values in both NaCl (open circles) and $CaCl_2$ (squares) solutions are comparable if the salt concentrations are concerted to ionic strength. c) The volume fraction at 0.01 M NaCl as a function of pH. At below the pKa of HA (2.9), the volume fraction increases by a factor of 3. This effect is not as dramatic as the effect of changing ionic strength of the solution.

To measure the swelling volume fraction, HA gels were brought to equilibrium with solutions of different salt concentrations over three days. The solution was exchanged 3 times a day. These experiments were repeated 3 times.

After the gels no longer changed in volume, the liquid was strained and the gels were weighted. Since the weight of the dry gel and swollen gel is known, the conversion to volume fraction is:

$$\phi = \left[1 + \frac{\rho_p}{\rho_s}\frac{M_b}{M_a} - \frac{\rho_p}{\rho_s}\right]^{-1} \qquad (4.3.1)$$

where M_a is the mass of the dried gel and M_b is the mass of the swollen gel; ρ_s and ρ_p are densities of polymer and solvent respectively. The density of water is taken as 1 g/cm^3, and the density of hyaluronic acid is taken as 1.29 g/cm^3.

In Figure 4.4, we show the effect of NaCl concentration on the volume fraction of polymer for 7 different HA gels at pH 7. By varying N and the external molar salt concentration, $I = N_A c_s$ where N_A is Avogadro's number, we control the volume fraction of our gels over two orders of magnitude, from 10^{-5} to 10^{-3}. To control N experimentally, we change the amount of cystamine added to the reaction. To facilitate discussion, we approximate the N values for HA gels using the swelling equilibrium Eq. 2.4.6. While c_s and ϕ are experimentally measurable quantities, we take α_0 as 0.25, v_1 as 3 x 10^{-26} L , and for α and χ we use values calculated in the following sections. Uniquely defined values for N are not pertinent for our study, and our estimates serve only as a reference for discussion. We note that no independent trials have been established for swelling equilibrium due to a lack of chemical control. Each time we run the reaction, even with a determinate amount of added cross-linking cystamine, the resulting N value is unpredictable. The highest volume fractions, corresponding to the densest gels, occur at the highest salt concentrations and lowest values of N. At 1 M NaCl for a gel with $N = 1670$, $\phi = 5.7 \text{ x } 10^{-3}$. The gels swell at low salt concentrations and for larger strand lengths. In pure water conditions, with an assumed salt concentration of 4 x 10^{-6} M based on conductivity, for a gel with the $N = 1860, \phi = 9.5 \text{ x } 10^{-5}$. As expected from equilibrium theories, the gels shrink in high salt, and the density depends inversely on the length of elastically active strands.

In the salt concentration range we have studied, ϕ is not a simple power law function of I, but nevertheless increases monotonically for all I. At higher I, between $I = 0.001$ and $I = 1$ M, it is notable that this dependence is weaker than a $1/2$ power law, indicated by the dashed line in Figure 4.4a.

The identity and valency of the ion does not change the swelling dependence. We compare the swelling results in NaCl solutions (open circles) and $CaCl_2$ solutions (squares) in Figure 4.4b. For both the monovalent and divalent electrolytes, we use Eq. 2.2.4 to estimate I in moles/L. From the figure for similar values of N, the gels swell to a similar ϕ and follow a similar monotonically increasing trend. For example, for a gel with $N = 1760$ swollen in 0.1 M $CaCl_2$, $I = 0.3$ M, $\phi = 0.0046$. Empirically extrapolated ϕ value for $I = 0.1$ M in this case is 0.0023. For a gel with a comparable $N = 1780$ swollen in 0.1M NaCl, $I = 0.1$ M, $\phi = 0.0027$. Swelling of HA gels do not appear to be sensitive to the valency of the electrolyte.

Ionizabilty of the backbone also modifies the volume fraction of HA gels. Lowering the ionizability of the backbone results in a lower number of counter-ions in the gel, and therefore a lower internal osmotic pressure. This effect is easily achieved by changing the pH of the solution. At pH below the acid dissociation (pKa) of the charged group on the backbone of HA, ionization is drastically decreased. In Figure 4.4b, we show the volume fraction as a function of pH for gels with two different N values (1550 and 1650) at 0.01 M NaCl. For $N = 1550$ at pH 2, the volume fraction increases from an average value of 1.7 x 10^{-3} to 6.6 x 10^{-3}, and remains relatively constant for pH 4, 6, and 8. For the other gel the trend is similar, at pH 2, the swelling decreases, which results in an increase in the volume fraction from an average value of 1.4 x 10^{-3} to 6.1 x 10^{-3}. Since the pKa of HA is 2.9, the higher volume fraction at pH 2 is consistent with association of counter-ions to the backbone. With lower counter-ion pressure to provide tension to the elastically active strands, the gels shrink. The predicted polymer volume fractions from the re-arranged swelling equilibrium Eq. 2.4.6 for the two gels as $\alpha \to 0$ are 0.0062 and 0.0056 for $N = 1550$ and $N = 1650$ respectively, and are consistent with our observations.

Remarkably, the effect of ionic strength is much larger than the effect of pH at 0.01 M for a gel with a constant N. The volume fraction is variable by a factor of 17 with changing salt

concentration, from ϕ = 5.7 x 10^{-3} to ϕ = 3.3 x 10^{-4} for a gel with N = 1670. The measurable pH effect at 0.01 M NaCl is only a factor of 4, from 0.0014 to 0.0061.

4.4 Rheology

The elasticity of polyelectrolyte gels in swelling equilibrium depends on the structure of the network and thermodynamic parameters such as α and χ. As shown in the previous section, lowering α leads to denser gels. Increasing the hydrophobicity of the backbone, by increasing χ leads to the same effect. For highly swollen gels, in high salt conditions, Eq. 2.4.16 describes the trends necessary to experimentally determine α and χ. Keeping c_s constant and varying the equilibrium volume fraction by changing N, we expect $G' \sim \phi^2$. Measuring this trend for different salt concentrations, the slope and intercept of the $\frac{\partial G}{\partial(\phi^2)}$ vs. $\frac{1}{c_s}$ data are related to the ionizability of the backbone and the chemical mismatch parameter.

All rheological experiments were done using the AR2000 rheometer from TA Instruments. HA gels were brought to equilibrium in different salt concentrations to match the plate geometry, in our case cylinders with a 40 mm diameter. The gels were typically 200-1000 μm in height. Constant 1.6% strain amplitude frequency sweeps from 0.1 Hz – 1 Hz were used to measure the storage (G') and loss (G") modulus of each gel at 20°C. The amplitude was chosen so that the measurements were in the linear-elastic regime. This was tested by measuring the modulus with increased amplitude for a 0.1 Hz shear rate for each gel.

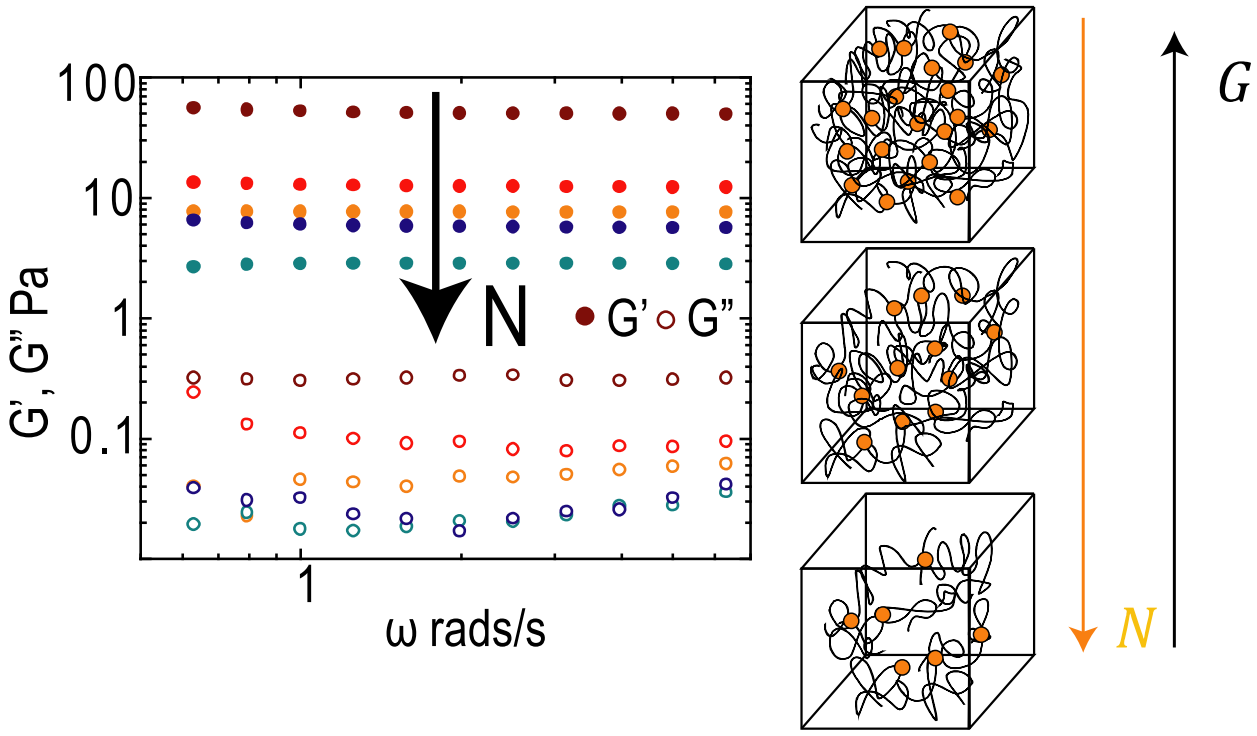

Figure 16.5: Shear rheology of hyaluronic acid gels. The elastic modulus, G', and the storage modulus, G", as a function of *N* and frequency at 1.6% oscillatory strain. Both the storage and loss moduli are constant in the frequency range for all *N* values shown and tested. In the figure $N = 1620$ (maroon), $N = 1775$ (red), $N = 1790$ (orange), $N = 1800$ (black), and $N = 1840$ (blue). The schematic on the right shows the modulus trends with varied *N* values. Gels with smaller *N* are more dense and rigid than gels with gels with higher *N*.

We have investigated the elastic of gels swollen in 0.001 – 2 M NaCl for a range of polymer volume fractions. For all gels, in all salt concentrations, the elastic shear modulus G', which describes the solid-like behavior of the gels, and the storage shear modulus G", which describes the fluid-like behavior of the gels, were constant with frequency in our experimental range of 0.6 rads/s to 6 rads/s. Furthermore, the elastic behavior dominates considerably since G' was reliably multiple orders of magnitude greater than G", which is consistent with the mechanical response for elastic solids. We plot G' and G" data for a range of *N* values in Figure 4.5. For gels with the lowest $N = 1620$, the storage modulus at 0.1 M NaCl, G', is 51 Pa, and the loss modulus, G", is 0.3 Pa. Systematically for gels with higher *N*, at a constant salt concentration, ϕ is lower and the modulus

is softer. As an example, for gels with the highest $N = 1840$ that we have investigated, the average G' and G" are 2.6 Pa and 0.02 Pa, respectively.

The experimental range for rheological experiments is limited to 0.6 rads/s to 6 rads/s for HA gels because the gels are so soft. At lower frequencies, the rheometer is not sensitive enough to measure the shear modulus of ~ 10 Pa. At higher frequencies, inertial effects emerge and skew the response.

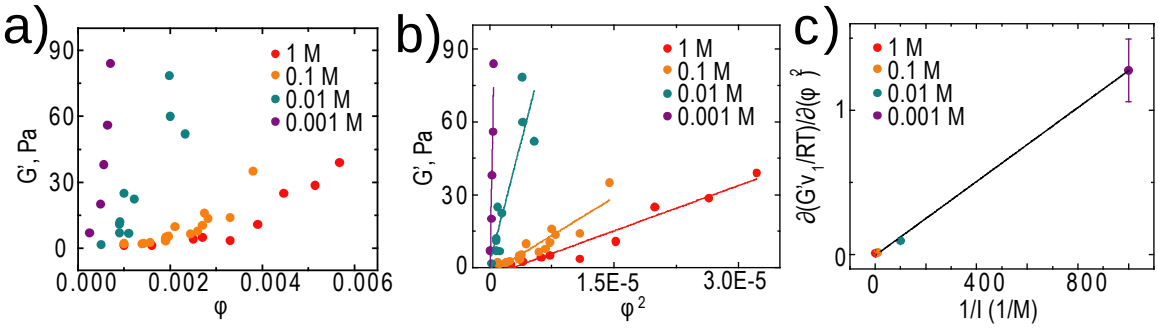

Figure 17.6: The elastic modulus as a function of the polymer volume fraction for swelling equilibrium at constant ionic strength. a) Changing the amount of cross-links added changes the polymer volume fraction at a constant salt concentration. The elastic modulus increases rapidly with ϕ in this case, for all salt concentrations. For lower salt concentrations, G' is considerably higher for a similar ϕ. b) The elastic shear modulus as a function of ϕ^2, for gels with varied N, at four different ionic strengths. At a constant ionic strength, the modulus varies proportionally with ϕ^2 within the experimental error. c) The slope of the linear trends in b) as a function of the inverse ionic strength. From the slope and intercept of the linear fit we calculate the ionizability α and the chemical mismatch parameter χ.

In Figure 4.6 we plot all modulus data as a function of ϕ and ϕ^2 for gels equilibrated against four different salt concentrations, 0.001 M, 0.01 M, 0.1 M, and 1 M. At a constant ionic strength, it is clear from Figure 4.4 that G' is a rapidly increasing function of ϕ. For a constant ϕ, the gels are considerably stiffer for lower salt concentrations. For a gel with $\phi = 0.002$, $G' = 2$ Pa at 1M NaCl, $G' = 5$ Pa at 0.1 M NaCl, and $G' = 60$ Pa at 0.01 M NaCl. Plotted against ϕ^2, the G' vs. ϕ^2 trend is linear. The solid lines in the plot are linear fits, which fit well within the scatter of the data, with the intercept close to zero for each fit as expected from Eq. 2.4.12. Each data point

represents a gel with a different N. The slopes for 1 M, 0.1 M, 0.01 M, and 0.001 M NaCl are 1.2 x 10^6 Pa, 2.0 x 10^6 Pa, 1.3 x 10^7 Pa, 1.8 x 10^8 Pa, respectively.

The slope for each line in Figure 4.6b is plotted in Figure 4.6c versus $1/I$. The colors for each ionic strength are consistent in Figure 4.6b and Figure 4.6c (1 M is red, 0.1 M is orange, 0.01 M is green, and 0.001 M is purple). The change in the elastic modulus as a function of the square of the volume fractions is linear with the inverse ionic strength for three decades of salt concentration. The slope of this linear trend is related to the ionizability of the gel strands, $\frac{\alpha^2}{4v_1}$. The intercept is related to the chemical mismatch of the gels strands, $\frac{1}{2} - \chi$. From the linear fit, we calculate the thermodynamic parameters α = 1 ± 0.02 % and $\chi = 0.499 \pm 0.01$. The statistics were determined from the scatter of the data shown in Figure 4.6b.

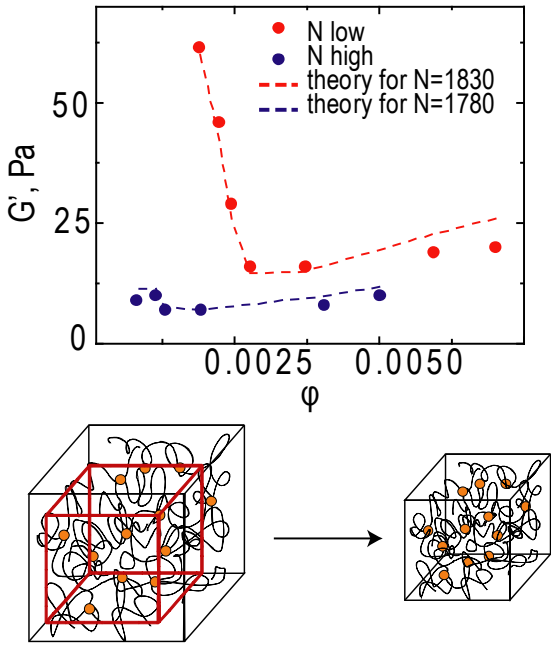

Figure 18.7: The prediction of Eq. 2.4.12 compared with rheological experiments. Storage modulus from rheological experiments (dots) as a function of the volume fraction for gels swollen in various ionic strength, 0.01, 0.02, 0.04, 0.06, 0.1, 0.5, and 1 M NaCl for two different gels, for $N = 1780$ (stiffer) and $N = 1830$ (softer). As shown in the schematic, at lower salt concentrations, the volume fraction is smaller as the gel swell compared to higher salt concentrations. The dashed lines are predictions of Eq. 2.4.12 without fitting parameters.

Along with these two thermodynamic quantities, we use the swelling equilibrium data at different salt concentrations to predict the elastic response of two low-volume fraction hyaluronic acid gels, one with $N = 1780$ and the other with $N = 1830$. In Figure 4.7 we plot the experimental modulus data (dots) for these different gels in 0.01, 0.02, 0.04, 0.6, 0.1, 0.2, 0.5 M NaCl solutions along with the predicted response from Eq. 2.4.12 (dashed line). As inputs to Eq. 2.4.12 we use α = 1% and $\chi = 0.499$, and the experimentally measured volume fraction data for each salt concentration in equilibrium. In this self-consisent way, Eq. 2.4.12 predicts the modulus behavior of gels with a constant N swollen in different salt concentrations. We find that even with equilibrium linear response perturbations the gels stiffen as they swell in lower salt concentrations. The stiffening is extremely sensitive to the molecular weight between cross-links. For gels with shorter strands between crosslinks ($N = 1780$), the elastic modulus increases by a factor of 4 from 16 to 60 Pa as the gels swelled from 0.0028 in 0.1 M NaCl to 0.00189 in 0.01 M NaCl. For softer gels ($N = 1830$), the modulus did not change as much with swelling in different salt concentrations. At the highest salt concentrations of 0.5 M NaCl, the modulus is 10 Pa. At 0.1 M NaCl, the gels swell and the modulus decreases to 7 Pa. When the salt concentration is decreased to 0.01 M NaCl, the volume fraction of the gel is 6 times lower than at 0.5 M NaCl, but the modulus increases back to 10 Pa.

The theoretical prediction deviates from experiments for higher salt concentrations. This is as expected because of the assumptions of the theory. At salt concentrations higher than 0.5 M NaCl, the ionizability is expected to decrease due to charge regularization, and higher order volume fraction terms to contribute to the modulus calculation.

4.5 Dynamic light scattering

The elastic diffusion coefficient measured with dynamic light scattering is proportional to the longitudinal modulus of the gels. As described in Eq. 2.4.16, we expect D to be a monotonically

increasing function of ϕ at a constant I, and to be inversely related to I for gels with a constant ϕ, which is similar to the trends observed with shear rheology. Dynamic light scattering measures time correlations in intensity due to density fluctuations in the networks. The density fluctuations are related to gel strand relaxations – the faster the gels strands relax in the presence of a dampening solvent, the faster the intensity correlations decay with time.

We have investigated gels of increasing values of N in solutions of two different NaCl concentrations, 1 M and 0.1 M. For each sample, the intensity at angles 30, 35, 40, 45, 50, 55, 60, 65, 70, and 75 was correlated for two minutes, and the relaxation times averaged for three different spatial locations within the gels. We show the normalized $g_2 - 1$ correlation functions for a gel with $N = 1670$ and N= 1820 at 0.1 M and 1 M in Figure 4.8b. We have chosen these systems, because in equilibrium they have the same polymer volume fraction, namely, $\phi = 0.0042$. HA gels swollen in 1M NaCl relax slower compared to gels of same density swollen in 0.1 M NaCl. At 1 M, the molecular weight of elastically active strands is higher than for gels of the same volume fraction swollen in 0.1 M NaCl. The relaxations are slower as expected for larger values of N, which is also related to the stiffness of the network. As shown in the earlier section, for a constant volume fraction, the shear modulus increases inversely with ionic strength. The diffusion coefficient is proportional to the stiffness of the network and is expected to have the same relationship with ionic strength at a constant volume fraction. This effect is sketched in Figure 4.8a.

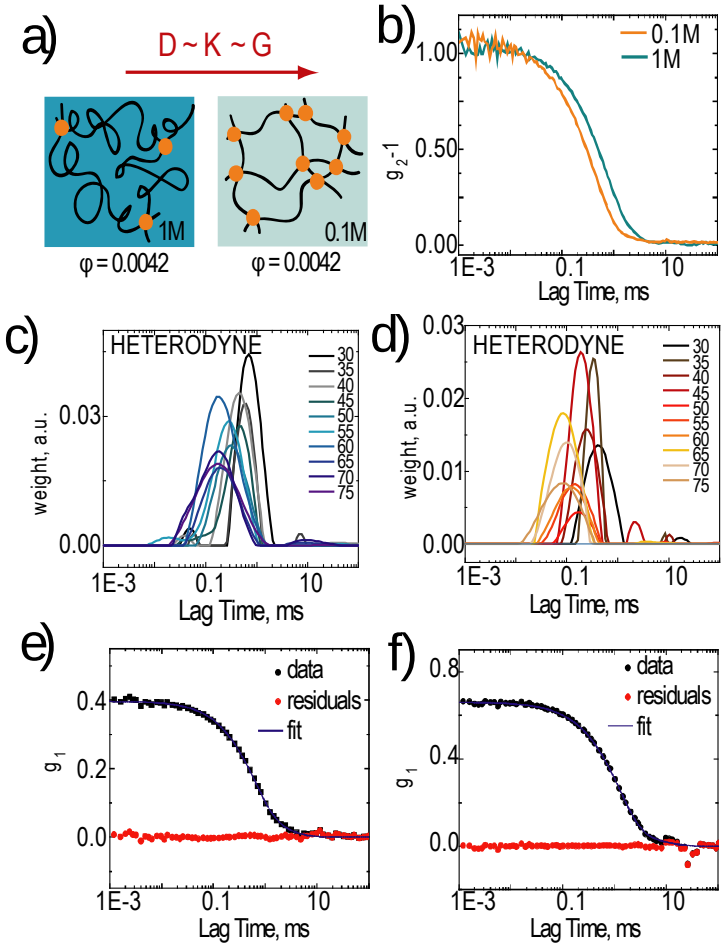

Figure 19.8: Analysis of DLS for HA gels with a constant $\phi = 0.0042$. a) To reach this volume fraction, gels swollen in 1 M [I] have a higher *N* and therefore lower modulus than gels swollen in 0.1 M [I]. b) Normalized $g_2 - 1$ correlation functions comparing the relaxation rates for HA gels with $\phi = 0.0042$ at 1 M [I] and 0.1 M [I] at 30°. The gels swollen in lower salt relax faster. c) Distribution functions of heterodyne analysis for a typical HA gel with $\phi = 0.0042$ at 1 M [I]. There are multiple distributions for each angle, but only one dominant one. d) Distribution functions of heterodyne analysis for a typical HA gel with $\phi = 0.0042$ at 0.1 M [I]. e) and f) A typical triple-exponential fit and residuals for HA gels with $\phi = 0.0042$ at 0.1 M [I] (e) and 1 M (f). Triple exponential functions fit well in both cases.

The correlation functions for each angle were analyzed using CONTIN analysis (Figure 4.8c,d) and multiple exponential fits (Figure 4.8e,f). The g_1 correlation functions are fit with three exponentials, because they typically do not show a simple decay. The residuals for these fits are shown in Figure 4.8e for a gel with $\phi = 0.0042$ swollen in 1M and in Figure 4.8f for a gel with $\phi = 0.0042$ swollen in 1M. Similarly, CONTIN analysis gives several distributions of decay times.

The several decay times result from the inhomogeneity of the gel, or the cleanliness of the gel as seen in previous works.[32,128] It is well documented in literature that these defects exist and can lead to problems with gel data analysis. In particular, the non-ergodicity of these networks results in a static component in the total intensity, as described in Chapter 3. However, for all methods of analysis, there is only one mode that has a clear q^2 dependence, shown in Figures 4.9a,b. The other, less contributing relaxations do not have a q^2 dependence and we do not consider them for our analysis (Figure 4.9c,d). While CONTIN and multiple exponential fits measure the apparent diffusion coefficient, heterodyne detection measures the true diffusion from just the fluctuating component of the intensity. The two values are related by Eq. 3.5.4.

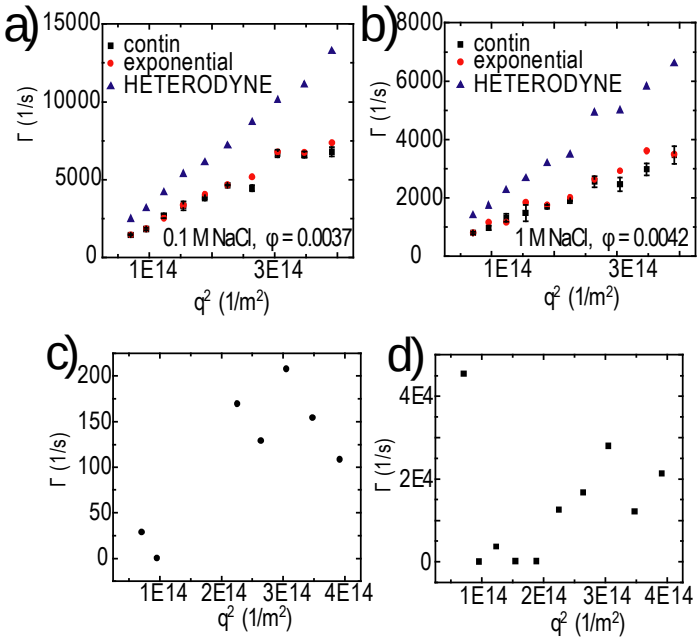

Figure 20.9: Comparison of the q dependence for the dominant mode and less contributing modes calculated with CONTIN, heterodyne, and triple exponential fits. a)-b)The dominant mode as a function of q^2 for gels in 0.1 M NaCl (a) and 1 M NaCl (b) while CONTIN and triple exponential fits are similar within the errors, the relaxation rates measured with heterodyne detection are higher. c)-d) The q^2 dependence of the decay rates from the other two exponential fits does not show a straightforward dependence.

We measure the elastic diffusion coefficient from the dominant relaxation rates, Γ. The relaxation mode of the density fluctuations is related to the modulus of the gel as described in Chapter 3 and Eq. 2.4.13 and Eq. 3.5.1. As an example, for the $N = 1820$ gel equilibrated in 1 M

NaCl the true elastic diffusion coefficient is 1.7 x 10^{-11} m^2/s, and for the gel with $N = 1670$ equilibrated in 0.1 M NaCl, the true elastic diffusion coefficient is 4.2 x 10^{-11} m^2/s. The apparent diffusion coefficient for all ϕ and both salt concentrations is plotted in Figure 4.10a. The general trends are consistent with the rheological data. The elastic diffusion coefficient increases with polymer density, and inversely with the salt concentration. At lower NaCl concentrations, the elastic diffusion is slower than at higher salt concentrations for the same volume fraction, as show in Figure 4.10b. We note that DLS becomes increasingly more challenging at lower ionic strengths, since equilibration time against the solvent in the DLS tube is longer, and the contrast of the HA gel strands against water is weaker. The fluctuating component of these gels dominate the scattering intensity, and on average among all the gel samples is 60% of the total intensity, with a 20% variation among samples. The X values used to determine the relative intensity due to the fluctuating component are plotted in Figure 4.10c. There is no clear ϕ or salt concentration dependence on this data, which we assume is a property of gel preparation.

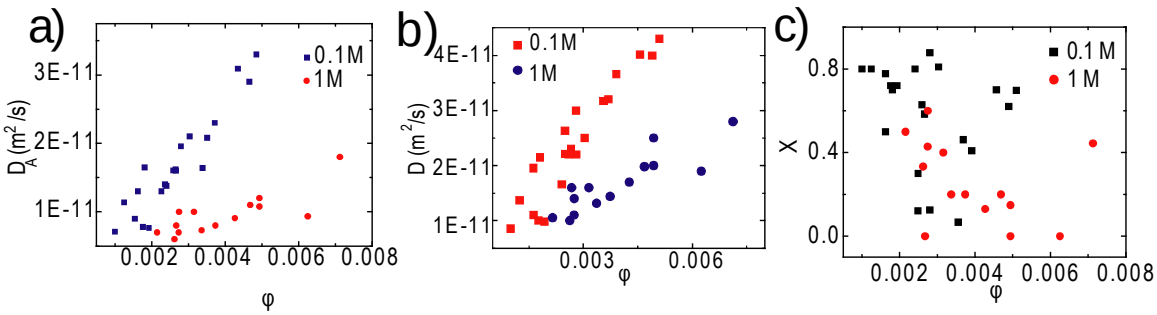

Figure 21.10: The apparent and true elastic diffusion coefficient as a function of ϕ. a) The apparent diffusion is an increasing function of the volume fraction, and is an inverse function of the salt concentration. b) The true diffusion coefficient follows the same trends as the apparent diffusion coefficient, but is generally larger. c) The factor X, which compares the apparent and true elastic diffusion. The variable does not have a defined salt and volume fraction dependence

4.6 Water Permeation

The above data by itself is not enough to directly compare the shear modulus from rheological experiments and the longitudinal modulus from DLS. There are two unknown

parameters in Eq. 2.4.16: one is the compressibility of the gels, the Poisson's ratio, ν, and the viscous friction of the polymer strands in a solvent, f. We determine$f$ experimentally by monitoring the velocity of the flow of water across a gel of specific dimension and volume fraction under an applied hydrostatic pressure.

The gel friction was measured in a set-up similar to that previously published.[76] Modified HA was crosslinked in a rubber cell 6.5 mm in thickness and 19.5 mm in diameter secured by Parafilm during gelation. After gelation, the Parafilm wrap was perforated to allow both sides of the gel to be exposed to the solvent. The cell was sandwiched in a 3D-printed water permeation cell, the dimensions of which are illustrated in Figure 4.11a. At one end of the cell, variable hydrostatic pressure is applied. At the other end of the cell, a glass capillary of 1 mm in diameter is attached. Water permeation is monitored by time lapse photography of the meniscus as it travels in the 1 mm capillary driven by the variable hydrostatic pressure through the gel. The acrylonitrile butadiene styrene (ABS) sample cell was 3D printed with the dimensions illustrated in Figure 4.11a using a Dimension uPrint SE Plus printer. The resulting product was sealed from water leaks using a Krylon acrylic sealant spray. The water flow was monitored using a stop-motion application TimeLapse on an Apple iPod.

Driven by a constant pressures, P, in steady-state flow, the friction coefficient of a gel is:[76]

$$f = \frac{P}{v_s}\frac{1}{d}\left(\frac{R}{r}\right)^2 = A\phi^{1.5} \quad (4.6.1)$$

where v_s is the velocity of the solvent across a gel of thickness d, $R = 9.5$ mm is the radius of the gel cross-section, and $r = 1$ mm is the radius of the capillary cross-section. Eq. 4.6.1 is expected to have a 1.5 power dependence with the volume fraction of the gel. Knowing both the friction coefficient and the volume fraction of the prepared gel, we determine the parameter A, which we use along with shear modulus, swelling equilibrium, and diffusion coefficient, to find the Poisson's ratio of hyaluronic acid gels.

For a gel with a volume fraction $\phi = 0.0036$, the steady-state flow velocity was monitored for four different hydrostatic pressures, 18000, 33000, 43000, and 71000 dynes/cm^2. As described in the Materials and Methods section, we monitored the flow by taking time-lapse photos of the meniscus in a capillary connected to gel. We show time snapshots at 0 seconds, 10800 seconds, 22800 seconds, 34800 seconds, 46800 seconds, and 58800 seconds of the meniscus in Figure 4.11c. From a snapshot of a ruler, we convert the pixel traveled values to actual distances in cm.

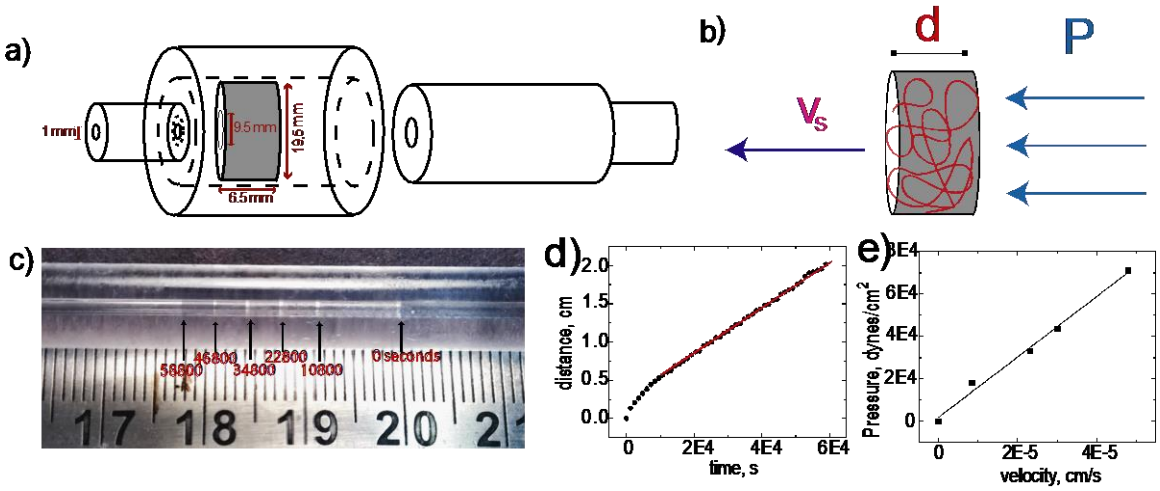

Figure 22.11. Water permeation experiment for the measurement of the friction coefficient. a) Dimensions of the 3D printed cell. b) Schematic of a water-permeation experiment: hydrostatic pressure is applied on one side of the gel in the cell, and velocity of the flow-through is measured in the meniscus on the other side. c) Time-resolved snap-shots of the water flow-through the gel at 0, 10800, 22800, 34800, 46800, and 58800 seconds. d) The change in the distance traveled of the meniscus with time. We calculate the velocity from the linear region, fit with the red line. e) Applied pressure versus the measured velocity fit with a straight line.

The flow rate data for a gel with the volume fraction equal to 0.0036 at a hydrostatic pressure of 43000 dynes/cm^2 is shown if Figure 4.11d. The distance the meniscus has traveled in the capillary is measured every 1200 seconds for 58800 seconds. At first we observe an acceleration of the flow rate, which has been observed by Tokita *et al.*[76] After the initial acceleration, the system reaches a steady-state, and the distance traveled by the meniscus is proportional to the observation time. In Figure 4.11d, we track the steady-state velocity by fitting a curve to the linear region and calculating the slope. For a gel of this dimension, under the applied pressure of 43000 dynes, we

find that the velocity of water permeation is 3 x 10^{-5} cm/s. From this measurement, the calculated friction coefficient is 1.4 x 10^{-11} dyne s/cm^4, such that the material parameter for a gel with a volume fraction of 0.0036, A = 6.41 x 10^{14} Pa s/m^2.

As a check, we monitor the water permeation velocity as a function of the applied pressure. In Figure 4.11e, we show the steady-state velocity data as a function of the applied hydrostatic pressure. The slope is related to the geometric parameters of our set-up and the friction coefficient of the gel, $\frac{\mathrm{d}P}{\mathrm{d}v_s} = \left(\frac{1}{d}\left(\frac{R}{r}\right)^2 \frac{1}{f}\right)^{-1}$. From the slope, we calculate the friction coefficient, f = 1.4 x 10^{-11} dyne s/cm^4, which matches exactly the calculated friction coefficient from the velocity data at 43000 dyne/cm^2 applied pressure.

4.7 Discussion

We have experimentally verified the theoretically predicted trends that at high salt concentrations, and low volume fractions, the elastic shear modulus of polyelectrolyte gels is quadratic with the volume fraction at a constant ionic strength, and inversely proportional to the ionic strength at a constant volume fraction. The prefactors for these power laws are related to α and χ. By measuring both trends independently, we calculate α = 1 ± 0.02% and $\chi = 0.499 \pm 0.01$ for hyaluronic acid gels for our experimental conditions. In a self-consistent way, the thermodynamic quantities in tandem with swelling measurements at different ionic strengths predict the elasticity of highly-swollen ultra-soft hyaluronic acid gels without any other fitting parameters. The gels swell with a decreasing I and stiffen for $I < 0.1$ M NaCl (Figure 4.7). Previously, this phenomenon has been attributed to finite extensibility of gel strands.[42] Here, we present a much simpler argument. In Figure 4.12a, we plot the rheological data (dots), along with the prediction of Eq. 2.4.12 (purple line). We deconstruct the theoretical prediction into its individual components. The first term in Eq. 2.4.12 is related to the chemical mismatch of the gel

and the solvent, $\frac{k_B T}{v_1}\left(\frac{1}{2}-\chi\right)\phi^2$, and the second term is related to the ionizability of the gel strands, $\frac{k_B T}{v_1}\left(\frac{\alpha^2}{4v_1 c_s}\right)\phi^2$. The chemical missmatch term is a quadratically increasing function of ϕ, while the Donnan equilibrium term is a decaying function of ϕ because even though ϕ is a complicated function of c_s, $\phi \sim c_s^a$, with $a < \frac{1}{2}$ as shown in Figure 4.12a for all salt concentrations.

In Figure 4.12b, we plot the individual contributions, the contribution from χ is shown as a dashed blue line, and the contribution from α is shown as the red dashed line. The two effects are competing, which results in a non-monotonic material response for a constant N swollen in solution of increasing NaCl concentrations. The effect therefore is not due to finite extensibility as previously reported, but due to stiffening of the gel strands at lower ionic strengths because of the internal Donnan equilibrium pressure, as illustrated Figure 4.12a. This behavior is expected to be universal for highly swollen polyelectrolyte gels, highly dependent on α and χ.

The longitudinal modulus measured from DLS is proportional to the shear modulus. The ϕ and I trends for this independent measurement of elasticity are consistent with rheological experiments. The elastic diffusion coefficient, D (Eq. 2.4.16), is inversely proportional to I at a constant ϕ, and is a monotonic increasing function of ϕ at a constant I. Using the measured thermodynamic parameters from rheology, α and χ, and the friction coefficient f from water permeation measurements, we find that $K \sim 170G'$, for both the 0.1 M and 1 M NaCl data, consistent with a Poisson's ratio of 0.498. We compare the two shear modulus results for different volume fractions at 0.1 M and 1 M NaCl in Figure 4.12c. The shear modulus measured from rheology, and the shear modulus calculated from DLS completely overlap within experimental error in the volume fraction and salt concentration range that we have investigated.

This data gives important insight into the physical nature of highly swollen hyaluronic acid gels. For linear deformations, highly swollen (> 99.95% water) hyaluronic acid gels are nearly

incompressible solids. As the gel is extended or compressed in the transverse direction, the axial direction is compressed to preserve the volume of the solid.

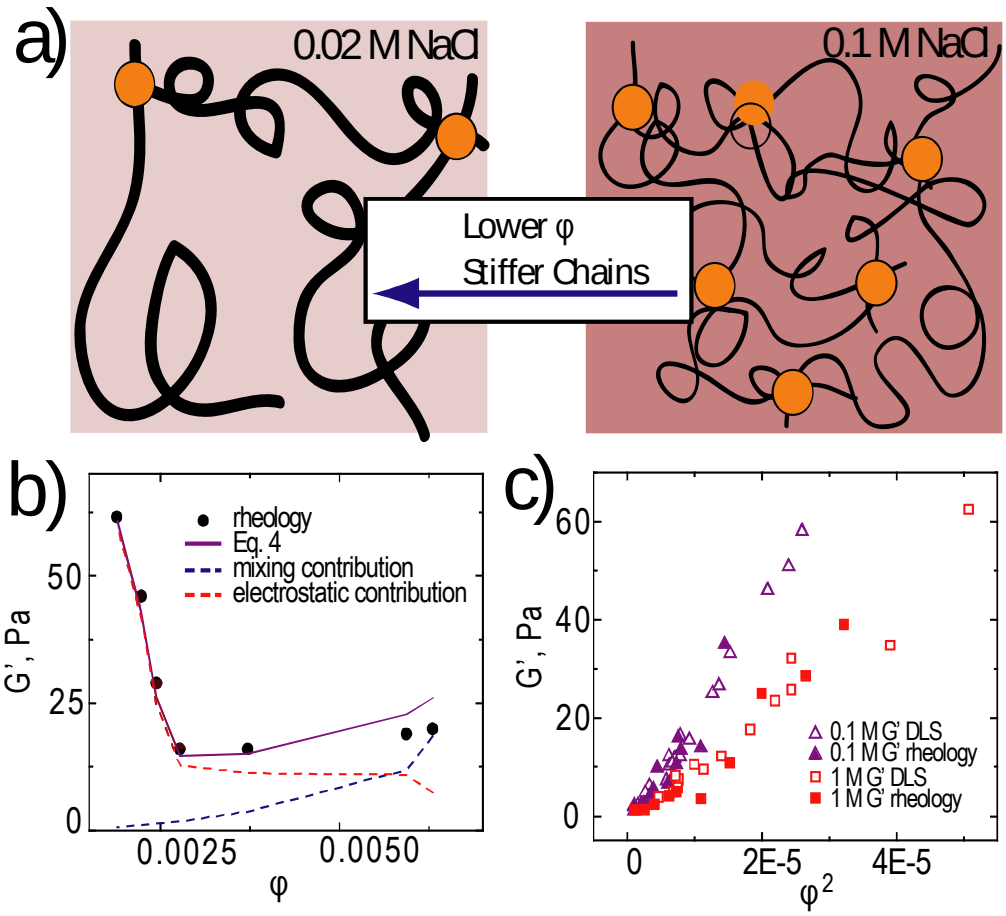

Figure 23.12. Dynamic behavior of highly swollen polyelectrolyte gels. a) Schematic for the chain stiffening at lower salt concentrations, the gels swell and stiffen due to the ionizability of the network. b) The elastic modulus determined from rheology (dots, same data as Figure 4.7d), and theory (purple line). The two match exactly for α = 1% and and χ = 0.499. To explain the non-monotinicity, Eq.2.4.12 is deconstructed into its components, the mixing contribution (blue dashed line), and the electrostatic contribution (red dashed line). At lower ionic strengths the gels stiffen due to electrostatic pressure as illustrated in a), and at higher ionic strengths the gels stiffen due to increased volume fraction. c) The shear modulus measured from rheology and calculated from DLS using water permeation results for 0.1 M (blue) and 1 M (red) versus ϕ^2. The two results overlap well within the experimental error.

4.8 Conclusions

In swelling equilibrium, the shear modulus of ionic gels is a function of two experimental determined quantities, c_{s0} and ϕ and two parameters, α and ϕ. By measuring G' as a function of

ϕ^2 at a constant I, and $\partial G'/\phi^2$ as a function of I. We have determined the thermodynamic quantities responsible for swelling equilibrium of polyelectrolyte gels and shown that existing equilibrium theories predict the elasticity of HA gels for our experimental conditions in a self-consistent way. At lower ionic strengths, even in equilibrium linear-elastic conditions, the gels swell and stiffen due to an internal pressure related to the ionizability of the backbone, which leads to a non-monotonic relationship of the modulus with the salt concentration.

The shear modulus of gels in equilibrium measured with rheology is proportional to the longitudinal modulus measured using DLS experiments. From their proportionality we determine the Poisson's ratio for this system to be 0.498. The extremely soft, highly swollen gels are incompressible solids for small deformations. The two elasticity data sets have the same trends with ϕ and I.

Using both DLS and rheological experiments, we have shown that ϕ does not uniquely determine the modulus of the system. A polyelectrolyte gel in 1 M NaCl at a certain density will have an order of magnitude lower modulus than the same gel with the same density swollen in in 0.1 M. This effect is captured well in established equilibrium theories. By determining the thermodynamic parameters of hyaluronic acid gels using rheological, DLS, swelling, and water permeation experiments we have developed an experimental protocol for the full characterization of polyelectrolyte gels.

CHAPTER 5

ELECTROSTATICS OF COLLAGEN FIBRILLIZATION

5.1 Introduction

Collagen is responsible for the support of a variety of animal tissues, including the extracellular vitreous. Without the rigid self-assembled collagen fibers, the vitreous is abundantly composed of HA, which is a highly swollen soft network, as described in the previous section. The structure and concentration of collagen fibers is essential for the support of the tissue and depends on the specifics of the self-assembly mechanism. It has been previously shown that the coulombic environment affects the final structure and the kinetics of collagen fiber formation, but the extent of the contribution remains unclear.[17,27]

To elucidate the contribution of electrostatic interactions on collagen type II fiber formation, we study the effects of monovalent salt concentration (0.006M-0.5M) and pH (2-10) on both the kinetics of fiber formation and equilibrium fiber size and concentration. Using turbidity measurements in tandem with more sensitive and higher-resolution techniques such as picro-sirius red staining and dynamic light scattering (DLS), we are able to gauge the solubility of collagen for broad salt and pH ranges. We find that electrostatic interactions contribute heavily to the bulk energy of fiber formation. For 189 mg/L collagen solutions, assemblies are possible only at salt concentrations below 250 mM and at intermediate pH ($10 > pH > 4$). At extreme pH ($pH < 4$, and $pH > 10$), collagen type II triple helices are homogeneously charged, and the energy to bring two molecules a short distance apart is highly positive and unfavorable. At intermediate pH collagen triple helices have a close to zero surface charge density because 336 positive and 324 negative residues are ionizable. At these conditions fibers assemble at ionic strengths below 250 mM, and while the fiber equilibrium width is increased with salt concentration, the total collagen fiber

concentration is reduced. The result is a non-monotonic trend of the total light scattering intensity as a function of ionic strength, which peaks at 110 mM for pH 7.2 and 37°C. The kinetics of fiber formation are fastest at lower ionic strengths, and quickly decay as $\sim \exp\left(\frac{\exp -\kappa d}{d k_B T}\right)$. These results suggest that electrostatics contribute favorably to the energetics of fiber formation at intermediate pH. These interactions are screened at higher salt concentrations. We find that numerical analysis using the amino acid sequence and Debye-Hückle theory can qualitatively explain both our kinetic data and equilibrium results.

5.2 Solubility of collagen triple-helices in extreme pH conditions

Collagen is a rigid triple-helix protein, and while the interior of the triple-helix is stabilized by hydrogen bonding, the exterior is decorated with both positive and negative charged residues. These ionizable amino acids contribute to the interaction potential between two collagen triple-helix molecules. The pKa's of these groups are listed in Chapter 2. As described, if pair-wise charge interactions or dipole-dipole interactions contribute to the assembly of collagen fibers we expect that at extreme pH, when only the positive or only the negative amino acids are ionized, collagen triple helixes remain soluble and do not form larger structures for any salt concentration.

To characterize collagen type II in these conditions, we use dynamic light scattering (DLS), a technique described in detail in Chapter 3. In our experiments, we use purified soluble type II collagen from bovine nasal septum (EPC Elastin Products CN276). Collagen solutions were kept at 4°C until use and re-made on a weekly basis to avoid degradation. Soluble collagen solutions were dissolved in 0.012 M HCl. All salts were purchased at Sigma-Aldrich.

DLS data from solutions at pH 2 and pH 10 confirms that collagen triple-helices are soluble when homogeneously charged, even in the presence of 0, 0.1, and 0.25M NaCl. Using CONTIN analysis we find that the correlation function of collagen solutions in these conditions is consistent

with only one distribution of relaxation times. We confirm this result by fitting the g_1 correlations with a single-decay function (Figure 5.1 a,c). The residuals analysis shows that single exponentials fully describe the correlation function. We plot the relaxation rates versus q^2 in Figure 5.1 b,d, and fit the result with a straight line of slope 7.9 e-12 ± 0.44 m^2/s for the acid solution and 6.4E-12 ± 0.56 m^2/s for the basic solution at 0 M NaCl. The same result is repeated at higher salt concentrations, while keeping the pH constant. Added salt does not change the solution properties of triple-helix collagen, and the diffusion coefficients are within experimental error of each other. We summarize the diffusion coefficients for three different ionic strengths of 0, 0.1 M, and 0.25 M at pH 2 and pH 10 in Table 5.1.

Table 1.1: DLS results of collagen type II at pH 2 and pH 10

	0 M NaCl	0.1 M NaCl	0.25 M NaCl
D, pH 2 (m^2/s)	7.9E-12 ± 0.44	7.1E-12	8.8E-12
D, pH 10 (m^2/s)	6.4E-12 ± 0.56	8.1E-12	7.9E-12

The diffusion coefficient measured for collagen triple helices in extreme pH conditions is consistent with the diffusion coefficient for rigid rods 300 nm in length and 1.5 nm in diameter.[137,138] Assuming a dense cylinder, the radius of gyration, R_G, depends on the radius of the cylinder, r, and the length of the cylinder, L: $R_G^2 = \frac{r^2}{2} + \frac{L^2}{12}$. For collagen type II triple helices, with a diameter of 1.5 nm, and a length of 300 nm, $R_G = 86$ nm. Broersma[138] predicted the expected R_H for this geometry: $R_H = \frac{R_G}{\left(\frac{1}{\sqrt{3}}\right)\left(\ln\left(\frac{L}{2r}\right)+0.38\right)}$, and the diffusion coefficient, $D = \frac{k_B T}{6\pi\eta R_H}$. For collagen type II triple helices, the expected diffusion coefficient is 7.4 x 10^{-12} m^2/s , and is exactly what we measure for all salt concentrations in pH 2 and pH 10.

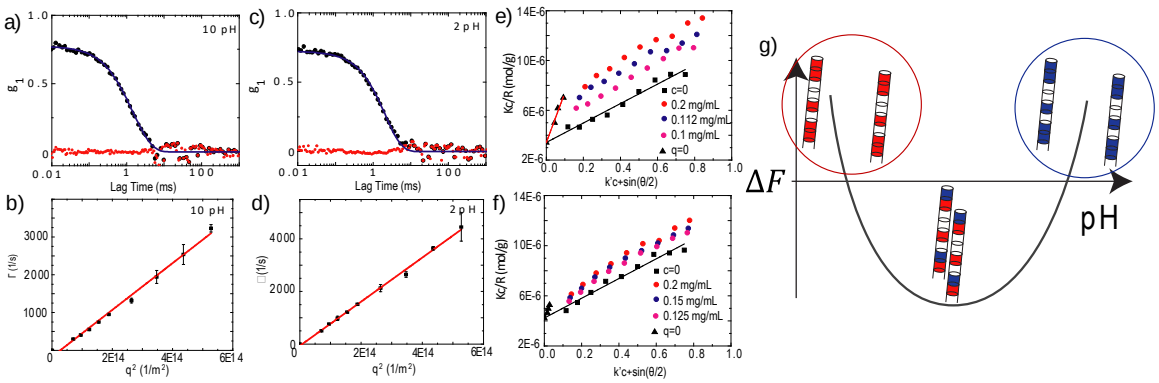

Figure 24.1. Light scattering of collagen solutions at pH 2 and pH 10. a) Typical g_1 correlation function at pH 10 with 0 M added NaCl, with a single exponential fit (blue). The residuals are shown in red, and indicate a good fit. b) The relaxation rate calculated from a single-exponential fit plotted against q^2. The trend is linear, and shows that the solute is diffusive. c) Typical g_1 correlation function at pH 2 0M NaCl, with a single exponential fit (blue). d) At pH 2, the solute is also diffusive, as indicated with the straight line dependence of the relaxation rate versus q^2. e) Zimm plot for pH 2, 0 M NaCl. f) Zimm plot for pH 2, 0.1 M NaCl. g) A schematic showing that at extreme pH, collagen is homogeneously charged, and the triple helices repel each other.

We confirm the dynamic light scattering results with static light scattering. While dynamic light scattering measures density fluctuations in the solution due to diffusing solutes, static light scattering measures how the solute contributes to the excess intensity. As described in Chapter 3, the excess intensity is related to the osmotic compressibility and the structure factor of the solute. By measuring the intensity as a function of both the concentration and scattering vector, we construct a Zimm plot, from which we determine R_g and B of collagen at different conditions. We show the Zimm plot for collagen dissolved in pH 2, 0 M added NaCl in Figure 5.1e. From the extrapolated $q = 0$ and $c = 0$ line, we calculate $M_W = 248000$ g/mol, $R_g = 81$ nm and $B = 2$ x 10^{-3} mL mol / g^2. The molecular weight is consistent with the expected molecular weight of a collagen triple helix, and the R_g is close to the theoretically predicted R_g for a rigid rod of 300 nm in length and 1.5 nm in diameter. This results confirms our DLS analysis. Both the excess scattering and the density fluctuations are due entirely to soluble, unassociated, collagen triple helices at pH 2.

The Zimm plot at pH 2 with added 0.1M NaCl is qualitatively similar, but the added salt gives rise to a few major differences (Figure 5.1f). As expected, the calculated molecular weight at the high salt condition is the same as the molecular weight at 0 M added NaCl, and is equal to 248000 g/mol. On the other hand, both R_g and B decrease with added salt. At 0.1 M NaCl, R_g = 74 nm, and B = 4 x 10^{-4} mL mol/ g^2.

The decrease in R_g and B with added salt is consistent with a homogeneous charge on the surface of collagen triple helices. In dilute conditions, the second virial coefficient is related to collagen-collagen interactions mediated by the solvent molecules. For homogeneously charged proteins, repulsive charge interaction contribute to the magnitude of B. At lower salt concentrations, as expected from Debye-Hückle theory, the repulsive charge interactions are long range, which leads to a larger positive B. With added salt, the electrostatic interactions are screened, and B decreases.

R_g decreases due to the polyelectrolyte effect.[90] At lower salt concentrations for homogeneously charged polymers, if polymer segments are repulsive with respect to the solvent, the coil will stretch out. With added salt, this effect is diminished, and the polymer contracts to a more relaxed configuration.

Our scattering experiments at pH 2 and pH 10 confirm that collagen type II triple helices are soluble at extreme pH for all salt concentrations. This solubility is related to the charge density on the surface of collagen triple helices, as illustrated in Figure 5.1g. Only the positive amino acids on the surface of the protein are ionized at pH 2, which leads to a strong repulsion between molecules. This repulsion weaken but does not change to attraction with added salt. At pH 10, a similar effect occurs. At extremely high pH, only the negative amino acids on the surface of the protein are ionized, which leads to soluble triple helices in solution.

5.3 Neutral pH collagen fiber structure and concentration

At intermediate pH values, both the positive and negative amino acids are ionizable, and we expect attractive interactions between collagen triple helices (Figure 5.2a). If these interactions result in collagen fiber assembly, both the kinetics and concentration of fibers are expected to change as a function of ionic strength of the solution. At lower ionic strength the interactions are long range and favorable, which we expect leads to faster kinetics and higher volume fraction of fibers. Higher salt screens the interactions, slowing the kinetics and decreasing the number of fibers formed.

We monitor the formation, the concentration, and structure of collagen fibers by measuring the total light scattered from the solution using a Hitachi u-3010 spectrophotometer. Each solution was pre-warmed using a water-bath heated metal sample holder before the addition of 0.01M HCl 1 mg/ml collagen stock solution. The initial concentration of collagen for all samples studied was 189 mg/L. After incubating the sample for 48 hours at each respective condition, we measured the turbidity. The results are summarized in Figure 5.2b.

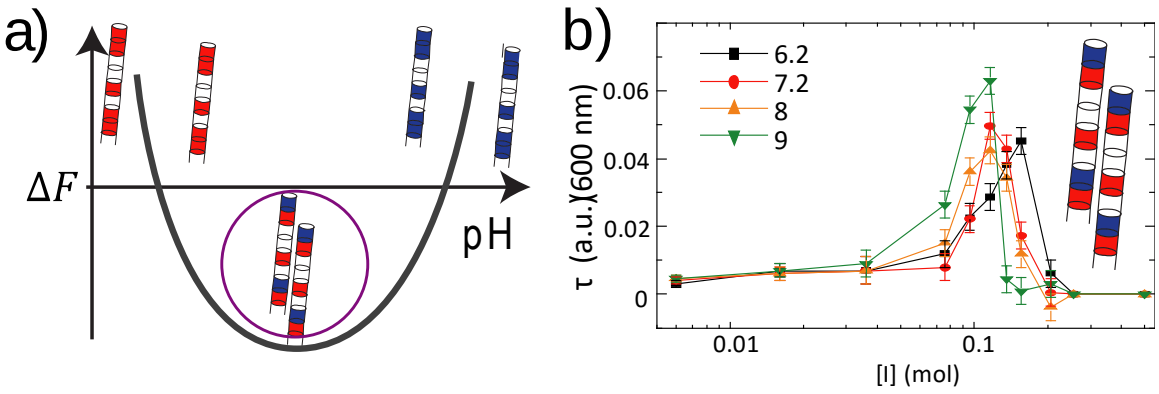

Figure 25.2. At intermediate pH and 37 ºC, collagen type II self-assembles into fibers. a) A schematic of the possible attractive potential at intermediate pH due to pair-wise interactions. At the pI of collagen, both positive and negative residues are ionizable, even though the total charge is zero. b) The turbidity at pH 6.2, pH 7.2, pH 8, and pH 9 after incubating collagen for 48 hours at varied ionic strength. The curve is non-monotonic. The turbidity is low at low and high ionic strengths and peaks at 100 mM [I]. The change in the total light scattering indicates fiber formation.

Surprisingly, turbidity is a non-monotonic function of ionic strength. For pH 7.2, at 6 mM [I], solution turbidity after 48 hours is 0.003 ± 0.001, and increases to 0.049 ± 0.004 at 116 mM [I]. At above 116 mM [I], the turbidity decreases to 0.017 at 156 mM [I], and is no longer detectable above 250 mM, even after a week's time. The trends are similar for pH 6.2, 8, and 9. For pH 6.2, at the lowest ionic strength, the turbidity is 0.003 ± 0.001, and increases to 0.045± 0.004 at 156 mM. For pH 8, at the lowest ionic strength, the turbidity is 0.0045 ± 0.001, and increases to 0.043± 0.004 at 116 mM. For pH 9, at the lowest ionic strength, the turbidity is 0.0045 ± 0.001, and increases to 0.062 ± 0.004 at 116 mM. At all pH turbidity decreases for ionic strengths above 150 mM and is undetectable above 250 mM. As expected at high and low pH solutions, we do not observe any change in the scattering intensity, for all salt concentrations tested (10^{-6} - 0.25 M).

It is impossible to determine the cause of the non-monotonic relationship solely from the turbidity data. As described in Chapter 3, for dilute samples, turbidity is an increasing function of concentration and an increasing function of the structure factor of the solute. The two effects are coupled. With this in mind, we measure both the collagen fiber size and collagen fiber concentration independently. We use AFM to determine the structure of collagen fibers, and a dye to determine the collagen fiber concentration.

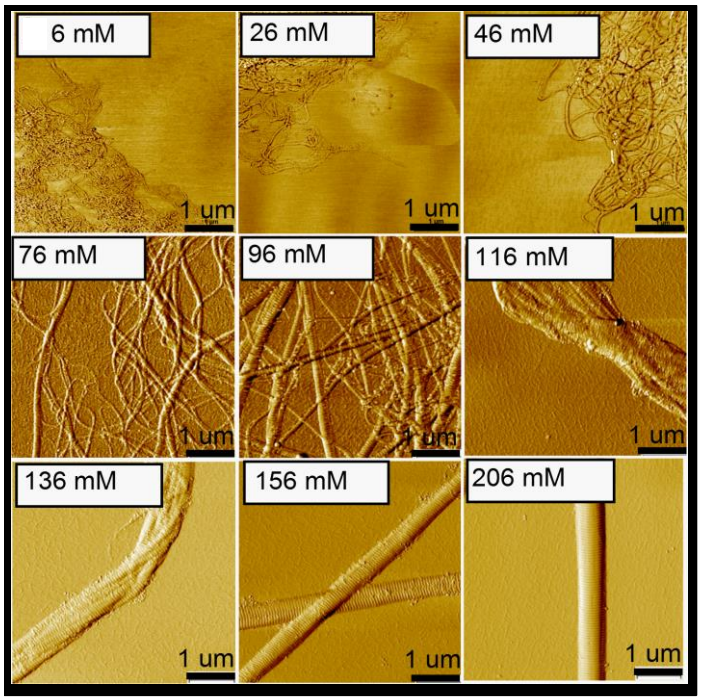

Figure 26.3. AFM images of collagen fibers at pH 7.2, 20ºC, and [I] = 6, 26, 46, 76, 96, 116, 136, 156, 206 mM.

For all AFM imaging experiments, a 10 μL droplet of each sample was deposited on a freshly-cleaved mica substrate for 10 minutes in a humid environment to avoid solution evaporation. The mica was then washed gently with de-ionized filtered water (Milli-q 12.8MΩ) to avoid salt crystallization on the substrate surface. Finally the samples were air-dried. All collagen samples were imaged using Digital Instrument AFM, model Dimension-3000, with an App Nano ACT-R-W Tapping Mode Probe tip. The tip radius is < 10 nm with a nominal frequency in air of about 200 - 400 KHz and a spring constant on an order of 25 - 75 N/m. The samples were imaged in a dry environment using the tapping mode.

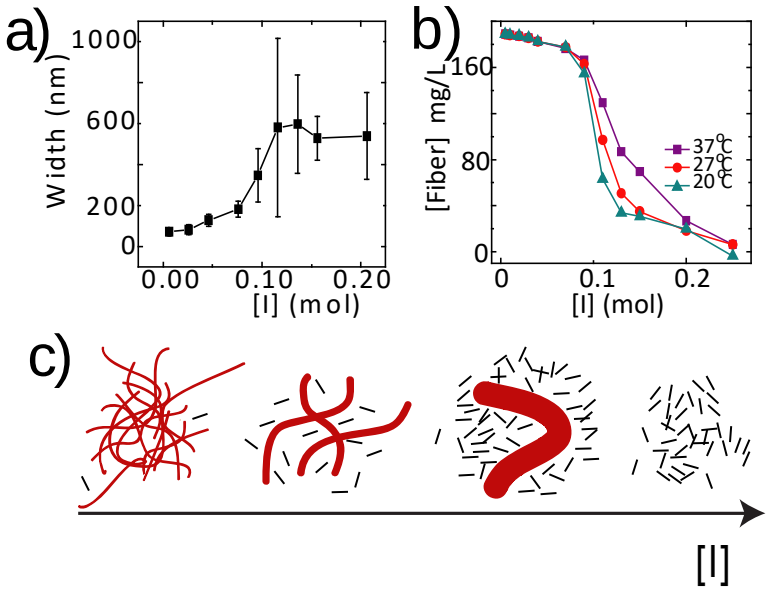

Figure 27.4. Deconstructing collagen solution turbidity into two contributing components, fiber structure and fiber concentration. a) Fiber diameter calculated from Figure 5.3, as a function of ionic strength at 20 ºC. The width increases monotonically. b) Concentration of fibers formed from the initial bulk 189 mg/L collagen triple helices as a function of ionic strength at 20 ºC, 27 ºC, and 37 ºC. The fiber concentration is monotonically reduced with ionic strength for all temperatures. c) A schematic of the main factors contributing to the non-monotonic turbidity change. As the ionic strength increases, collagen fiber size increases, while the concentration of fibers decreases.

Using AFM to probe the structure of collagen fibers, we find that in neutral solutions collagen type II assembles into fibers for all salt concentrations below 250 mM. Even at the lowest testable salt concentrations, ~ 6 mM, we observe the formation of fibers with AFM. Although there is some evidence of a turbidity change at these conditions, the fibers are so thin that solutions at lower ionic strengths are close to the low sensitivity range of the spectrophotometer.

The fibril thickness is heavily dependent on ionic strength (Figure 5.3). We quantify this observation by measuring the width profile distribution of collagen fibrils at each salt concentration (Figure 5.4a). At 6 mM, the fibers are thinnest, with an average width of 72 ± 18 nm. The thickness generally increases with salt concentration. At 116 mM the average fiber diameter is 600 ± 400 nm. Above 116 mM, the width is relatively constant, and at 206 mM the fiber diameter is on average 540 ± 200 nm. Amazingly, the fiber thickness can change an order of magnitude depending on the salt concentration.

While the fiber thickness increases with salt concentration, the total fiber concentration decreases (Figure 5.4b). The concentration of soluble collagen in solution was determined using a Sirius red F3B stain (1 g/L in water) (Polysciences, Inc). The equilibrated solutions were first centrifuged at 20,000 RPM for 15 minutes to spin down the fibers. Then the supernatant was removed and filtered using a 0.45 μm PES Millipore filter into a solution of 0.45 mL picro-sirius red stain and 0.1 mL 0.12 M HCl. After 20 minutes incubation time at room temperature, the resulting precipitate was spun down at 20,000 RPM for 15 minutes. These solutions were washed with 0.012 M HCl and spun down again at 20,000 RPM for 15 minutes, after which the supernatant was removed and the precipitated collagen was solubilized using a 0.1 M NaOH solution. The concentration was determined by comparing solutions against a calibrated standard curve. The fiber concentration and the concentration of soluble triple helices are assumed to be additive. Therefore to calculate the former quantity, the concentration of soluble triple helices was subtracted from the initial bulk concentration of 0.189 g/L. Starting with a total collagen concentration of 0.189 g/L, at the lowest ionic strength tested, 6 mM, ~ 99% of collagen triple helices assemble into fibers. With increased ionic strength, collagen fiber concentration decreases until at 250 mM 6 - 0% of the initial collagen triple-helices are assembled into fibers.

Decoupling the fiber structure and concentration reveals two competing effects that contribute to the total light scattering intensity. At lower ionic strength, collagen fiber concentration is high, but the fibers are thin. At higher ionic strengths, the fibers are thicker, but the total fiber concentration is much lower. We illustrate this effect in Figure 5.4c. Since total light scattering intensity depends on both concentration and structure, the competition of the fiber size and concentration as a function of ionic strength is responsible for the non-monotonicity shown in Figure 5.2b.

5.4 Neutral pH collagen fiber structure and concentration

Ionic strength of the solution also influences the kinetics of collagen assemblies. To resolve the temporal evolution of fibrillization, we monitor the turbidity at 600 nm every two seconds. The resulting turbidity curves have a characteristic sigmodal shape with three characteristics: a lag time, an equilibrium saturation value, and a growth rate. To compare the growth and nucleation rates, we normalize each raw absorbance curve by the saturation turbidity at long times. The growth rate is taken to be the inverse slope of the linear portion of the curve (A). The lag time, t_{lag} is the intercept of the same linear fit (Figure 5.5). The nucleation rate is inversely proportional to the lag time, $A' \sim \frac{1}{t_{lag}}$. The resulting data is an estimated extent of reaction versus time.

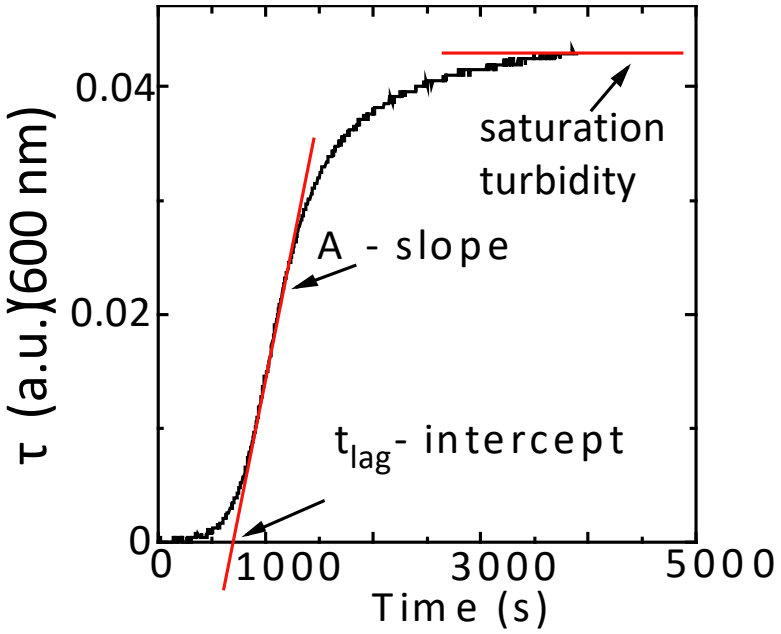

Figure 28.5. Typical turbidity curve for the formation of collagen fibers. There are three distinct characteristics of this curve, the growth rate, the lag time, and the saturation turbidity. From the slope of the linear region (red), we calculate the growth rate (A). From the intercept of the linear region with the x-axis, we calculate the lag time t_{lag}. At long times, the turbidity curve saturates at an intensity.

We find that as we increase the ionic strength of the solution from 90 to 120 mM, collagen type II fibrillization kinetics are generally slowed (Figure 5.6). The data presented in Figure 5.6 is plotted against the inverse Debye screening length, described in detail in Chapter 2. $\kappa \sim \sqrt{I}$ and

determines the inverse length scale below which electrostatics over power thermal fluctuations. By changing the ionic strength of the solution, we change the range of electrostatic interactions. At higher κ values electrostatic interactions are short range and weak. In an analogous way, temperature influences the strength of interactions. Thus, monitoring the growth and nucleation rates as we vary both the temperature and the salt concentration reveals important information about the mechanism of collagen fiber formation.

With the addition of salt, the lag time increases rapidly from 5.5 ± 1 seconds to 350 ± 40 seconds for 37°C, and from 230 to 3500 s for 24°C (Figure 5.6a). The growth rate decreases rapidly from 0.0097 s^{-1} to 0.0030 s^{-1} for 37°C and from 2E-4 s^{-1} to 3.2E-5 s^{-1} at 24°C (Figure 5.6b). Clearly increasing the temperature increases both the nucleation and growth rates of collagen fiber formation.

In Figure 5.6c and Figure 5.6d, we replot the data as $\ln A/s$ vs. $e^{-\kappa d}$. For both the nucleation and growth rates, the trends are linear for our experimental range, for all temperatures. Moreover, the slopes are similar for all data. The average of the slopes for $\ln A/s$ vs. $e^{-\kappa d}$ lines is 70 ± 6. The average of the slopes for $\ln A'/s$ vs. $e^{-\kappa d}$ is 77 ± 12. The change of kinetics with ionic strength is consistent with a Debye-Hückle energy barrier for fibrillization.

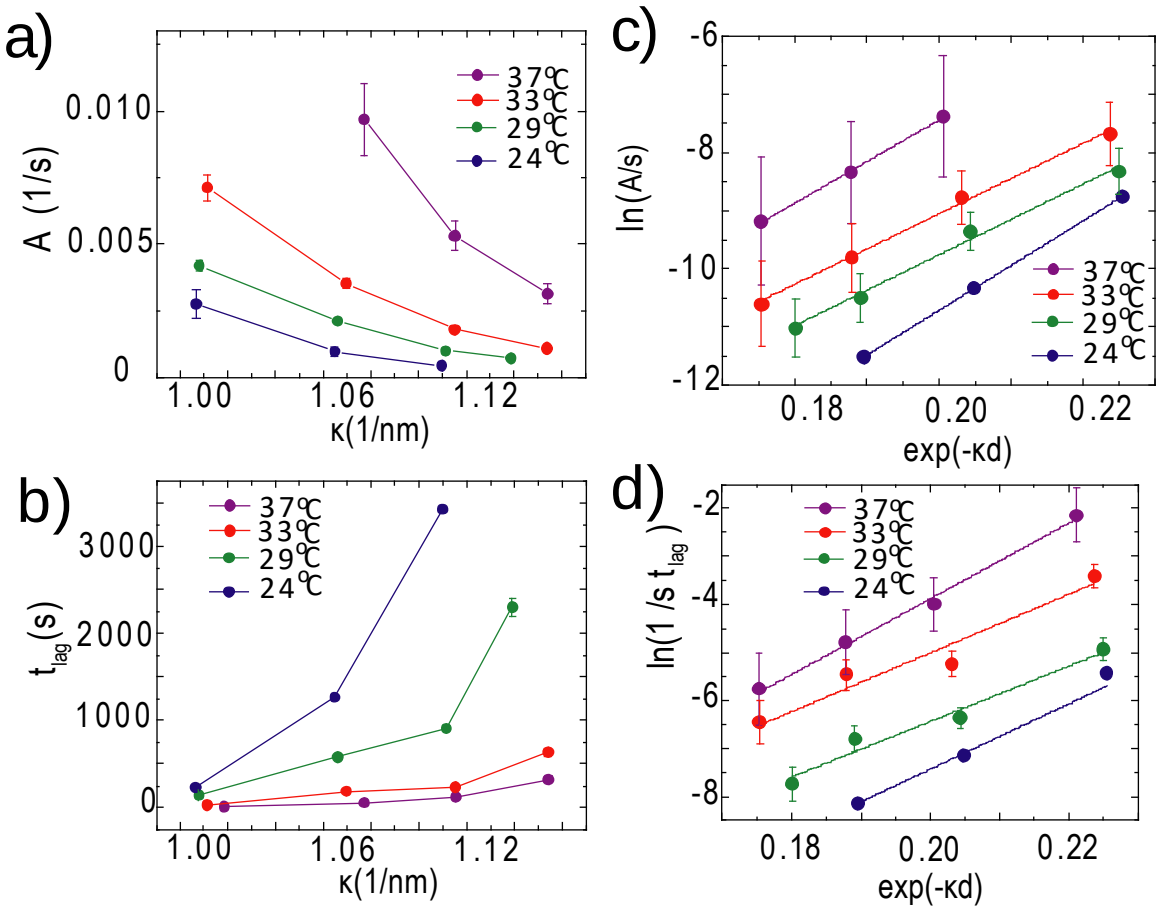

Figure 29.6. Kinetics of collagen fiber formation. a) The growth rate decreases rapidly with the inverse Debye-Hückle screening length, a measure of ionic strength, for all temperatures. The rates are inversely related to the temperature. b) Lag time as a function of ionic strength increases rapidly with ionic strength for all temperatures. c) The growth rate as a function of $\exp(-\kappa d)$ is linear for all temperatures, with an average slope of 70 ± 6. d) The nucleation rate as a function of $\exp(-\kappa d)$ is linear for all temperatures, with an average slope of 77 ± 12. All error bars are the standard deviation of three trials.

We monitor the temporal evolution of the average distance between fibers, ξ using small angle light scattering. By focusing on extremely small angles, we measure this structural information directly. In Figure 5.7a, we show the scattering decay profile for a 0.1 mg/mL collagen solution in 85 mM ionic strength solution at 37 ºC as a function of time. By fitting each intensity decay with the expected decay from an Ornstein-Zernike type approximation, discussed in Chapter 3, we calculate the meshsize of the solution of fibers as a function of time. Figure 5.7b shows that the meshsize increases from 2 to 4.5 μm during the duration of the experiment. To compare the kinetic information between the small angle light scattering experiments, we

compare the time it takes for the meshsize to change to half its value at long times, $t_{\frac{1}{2}}$. For the conditions of the sample in Figure 5.7a, $t_{\frac{1}{2}}$ = 100 s.

Temperature, ionic strength, and the initial concentration of collagen fibers influences both the meshsize and the kinetics. At a lower temperature, for a 0.15 mg/mL collagen, 90 mM [I] solution, the meshsize increases from 3.2 to 6.5 μm (Figure 5.7 c,d), with $t_{\frac{1}{2}} = 3000$ s. The kinetics are slower than for the sample analyzed in Figure 5.7a by a factor of 30. For the same conditions for a 0.1 mg/mL collagen solution, the meshsize is much smaller, and increases from 2.2 to 2.8 μm (Figure 5.7 e,f) with $t_{\frac{1}{2}} = 5000$ s. The kinetics and the final structure of collagen fibers is a sensitive function of the temperature, ionic strength, and bulk collagen concentration.

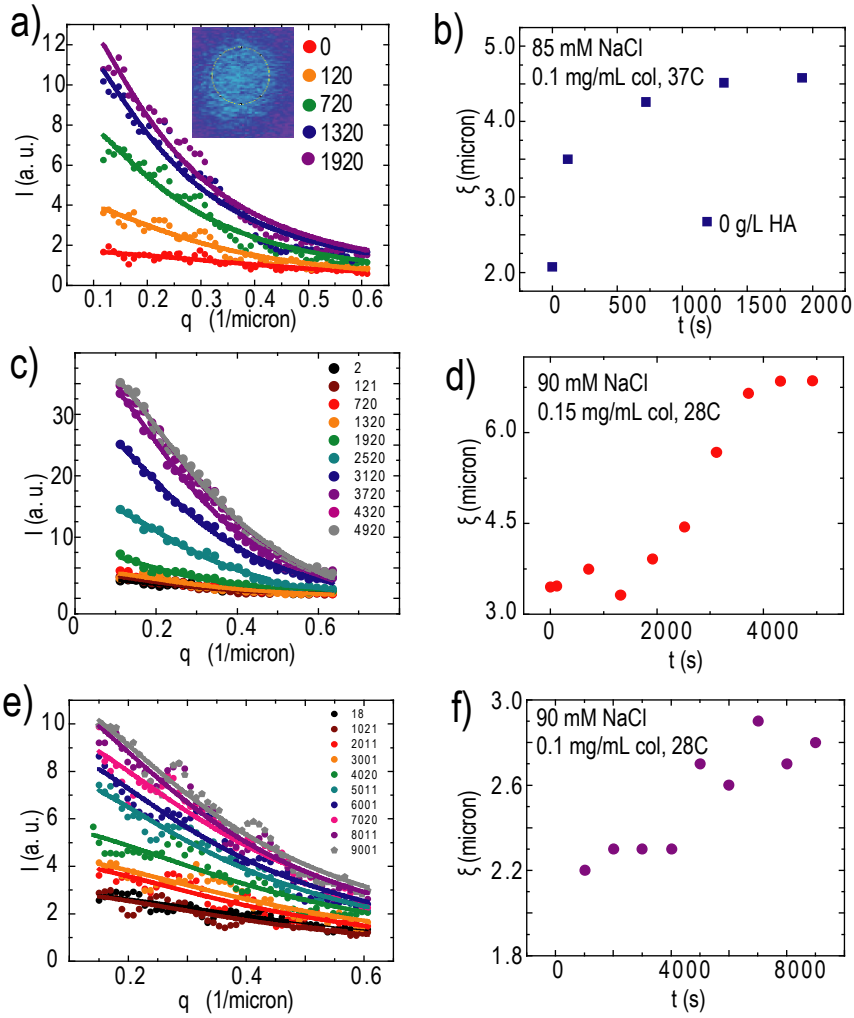

Figure 30.7. Time-resolved small angle light scattering of collagen fiber formation. a)-b) The decaying intensity profiles from a 0.1 mg/mL collagen, 85 mM NaCl and 37 ºC solution as a function of *q* for snapshots at 0 s, 120 s, 720 s, 1320 s, and 1920 s. After 1320 seconds, the system begins to saturate. The measured intensity was fit with Ornstein-Zernike type function, from which we calculate *ξ*, plotted in b). The meshsize increases with time, and saturates at longer times. c)-d) Data for 90 mM NaCl, 0.15 mg/ml collagen type II, and 28 ºC. With increased collagen concentration and salt and decreased temperature, the kinetics are much slower, but the meshsize is larger. e-f) Data for 90 mM NaCl, 0.1 g/ml collagen type II, and 28 ºC. With decreased collagen concentration , the kinetics are much slower, but the meshsize is smaller.

5.5 Discussion

The solution ionic strength greatly influences collagen type II fibril formation. At extreme pH, lower than 3 and greater than 10, collagen triple helices are completely soluble in solutions with ionic strength ranging from 10^{-6} M to 250 mM. Both DLS and SLS confirm that

collagen does not associate, and on the contrary, both scattering techniques show evidence that the triple helices strongly repel each other. The second virial coefficient, which we calculate using SLS, is large and positive at 10^{-6} M [I]. With the addition of 100 mM NaCl, A_2 decreases from $B = 2 \times 10^{-3}$ mL mol/ g^2 to $B = 4 \times 10^{-4}$ mL mol/ g^2. The salt-dependent second virial coefficient is consistent with a homogeneous charge density on collagen triple helices. At pH lower than 3, collagen triple helices are homogeneously positively charged and repel strongly in low salt solutions. Likewise, at pH higher than 10, collagen triple helices are homogeneously negatively charged. With the addition of salt, the repulsive interactions weaken due to Debye-Hückel screening.

At intermediate pH conditions for ionic strengths lower than 250 mM, collagen type II associates into larger fibers. The kinetics and the resulting fiber structure is extremely sensitive to the ionic strength of the solution. The average equilibrium fibril diameter changes from 72 ± 18 nm at 6 mM [I] to 540 ± 212 nm at 206 mM [I] (Figure 5.4). The concentration of fibers in solution decreases with salt, from 188 mg/L of the initial 189 mg/L, at 6mM [I], to 6mg/mL at 256 mM [I]. For a specific temperature, the total light scattering intensity, which is a function of the size of the structures in solution and the concentration, changes in a non-monotonic way with salt concentration (Figure 5.3). At 6 mM, the lowest ionic strength tested, the volume fraction of fibers is highest, and fibers have the smallest diameter. With additional salt, the equilibrium fiber diameter increases and the volume fraction of fibers decreases, resulting in the non-monotonicity of the total light scattering intensity. Above 250 mM, at the initial collagen concentration of 0.189 g/L, we observe minimal fiber self-assembly in solution. The kinetics of self-assembly slow down rapidly as a function of salt concentration. At 96mM, at pH 7.4 and 33°C in the linear region, the total intensity changes at a rate of 0.0071 units/second. The lag time for this condition is only about 30 seconds. The rate decreases to 0.0011 units/second at 126 mM, and the lag time increases nearly 21 times, to 635 seconds (Figure 5.6). These results are consistent with attractive

pairwise charge interactions driving collagen self-assembly in intermediate pH solutions. This requires the molecules to be close to net neural, or at conditions at which both positive and negative charges are ionizable. With added salt the attractive potential is weakened.

The effect of ionic strength on the assembly of collagen type II is consistent with electrostatics acting as a driving force for fiber formation.[27,143,144] Previously, Wallace et al.[27] modeled the electrostatic contribution to the work of bringing a two collagen triple helices a distance d apart by assuming that upon association, collagen is stabilized by a number of charged pairs, and destabilized by a smeared mean electrostatic potential from excess charge. In his method, the electrostatic free energy, Δf_{el}, will contribute to the bulk free energy of fiber formation, $\Delta f = \Delta f_{el} + \Delta f_{other}$. This free energy depends on both the distance between charges, d, and κ. In a general sense, the bulk formation energy is proportional to the work done for the assembly of a collagen type II dimer. To be more precise, we build up on Wallace's method by directly calculating the electrostatic contribution to the work done to form a collagen dimer in different pH and salt conditions by calculating the electrostatic interactions directly from the amino acid sequence.

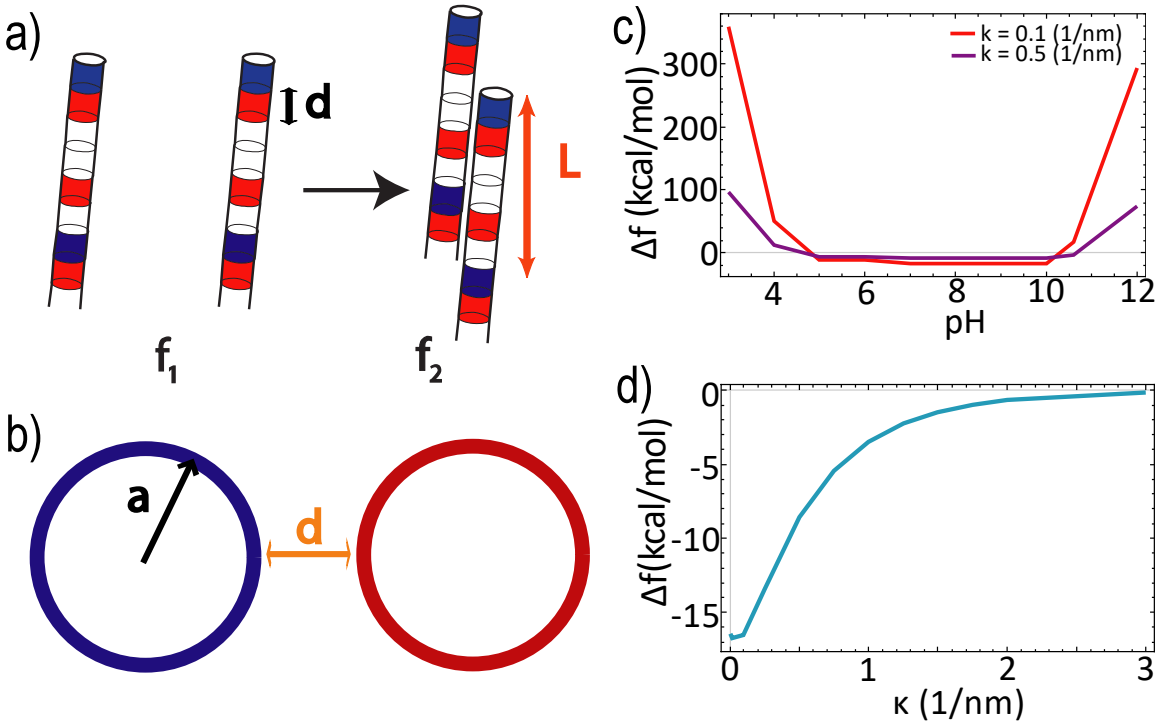

Figure 31.8. Numerical calculation of the work done to bring two collagen triple helices a distance d apart from infinity. a) We model collagen as long rods, segregated into cylinders of length d, and of smeared charge of value +3, -3, or 0 based on the amino acid sequence at any pH. The two rods are brought together in a parallel, staggered way, displaced by 234 amino acids based on previously observed structural information. b) The charges are assumed to be surface charges, located at a radial distance a. c) The numerical result as a function of pH, at extreme pH the collagen triple helices are repulsive, and at intermediate pH, collagen triple helices attract each other due to pair-wise interactions. d) At intermediate pH, the free energy change is diminished at higher salt concentrations.

To calculate electrostatic contribution directly, we numerically sum up the possible extended Debye-Hückle charge interactions as a function of [I], and pH. The triple helix proteins have a stiff backbone with a persistence length in water between 12 and 40 nm,[145] with all the charges on the perimeter of the molecule, facing the solvent. The amino acid sequence for each of the three peptides that form collagen type II is the same. From these physical traits, we simply model a collagen molecule as a charged linear rod with radius a, and residues a distance d apart (Figure 5.8a). Each coordinate has a smeared charge of value 0, 3, -3. These charges are a distance (a + d) apart distributed evenly around the circumference of the rod. When two rods are brought a distance $\sim d$ apart, (Figure 5.8b), the change in free energy for each interaction is:

$$\frac{\Delta f_{el}}{k_B T} = \sum_{i=1}^{L/d} \sum_{j=1}^{L/d} \frac{zz' e^2}{4\pi\epsilon\epsilon_0} \left[\frac{K_o\left(\kappa(\sqrt{(j-i)^2 d^2 + (2a+d)^2})\right)}{\kappa(\sqrt{(j-i)^2 d^2 + (2a+d)^2}) K_1\left(\kappa(\sqrt{(j-i)^2 d^2 + (2a+d)^2})\right)} \right] \qquad (5.5.1)$$

In Eq. 5.5.1, z_i is the charge of value 0, 3, or -3 of coordinate i away from the start of the stagger, and z'_j is the charge on the second rod. The total pairwise electrostatic interaction will depend on the stagger number n based on the amino acid sequence of collagen type II. For some configurations, the formation energy is positive, and for others it is negative. Previous wide angle x-ray scattering work by Antipova et al. has shown that in the assembled form, collagen type II triple helixes are staggered ~67 nm, or around ~234 nm in the helical region.[54] To be consistent with these results, all κ and pH results are calculated when the two parallel rods are mutually displaced by 234 residues. From these calculations, we find that for $\kappa = 0.001 - 3 \left(\frac{1}{\text{nm}}\right)$, the electrostatic contribution to the energy of formation varies in a non-monotonic way with pH (Figure 5.8c). Δf_{el} is positive for pH < 4 and pH > 10. In the intermediate pH range, at pH 7, Δf_{el} is minimum at $\kappa = 0.01 \left(\frac{1}{\text{nm}}\right)$, and decays with increased amount of salt (Figure 5.8d).

The kinetics of fiber formation show elements of an energy barrier process. In general the nucleation, A, and growth, A', rates follow

$$A \sim A' \sim \exp - \frac{\Delta f}{\mathrm{k_B} T} \sim \exp - \frac{\Delta f_{el}}{k_B T} \qquad (5.5.2)$$

where Δf is the enthalpy of bringing single molecule collagen to the surface. The salt concentration dependence of Eq. 5.5.2 is described by Eq. 5.5.1 and plotted in Figure 5.8d. With the addition of salt, the strength of the interaction is weaker. This generally agrees with our Debye-Hückel analysis of the kinetics plotted in Figures 5.6c and 5.6d. As κ increases, the barrier for nucleation and growth of collagen fibers increases exponentially. This leads to a drastically slower fibrillization, as seen in Figures 5.6 and 5.7.

5.6. Conclusion

We have shown that the kinetics and phase space of collagen fibers is in a signification part driven by the coulombic environment of the solution. At extreme pH, collagen is homogeneously charged and triple helices are soluble because of strong repulsive electrostatic interactions. At intermediate pH at which both positive and negative amino acids are ionized, collagen triple helices self-assemble into large fibers. Numerical calculations show that pair-wise electrostatic interactions between parallel triple helices contribute to the collective association.

Salt is directly responsible for the range of these interactions, such that at lower ionic strengths, electrostatic forces are long range and collagen triple helices are strongly attractive. This results in a higher concentration of collagen fibers in solution from the bulk, and fast kinetics. With the addition of salt, the interactions are screened, and the concentration of fibers is lower. Likewise the kinetics are slowed down consistent with a Debye-Hückel $e^{\frac{l_B e^{-\kappa d}}{d k_B T}}$ energy barrier for association. The insight into the mechanism of collagen assembly is crucial to understanding how the physiological environment can impact biological structures. As people age, the protein and ionic concentration throughout the body changes in dramatic ways, drastically influencing protein interactions and potentially leading to diseases.

CHAPTER 6

COMPOSITE NETWORKS

6.1 Introduction

The vitreous is a composite network, in which the soft hyaluronic acid network HA swells to suspend the rigid collagen fibers. HA gels are very soft as a result of permanent ionizable groups on the backbone of the polysaccharide (Chapter 4). In contrast, collagen fibers are macroscopic and have a high modulus, (~ GPa). Due to the disparity in moduli, the addition of collagen is expected to strongly reinforce the composites. The interaction between the two components modulates their mutual reinforcement. If collagen and HA are strongly interacting, the osmotic pressure and therefore the elasticity of the polysaccharide network is expected to change. The presence of HA is also expected to modify the association kinetics and final structure of collagen fibers. If HA-collagen interactions are stronger than collagen-collagen interactions, then we expect the kinetics of fiber formation to slow and fewer fibers to form. On the other hand, if the two components are non-interacting, then the presence of collagen is not expected to influence the swelling behavior of HA gels. The presence of the trapped rigid fibers will however increase the modulus of the composite. The interactions between the two components, or lack thereof, will determine the final physical properties of the composite hydrogel.

Here we systematically study the swelling and elasticity of hyaluronic acid networks in the presence of collagen fibers using swelling and rheological techniques. We investigate the structure and kinetics of collagen fiber formation in an HA matrix using light scattering. We find that for our formulations, the two networks do not interact enthalpically, but are mutually reinforcing. HA suspends collagen fibers without influencing the structure or concentration of collagen fibers, while the presence of collagen does not influence the swelling of the HA network.

6.2 Structure of collagen fibers in the presence of HA

In the vitreous, collagen self-assembles into fibers in a solution of hyaluronic acid. If the two components interact strongly, we expect HA to influence the kinetics and the final structure and concentration of collagen fibers. We investigate this influence by time-resolving the light scattered from collagen-HA mixtures at varied temperatures, ionic strengths, and pH.

For this study, we prepare solutions of 0.5 mg/ml HA in a phosphate buffer of pH 7 and NaCl concentrations between 10 mM and 200 mM. To time-resolve collagen fiber formation, we dilute a collagen stock prepared in 0.01 M HCl in 0.1 M NaCl HA solution at pH 7, and monitor the intensity of scattered light at small angles. The schematic of this process is shown in Figure 32. Depending on the experiment, we use either the uncross-linked cystamine-modified HA, or un-modified HA. The cystamine-modified HA eventually cross-links by thiol bridge formation in the presence of oxygen naturally dissolved in the solution. The oxidation is slow compared to collagen fiber formation and is usually complete within several days. The collagen fibers on the other hand are fully formed in a matter of hours. The discrepancy in the time scales allows for the creation of a fiber reinforced HA network in which collagen fibers are naturally dispersed.

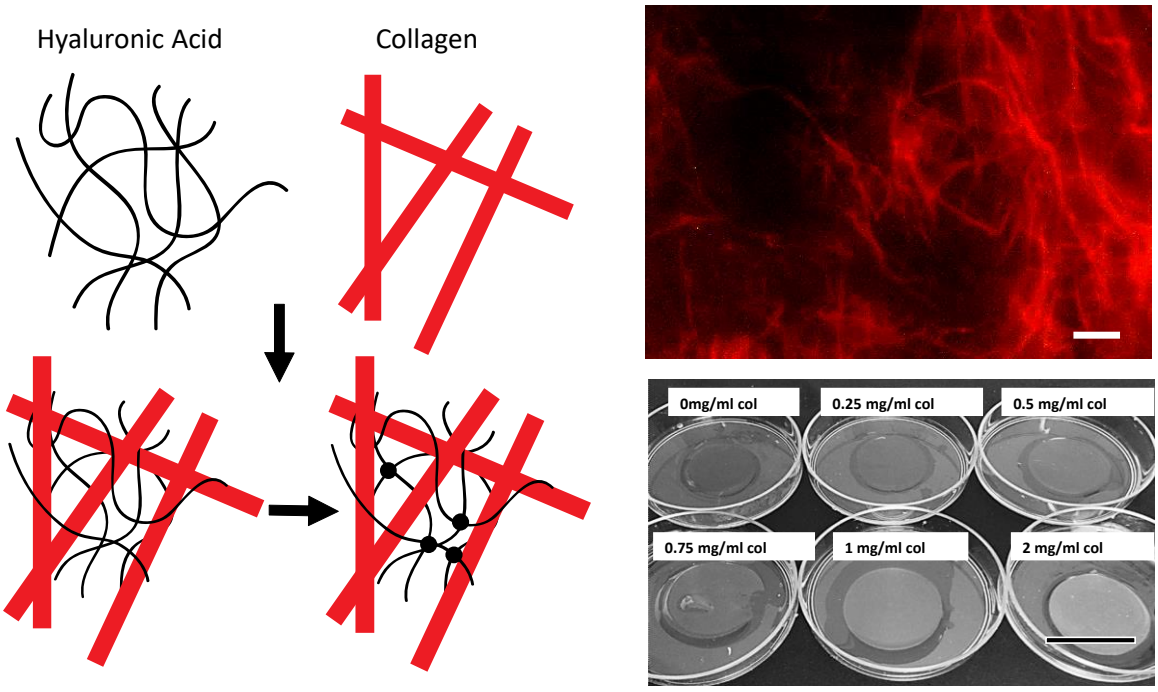

Figure 32.1. Collagen-HA composites. To synthesize the composites, collagen type II fibers are self-assembled in a solution of HA at intermediate pH and physiological ionic strength. Then, the HA is cross-linked to trap the fibers in the network.

We image the dispersed collagen fibers by staining the collagen present in the cross-linked gel. This methodology is similar to the staining protocol we used in the previous chapter to monitor the concentration of the protein. We swell the collagen-HA composite gels in a solution of 1 mg/mL pico-sirius stain solution in PBS overnight, after which we remove the excess stain by swelling the gels in pure PBS. We image the resulting stained collagen-HA composite using a Zeiss 200M Axiovert Inverted Microscope at 60X magnification. In Figure 6.1, the collagen fibers embedded in an HA hydrogel are clearly stained. Although it is hard to resolve the diameter from the image, it is consistent with ~ 500 nm, and the length is close to 10 μm. Without staining, the self-assembled collagen fibers effectively cloud the HA gels. As described in the previous chapter, this opacity change is related to the self-association of collagen into large fibrillar structures. We show this effect in Figure 6.1. The opacity of the composite network decreases with increased concentration of collagen. Collagen still self-assembles in the presence of HA.

To investigate the influence of the polysaccharide on both the kinetics and the structure of collagen fiber formation, we monitor the temporal evolution of both the turbidity and the small angle light scattering of a 0.1 mg/mL pH 7 and 90 mM [I] collagen solution mixed with 0 mg/mL and 0.47 mg/mL HA at 37 ºC. In Figure 6.2a, and Figure 6.2b, we compare the temporal evolution of SALS with (Figure 6.2a) and without (Figure 6.2b) the presence of un-crosslinked HA. The two data sets are qualitatively the same. We analyze each intensity profile with an Ornstein-Zernike fit, from which we determine the meshsize as a function of time, plotted in Figure 6.2c. The Ornstein-Zernike fits are consistent within the scatter. Surprisingly, the meshzie and the kinetics of the meshsize are similar with and without HA (Figure 6.2c). At the beginning of the experiment, the meshsize without HA is 2 μm, and increases to 4.5 μm after 2000 seconds. In the presence of the matrix, the meshsize starts at 2.8 μm and increases to 4.9 μm after 2000 seconds. The final meshsize is qualitatively consistent with the optical microscopy picture in Figure 6.1. As the collagen associates into fibers, the average distance between the fibers increases, with little influence by the HA network.

This result is consistent with time resolved turbidity experiments. For a 0.2 mg/mL pH 7 and 100 mM [I] collagen solutions, the temporal evolution of the total light scattering is unchanged for formulations with 0 mg/mL and 0.47 mg/mL HA at 37 ºC. In Figure 6.2d, we show the result of the measured turbidity normalized by the turbidity at long times. The data with and without HA overlap almost completely for the duration of the experiment. The presence of 0.47 mg/mL un-crosslinked HA, which is consistent with the concentration of HA in the vitreous, at 37 ºC does not influence the kinetics and structure of collagen fibers.

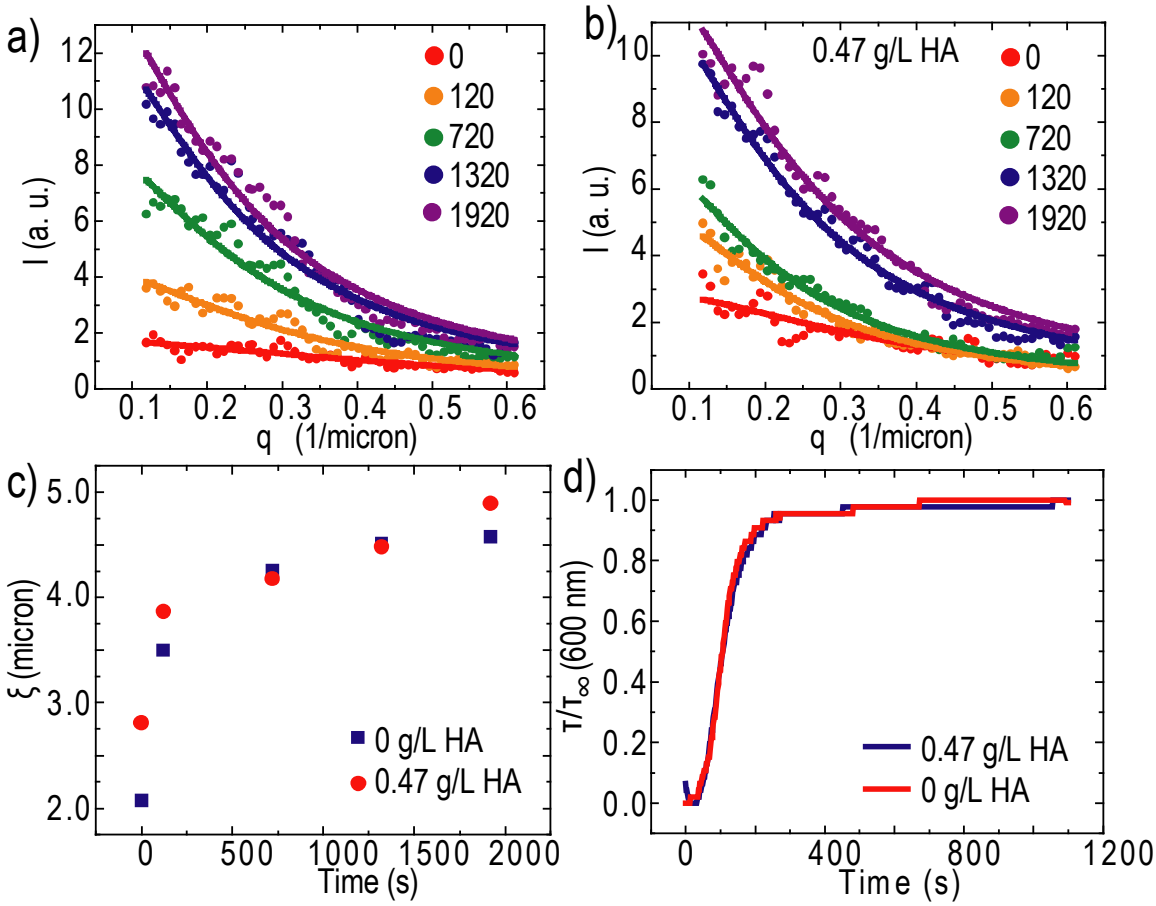

Figure 33.2. Kinetics of collagen type II fiber formation with and without HA. a) SALS data repeated from Figure 5.7. As the fibers self-assemble in solution, the intensity increases and decays faster with *q*, corresponding to an increase in the meshsize. b) SALS data for 0.1 mg/mL collagen at 37ºC, pH 7.2, 0.085 M NaCl, and 0.47 mg/mL HA. The data looks qualitatively similar to the data in a). c) The meshsize calculated from the Ornstein-Zernike fits plotted versus time. The data sets with and without HA for the same salt, pH, and temperature are nearly identical. d) Similar to SALS, turbidity measurements of collagen fibrillization do not change with the addition of HA.

6.3 Swelling of HA hydrogels in the presence of collagen

If the collagen fibers are self-assembled in the solution of cystamine-modified HA and exposed to the air, the network crosslinks around the fibers to form a composite hydrogel. Collagen fibers are much larger than the meshsize of the HA hydrogel and the fibers are effectively trapped. To reach swelling equilibrium, we expose the composite to a salt solution, and assume, because neither component is free to diffuse, that this results in solely a volumetric change, such that the

relative composition of collagen and HA is constant ($k = \frac{\phi_{HA}}{\phi_{col}}$). Using this method, we test the influence of collagen fibers on the swelling equilibrium of HA networks. If the two components are strongly interacting, the swelling of HA will strongly depend on the concentration of added collagen. The final volume fraction of HA, with added collagen is:

$$\phi_{HA} = \frac{\phi_{total}}{1+\frac{V_{col}}{V_{HA}}} \qquad (6.3.1)$$

where ϕ_{HA} is the final volume fraction of HA, ϕ_{total} is the total volume fraction of polymer in the hydrogel, V_{HA} and V_{col} are the volumes of HA and collagen in the system respectively, which remain constant in the experiment. We calculate V_{HA} and V_{col} directly from the initial configuration of the composite networks. For example, if the system starts with 3 mg/mL HA and 1 mg/mL collagen in 1.5 mL, then V_{HA} is 3.9 x 10^{-3} mL, and V_{col} is 1 x 10^{-3} mL.

In Figure 6.3a, we show the effect of added collagen on ϕ_{HA} for swelling equilibrium (as defined in Chapter 4) in 1 M, 0.1 M and 0.01 M NaCl solutions. For equilibrium in 1M NaCl and 0.1 M NaCl, the volume fraction of the HA network is not dependent on the collagen volume fraction. Without added collagen, the volume fraction of the HA network is 0.0017 in 1 M NaCl and 0.0013 in 0.1 M. With $\phi_{col} = 0.0007$ for 1M NaCl and $\phi_{col} = 0.0002$ for 0.1 M NaCl, the volume fraction of the HA network is 0.0017 and 0.013 respectively. In 0.01 M NaCl, on the other hand, the volume fraction of HA seems to increase slightly with the addition of collagen, but is likely within the error of the experiment. Without collagen, $\phi_{HA} = 0.00049$, with $\phi_{col} = 0.0002$, $\phi_{HA} = 0.0053$. As shown in the schematic associated with that figure, regardless of how much collagen is added, the HA network surrounding the fibers swells the same amount in 1 M and 0.1 M NaCl.

The dependence of ϕ_{HA} on ϕ_{col} changes as a function of pH. For gels swollen in 0.01 M NaCl at pH 3.8, pH 6, and pH 9, the result is qualitatively similar to the result at pH 7. The volume

fraction of HA is independent of the collagen concentration within the errors of the experiment. At pH 3.8, ϕ_{HA} without collagen is 0.005, and with ϕ_{col} = 0.0002, the volume fraction increase slightly to 0.008. At pH 6, for $\phi_{col} = 0$, $\phi_{HA} = 0.005$ and for $\phi_{col} = 0.0002$, $\phi_{HA} = 0.008$. At pH 9, for $\phi_{col} = 0$, $\phi_{HA} = 0.008$ and for $\phi_{col} = 0.0002$, $\phi_{HA} = 0.008$. The volume fractions do not exactly match the data set in Figure 6.3a because we used gels from a different synthesis batch. For the lowest pH, the relationship between ϕ_{HA} and ϕ_{col} changes. As shown in Chapter 4, below the pKa of HA, the gels shrink due to the decrease in counterion pressure and ϕ_{HA} increases to 0.003. With added collagen the HA network shrinks monotonically, from ϕ_{HA} = 0.003 at ϕ_{col}= 0 to ϕ_{HA} = 0.004 at ϕ_{col} = 0.0002. At lower pH, collagen is more likely to interact with the HA network because of the homogenous positive charge on the triple helices, described in Chapter 5.

Much like the result in Section 6.2, the independence of the swelling equilibrium of HA gels on the presence of collagen is consistent with an insignificant interaction between the two components in high salt. At low pH and ionic strengths however, there emerges a potential interaction between collagen and HA.

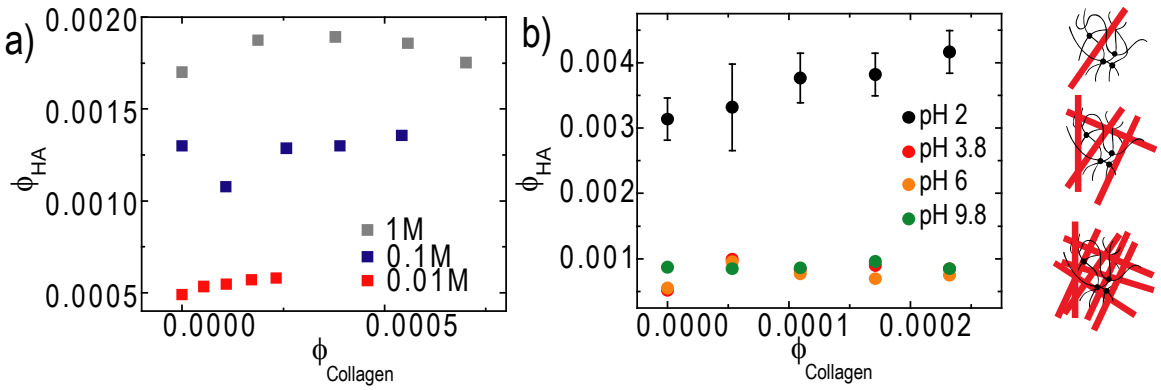

Figure 34.3. Swelling of HA networks with embedded collagen fibers. a) For 1 M, 0.1 M , and 0.01 M NaCl, the volume fraction of the HA network does not have a strong dependence on the added collagen in 20 ºC. b) For 0.01 M NaCl, at high pH, the volume fraction of HA is independent of ϕ_{col}. On the other hand, at pH 2, the HA network shrinks as a function of added fibers.

6.4 Rheology of HA-collagen composite networks

While the addition of collagen does not affect the equilibrium swelling of HA networks, we expect the fibers to impact the elasticity of the network. For composite systems, low volume fractions of rigid fibrous materials reinforce the softer materials in an additive way.[146] The overall modulus increases linearly with the volume fraction of added fibers, and the relative increase is related to the modulus of the fibers themselves. Rigid fibers are more effective at increasing the modulus of the composite than lower-modulus fibers. Collagen is stiffer than the HA gels by orders of magnitude,[20,21,24] so we expect that the addition of even a fraction of collagen fibers strongly increases the modulus of the composite.

We investigate the effect of collagen fibers on the elasticity of the composite networks by measuring G' as a function of ϕ_{col} in HA gels. The result is shown in Figure 6.4. Each color in the plot represents a hydrogel of a fixed HA volume fraction in 0.1 M NaCl. Addition of collagen reinforces the modulus of the composite in a linear way for all hydrogels. This is consistent with the rule of mixtures for fiber reinforced composites, for which the modulus of the network, G'_{total} is:[146]

$$G'_{total} = \phi_{HA} G'_{HA} + \phi_{col} G'_{col} \qquad (6.4.1)$$

A simple rearrangement gives:

$$G'_{total}/G'_{HA} = \phi_{HA} + \phi_{col} G'_{col}/G'_{HA} \qquad (6.4.2)$$

Which is a function linear in ϕ_{col} and describes the relative increase of the modulus with the addition of fibers. The presence of $\phi_{col} = 0.001$ collagen increases the modulus by a factor of 1.75, and the presence of $\phi_{col} = 0.0015$ increases the modulus by 2.2 for gels in equilibrium in 0.1 M NaCl.

The slopes of the linear trends are relates to the relative magnitude of the modulus of the collagen fibers and the soft HA hydrogel matrix. For the networks shown in Figure 6.4, the slopes are 1510, 1420, and 1300 for gels with $\phi_{HA} = 0.0019$, 0.0018, and 0.0014 respectively. Compared to the respective HA network moduli of 2.5 Pa, 3.3 Pa, and 6 Pa, the contributing modulus of the collagen fibers is 4000 Pa, 4500 Pa, and 7800 Pa for each network. The stiffness of the two components is starkly different, which results in the effect that 0.1 v% of collagen fibers doubles the modulus of the composite. The modulus of collagen embedded in the network is lower than expected (1-500 MPa),[22,41] possibly due to the uncertainty of the concentration and structure of collagen fibers within the network. This point warrants a deeper inverstigation, as described in the Conclusion chapter below.

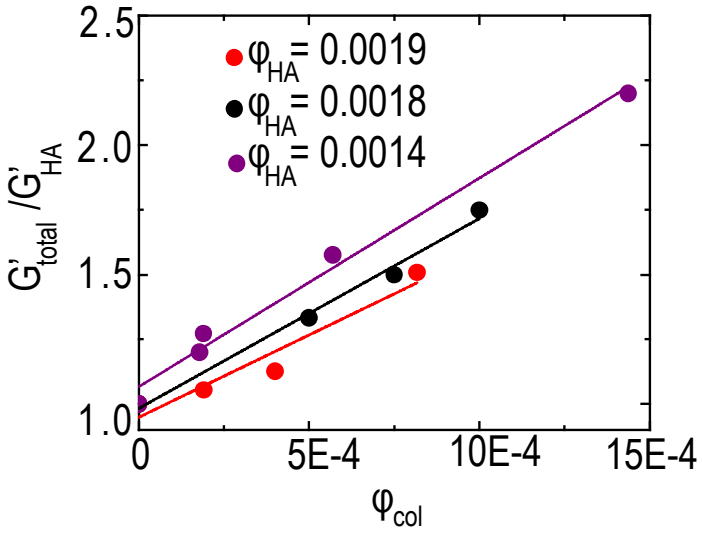

Figure 35.4. Collagen fibers reinforce HA networks. For each HA gel, with a constant *N* (red, black, purple) the addition of collagen linearly increases the modulus of the composite relative to the neat HA networks.

6.5 Conclusions

We have studied the mutual interactions of HA and collagen in the context of the extracellular matrix that makes up the vitreous. At physiological pH and ionic strength, the two components are non-interacting but are mutually reinforcing. As studied by two independent light

scattering experiments, the structure of collagen fibers in the presence of HA does not change, and neither does the time scale of self-association for a set ionic strength and pH. In the presence of the large fibers, the equilibrium volume fraction of HA remains unchanged, consistent with the two component not influencing each other. The lack of interactions greatly simplifies the system. The osmotic pressure of HA remains the same while the soft network suspends the thick collagen fibers. Since the collagen fibers are at least three orders of magnitude stiffer than the HA matrix, the suspended rods increase the modulus of the composite drastically. Varying the osmotic pressure and the modulus of the composites becomes simple; the volume fractions and the moduli of the two components at the physically relevant concentrations are additive.

CHAPTER 7

REPLACEMENT VITREOUS

7.1 Introduction

The failure of the vitreous function leads to many clinically encountered vitreoretinal diseases such as posterior vitreous detachment, retinal detachment, vitreous hemorrhage, and uveitis. In such cases, surgical vitrectomy is required.[38] The gel is removed from the ocular cavity and replaced by either a gas or synthetic material.[39] These options, however, are not ideal and are not long-term.[33] The ideal material should mimic the transport and dynamic properties of the original tissue without damaging the neighboring cells.

The natural vitreous gel is composed of an interpenetrating network of hyaluronan and collagen fibers. The charges on hyaluronan provide an internal pressure to swell the tissue, while collagen fibers increase rigidity. The addition of both permanent charges and a fibrous structural component to the synthetic systems promises to improve structural integrity and compositional density of the injectable synthetic vitreous material. In this chapter we present a new vitreous substitute material which incorporates both charged monomers such as methacrylic acid, and fibrous structures, such as gellan. Starting from a copolymer of methacrylic acid (MAA) with methylacrylamide (MAm) and bismethacryloylcystamine (BMAC), we cross-link gellan to create injectable hydrogels of tunable swelling ratio and dynamics (Figure 7.1b). We characterize these systems using shear rheology, swelling techniques, and dynamic light scattering. In equilibrium in vitro, the density and dynamic response of our synthetic systems are closely matched with previous results describing the vitreous.

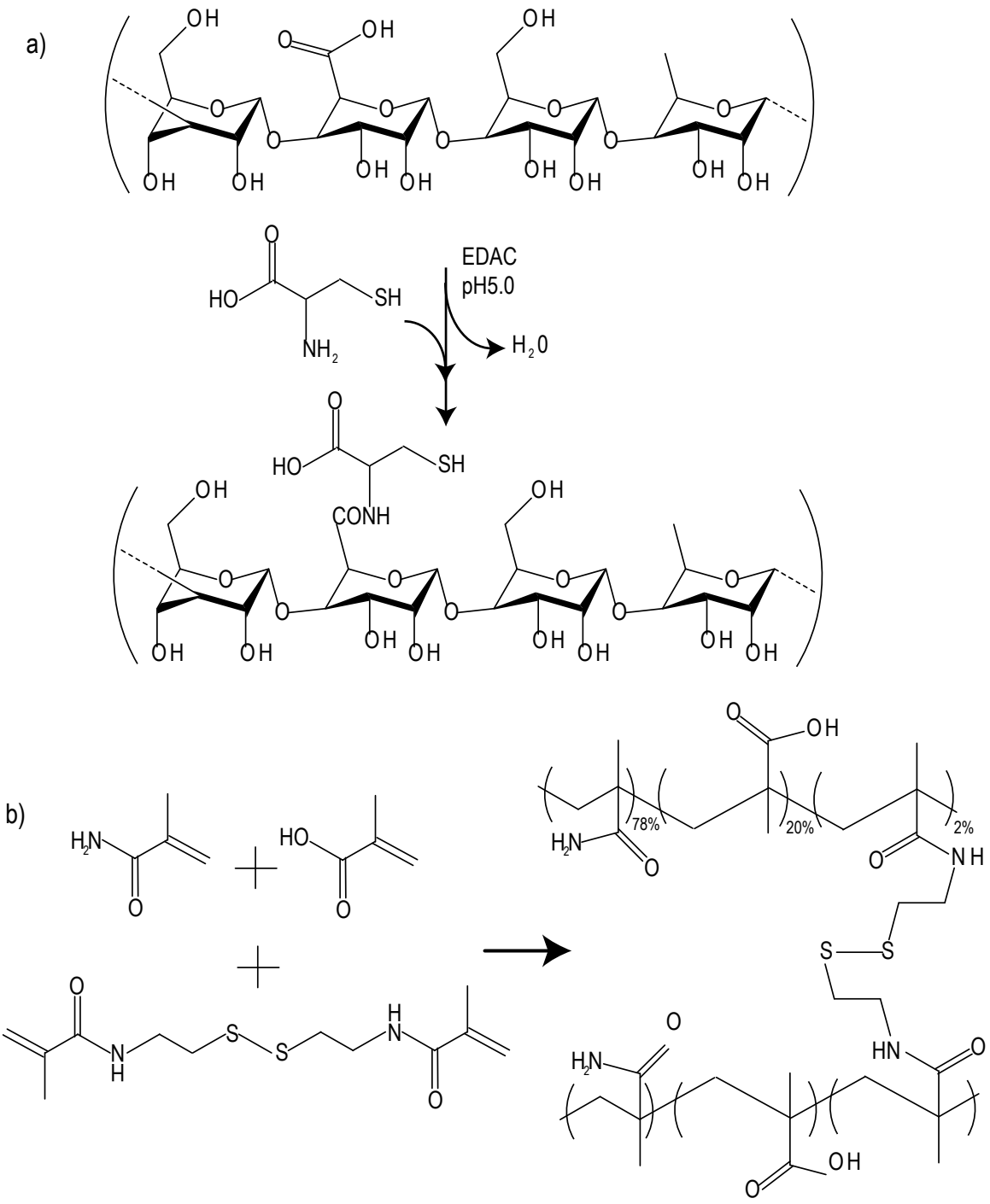

Figure 36.1. Schematics of the chemical structure of the two components of the synthetic vitreous. a) 6.4% thiolated gellan and b) MAm-MAA-BMAC synthetic copolymer with 20% ionizable monomers and 2% cross-links.

7.2 Charged copolymer gels

The addition of charged components to the backbone of the copolymer provides an extra internal pressure. Due to this Donnan equilibrium pressure, the gel will swell compared to the uncharged gel systems.[7,41] The lower volume fraction of the copolymer components of the gel results in a softer gel with greater water content. The swelling equilibrium is also varied with the number of cross-links. The more cross-links in the system, the tighter and less swollen the gel.[7]

To add permanent charges to the network, we copolymerize MAA with MAm and BMAC (Figure 7.1b). The MAA content was fixed at 20% of the total monomers, while the MAm and BMAC was 78%, and 2%, respectively. The synthesis of this molecule is described in detail in Appendix B. Deacylated gellan or gelzanTM (MW 100 kDa), 1-Ethyl-3-(3-dimethylaminopropyl) carbodiimide (EDC), N-hydroxysuccinimide (NHS), cystamine dihydrochloride (Cys), methacrylamide (MAM), 2,2'-azobis(2-methylpropionitrile) (AIBN), sodium sulfite (98%), 5,5′-dithiobis(2-nitrobenzoic acid) (DTNB), dithiothreitol (DTT), and Dulbeco's phosphate buffered saline (PBS) were all purchased from Sigma Aldrich Co. (St Louis, MO) and used as received. Methacrylic acid (MAA, 99%) was purchased from Sigma Aldrich Co. (St Louis, MO) and vacuum distilled before using.

The thiol blocks are responsible for cross-linking, therefore theoretically 2% of the monomers are active for cross-linking. All thiol content has been verified with a 2-nitro-5-thiosulfobenzonate NTSB assay. The final concentration of the copolymer dictates the dynamic response and water content of the synthetic networks. We tune this concentration to match the water content of the vitreous tissues by varying the total concentration of the copolymer during gelation. Increasing the initial concentration of the copolymer during gelation, while keeping the total volume constant increases the cross-link density of the gels, which stiffens the gels.

The addition of charges leads to more swollen gels. To measure the polymer volume fraction of our gels, ϕ, in equilibrium with a phosphate buffered saline (PBS) solution, we weigh the gels after they have been washed exhaustively with PBS. In general, the final volume fraction is related to the volume of the swollen gel and the volume of the dry gel:

$$\phi = \frac{V_{dry}}{V_{swollen}} = \left[1 + \frac{\rho_p}{\rho_s}\left(\frac{M_b}{M_a}\right) - \frac{\rho_p}{\rho_s}\right]^{-1} \qquad (7.1.1)$$

Here ρ_p and ρ_s are the densities of the polymer and solvent respectively, while M_b is the mass of the swollen gel and M_a is the mass of the dried gel. These equations simplify considerably under our assumption of densities of all components being 1. In the presence of salt, theoretical expressions for the swelling equilibrium are known based on screened electrostatic expansion and Donnan equilibrium. As the primary goal of the present thesis chapter is not molecular interpretation of observed properties, it suffices to state that salt concentration is equivalent to making the swelling weaker.

The final volume fraction of the copolymer with initial formulations of 1.8, 1.55, and 1.35 w% are shown in Table 7.1. The gels swell, resulting in respective volume fractions of 0.009, 0.008, and 0.007.

In equilibrium with PBS solutions, the shear modulus of charged copolymer gels depends on the volume fraction. Usually, the gels are brought to equilibrium to match the plate geometry, in our case cylinders with a 40 mm diameter. The gels were typically 200-1000 μm in height to facilitate rheological experiments.

Constant amplitude frequency sweeps from 0.1 Hz – 1 Hz were used to measure the storage (G') and loss(G") modulus of each gel at 37°C on a AR2000, a TA Instruments rheometer. The amplitude was chosen so that the measurements were in the linear-elastic regime. This was tested by measuring the modulus with increased amplitude for a 0.1 Hz shear rate for each gel. The

experiment remained in the linear-elastic regime until ~3% strain. 1% strain was chosen for all rheological experiments. Each measurement was the result of an average of 20 oscillations.

In Figure 7.2 we plot the shear and storage modulus as a function of frequency. For all gels, the frequency response is constant, and G' is an order of magnitude larger than G". This frequency response is suitable for vitreous substitution.[1,33–37] The stiffness of the gels increases with the density of the copolymer in the gel (Table 7.1). For gels with equilibrium polymer volume fraction equal to 0.007 the modulus is 7 ± 1.5 Pa. For gels with equilibrium polymer volume fraction equal to 0.009, the modulus is 15 ± 3 Pa.

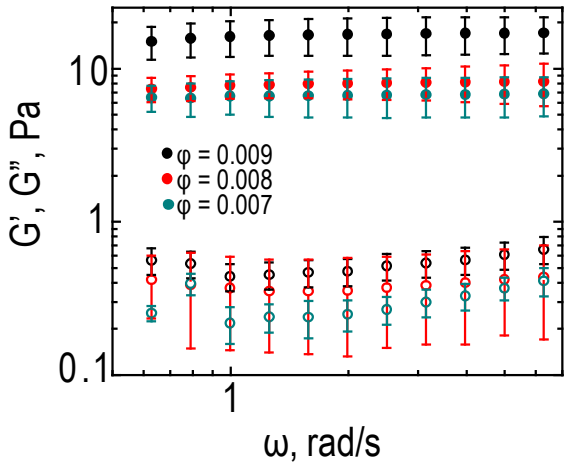

Figure 37.2. Dynamic response of charged MAm-MAA-2%BMAC copolymer gels at 37°C. The filled circles depict the elastic modulus, G', and the hollow circles depict the storage modulus, G". Since the frequency response is constant, the gels are considered elastic solids. The modulus increases with the copolymer volume fraction. The error bars indicate the standard deviation of three trials for the same gel.

The dynamic light scattering results show a similar trend to the shear rheology results. For gel systems, the electric-field correlation function is proportional to the time averaged correlations of the density fluctuations. The elastic diffusion is therefore related to the dynamic response of the gel as outlined in the Chapter 3. Typically for gels, the correlation function does not show a single decay, but rather a dominant decay with a distribution of other relaxations due to inherent inhomogeneities from clustering of cross-links and other impurities. These inhomogeneities are responsible for the nonergodicity of the networks. As outlined in the Chapter 3, there are several

analysis methods which are used to determine either the apparent elastic diffusion coefficient of the network, D_A or the true elastic diffusion, D. While CONTIN and multiple exponential fits give D_A, heterodyne analysis evaluates the relaxation times only from the fluctuating component of the gel, from which we measure the true elastic diffusion coefficient, D. The two measured quantities are related by Eq. 3.5.4. In Figure 7.3, we compare the angle dependence of all relaxation times for all three analysis methods. The values obtained by CONTIN and multiple-exponential fits are consistent within experimental error. As expected, the true elastic diffusion values calculated using heterodyne analysis are a factor of 1-2 greater (Figure 7.3).

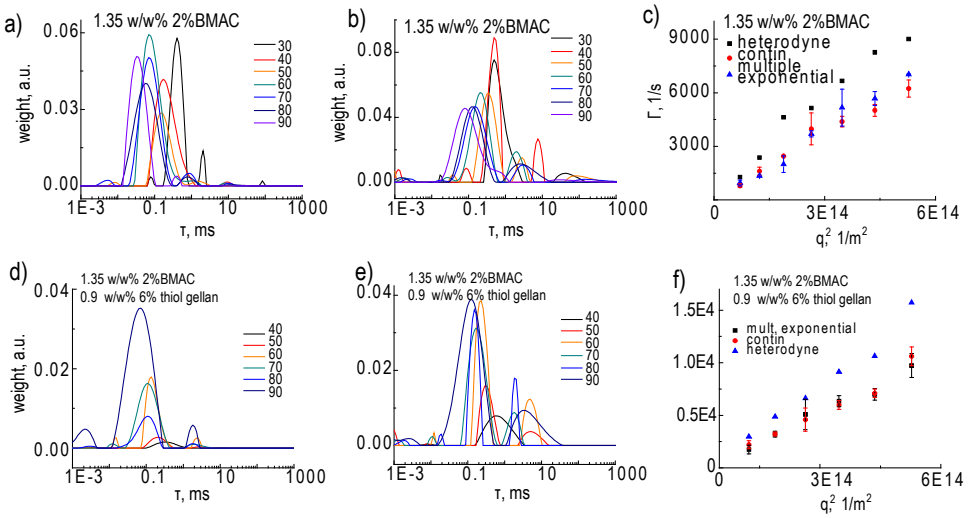

Figure 38.3. Comparison of three different DLS analysis methods: CONTIN, heterodyne detection CONTIN, and multiple exponential fits for MAm-MAA-BMAC copolymer network and MAm-MAA-BMAC copolymer-gellan double networks. a) Heterodyne CONTIN distribution functions for each decay rate for angles 30-90 for a typical copolymer gel. In this case the gel is 1.35 w/w% starting concentration with 2%BMAC. b) CONTIN analysis of the same gel. CONTIN analysis shows a clear dominant mode along with multiple other distributions per angle. c) The decay rate as a function of the square of the scattering vector for the three analysis methods. CONTIN and multiple exponential analysis are within experimental error of each other, while heterodyne detection shows consistently 1-2 times higher decay rates as expected for a non-ergodic system. d)-f) typical results for the double network show similar trends as just the pure copolymer network.

For our analysis, we compare the MAm-MAA-2%BMAC copolymer gel networks by focusing only on the most dominant mode from multiple exponential fits and CONTIN heterodyne detection (Figure 7.3, 7.4, 7.5). This is the only mode that has a clear angle dependence, shown in

Figure 7.3 and Figure 7.4. Typically the other 1-2 modes present in the system contribute to less than 25% of the correlation function description and do not have an angle dependence (Figure 7.4). In Figure 7.3c,f and Figure 7.5b, we show that the relaxation rate associated with this mode is linear with the square of the scattering angle. From this we conclude that the mode is due to the density fluctuations of the gels. Using the slope of the linear lines, we calculate the elastic diffusion coefficient. This quantity increases with the polymer volume fraction. In Table 7.1 we summarize the results of the dynamics for our gel systems, based on the rheological data, and data obtained from dynamic light scattering. For copolymer gels with ϕ = 0.007, 0.008 and 0.009, the apparent diffusion coefficient is 1.3 ± 0.2 x 10^{-11} m^2/s, 2.2 ± 0.3 x 10^{-11} m^2/s, and 2.7 ± 0.3 x 10^{-11} m^2/s, respectively, with the fluctuating component contributing to more than 50% of the total intensity. The true diffusion coefficient, measured from just the fluctuating components of the gel is 1.7 ± 0.3 x 10^{-11} m^2/s, 2.7 ± 0.4 x 10^{-11} m^2/s, and 4.2 ± 0.5 x 10^{-11} m^2/s for the same gels, respectively.

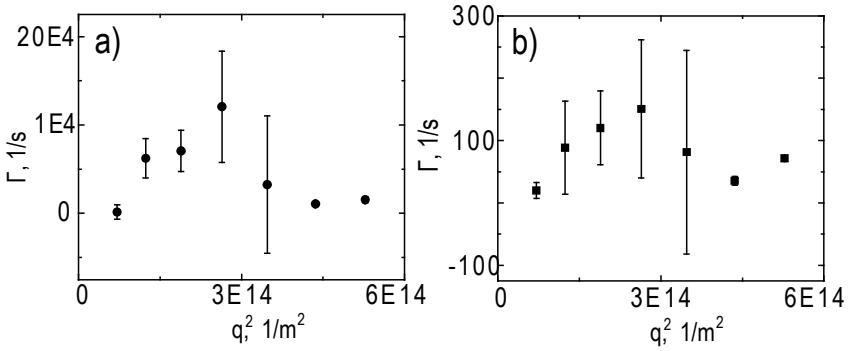

Figure 39.4. The typical angle dependence of two other modes in the triple-exponential fit for 2%BMAC copolymer gel with starting polymer concentration of 1.35 w%. The weights for these modes were 12 and 13% of the total number respectively.

Table 2.1: Dynamics of charged 2%BMAC copolymer gels

Equl. ϕ	G' (Pa)	G" (Pa)	$D_A x 10^{11}$ (m^2/s)	$Dx10^{11}$ (m^2/s)	X
0.007	7 ± 1.5	0.8 ± 0.05	1.3 ± 0.2	1.7 ± 0.3	0.7
0.008	8 ± 1.5	0.4 ± 0.2	2.2 ± 0.3	2.7 ± 0.4	0.8
0.009	15 ± 3	0.5 ± 0.1	2.7 ± 0.3	4.2 ± 0.5	0.5

In comparison with previously-studied disulfide-cross-linked acrylamide gels, in our systems 20% of all monomers are ionizable. Because of the added permanent charges in the system, the gels swell considerably more in equilibrium, which leads to a lower modulus than for copolymer gels without ionizable monomers. From studies published by Swindle et al, the uncharged analogues of our copolymers have a modulus two order of magnitude higher, at a range of 240-582 Pa, depending on the density and number of cross-links.[84]

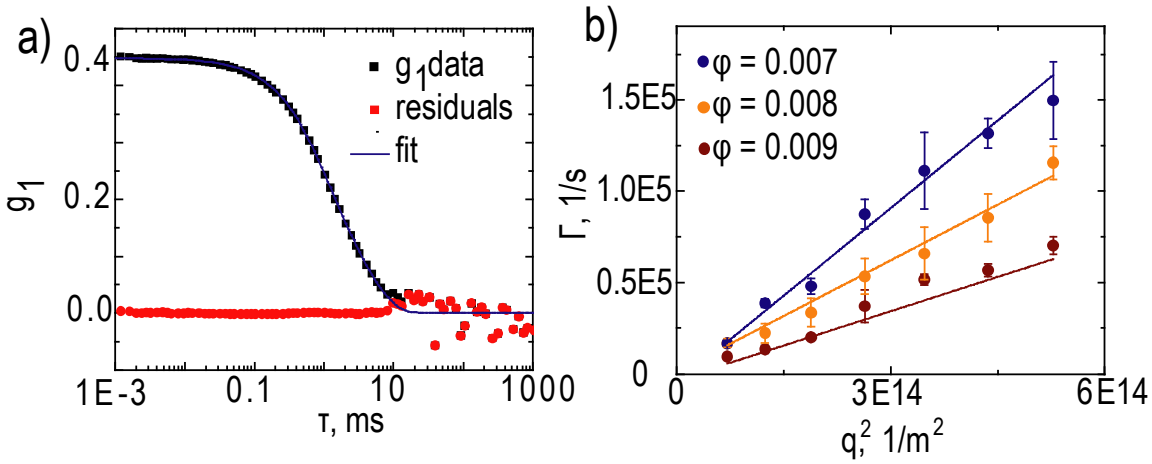

Figure 40.5. Dynamic light scattering analysis for 2%BMAC copolymer gels at 37°C. a) Representative g_1 correlation function for 30° angle. The blue line is a triple-exponential fit, which fits for all angles, based on the residue analysis (red squares). b) The decay rate of the dominant mode from the multiple exponential fits in a). The decay rate is linear with the square of the scattering vector, q. From the slope, we calculate the apparent elastic diffusion coefficient, which increases for denser gels. The error bars indicate the standard deviation of three different spatial locations within the gel.

7.3 Incorporating gellan

The copolymer gels with ionizable monomers described above are swollen, but too soft to be viable vitreous substitutes. To increase the modulus of our copolymer gels to more closely match that of the vitreous, we incorporate fibrous structures. Gellan gels in a hyaluronic acid matrix have been previously considered as injectable vitreous substitutes, and have exhibited great biocompatibility, as pointed out in Chapter 1. One advantage of gellan is that the polysaccharide coils into double-helixes spontaneously at room temperature.[81,82] In the presence of divalent salt

ions these double-helixes are attractive, and act as physical cross-links in the system (Figure 7.6a). These physical cross-links are fibrous in nature, as shown by atomic force microscopy by Gunning *et al.*[82] The helices melt at above a critical temperature, which allows us to pass these materials through a syringe needle without compromising the structure.

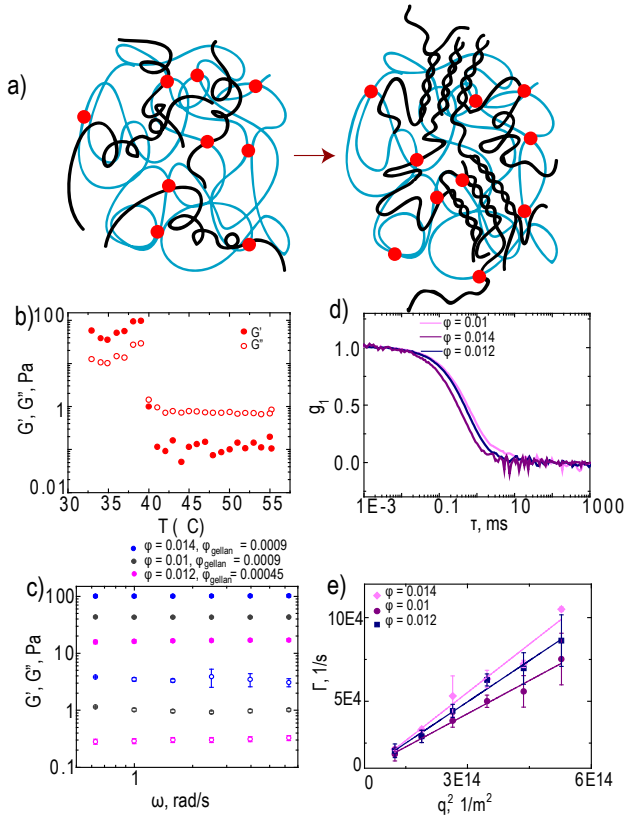

Figure 41.6. Dynamic response of the double-network MAm-MAA-BMAC – gellan gels. a) Schematic of cross-linked gellan-copolymer gels. Blue is the copolymer matrix cross-linked to the gellan network shown in black. The gellan network undergoes a coil-helix transition in the presence of divalent ions. b) Thermal scan of 0.09 w/w% gellan with 0.9 w/w% MAm-MAA-2%BMAC copolymer networks showing a transition gelling temperature between 40 and 39°C. c) G' and G" as a function of frequency and double-network composition at 37°C. The response is independent of frequency and highly dependent on the presence of gellan. d) Overlay of normalized g_1 correlation functions of double network gels at 40° scattering angle and 37°C for three different compositions: 0.09 w/w% gellan with 1.35 w/w% 2%BMAC copolymer and 0.9 w/w% 2%BMAC copolymer, and 0.045 w/w% gellan with 1.35 w/w% 2%BMAC copolymer. The total equilibrium volume fractions of these compositions are 0.014, 0.01, and 0.012, respectively. e) The relaxation rate as a function of the square of the scattering vector for the three different interpenetrating networks described in d). The error bars indicate the standard deviation of three different spatial locations within the gel.

The sol-gel transition characteristic of each Mam-MAA-BMAC – gellan composite networks was carried out using a Vilastic-3 oscillatory tube rheometer (Vilastic Scientific Inc., Austin, TX). A thermal scan with 5% constant shear strain and 1.0 Hz constant frequency was used to measure the transition point of the hydrogel by cooling the samples from 55 °C to 15 °C, equilibrating within 0.1 °C at each point as described. A 3x molar excess of glutathione was added to the samples during measurement to prevent disulfide cross-linking. To measure the transition temperature, we add a reducing agent to prevent covalent cross-linking of the network. In Figure 7.6b we show that for the 0.9 w% 2%BMAC copolymer gels with 0.09 w% gellan, the gelling temperature is around 40°C. In physiological conditions, for which the temperatures are stable around 37°C, gellan will remain in the associated-helices phase for the gels in our study.

In Figure 7.5c-e and Table 7.2 we show the dynamic response of 2% BMAC copolymer gels with 0.09 w% and 0.045 w% of gellan at 37°C. The 6% thiol-modified gellan is cross-linked to the copolymer, increasing the modulus in two ways: by (1) increasing the number of chemical cross-links, and by (2) increasing the number of physical cross-links (Figure 7.6a). As summarized in Table 7.2, the addition of gellan strongly reinforces the copolymer matrix. While the 2% BMAC copolymer solution at initial concentration of 0.9 w% did not gel, addition of 0.09 w% of 6% modified gellan into the same total volume leads to a stiffer, swollen gel of 43 Pa with a final equilibrium volume fraction of 0.01. For a similar volume fraction without gellan, the copolymer matrix modulus is 3 times smaller, at 15 Pa. In a similar trend, reducing the weight fraction of gellan by a factor of 2 greatly reduces the modulus from 104 Pa to 17 Pa (Figure 7.6c).

Because of the greater number of both physical and chemical cross-links, the final concentration of gellan-copolymer gels is much higher than just single-network Mam-MAA-2%BMAC gels. The total concentration of polymer is shown in Table 7.2. Minimal swelling was observed from the initial composition. The increased polymer concentration in equilibrium contributes to the gel's enhanced dynamic response.

Dynamic light scattering on the copolymer-gellan gels provides more information about the network. While in rheological data, we find that the modulus is highly sensitive to the volume fraction of the gellan network, the total volume fraction of the double network gel dominates the DLS results. In Figure 7.6d, we compare the correlation function at 40^o for three different compositions of double network gels. The results are also summarized in Table 7.2. For denser gels, the relaxation time decreases systematically. More quantitatively, we measure the apparent elastic diffusion coefficient from the decay time data at 6 angles. In Figure 7.6e, we show that decay rate for the dominant mode of the system, Γ, is linear for all angles and for all gels studied. From the slope of these linear trends, we show the apparent elastic diffusion coefficient, the true elastic diffusion coefficient and the ratio of the fluctuating to static intensity, X, in Table 7.2. For denser gels the density fluctuations relax systematically faster. The trends scale with the total volume fraction of the gels, which is dominated (>90%) by the copolymer composition. The fluctuating component for these systems is consistently 50-60% of the total intensity.

Table 3.2: Shear rheology of charged 2%BMAC copolymer gels with varied amount of gellan.

2%BMAC ϕ	6%gellan ϕ	Total ϕ	Equil. G' (Pa)	G" (Pa)	D_A (m^2/s) x 10^{11}	$D(m^2/s)$ x 10^{11}	X
0.009	0.0009	0.01	43 ± 2	1 ± 0.1	1.3 ± 0.2	2.1 ± 0.3	0.5
0.0135	0.0009	0.014	101 ± 5	3 .5± 0.5	2.0 ± 0.3	2.9 ± 0.4	0.5
0.0135	0.00045	0.012	17 ± 1	0.5 ± 0.1	1.7 ± 0.1	2.3 ± 0.1	0.6

Crosslinked gellan-copolymer gels are up to 99.9-99.86 % water by volume, with polymer volume fractions between 0.01-0.014, and are still able to maintain an elastic response in a range of 2-101 Pa, depending on the formulation. This closely matches the volume fraction of the vitreous, which is estimated to be 99.94% water and soluble small molecules by volume. According

to rheological studies done on the natural vitreous in vitro, the modulus of the tissue is 57 Pa according to Swindle et al.[84], 120 Pa according to Zimberlin *et al.*[147], 50 Pa according to Zimmerman *et al.*[148], 7 Pa according to Nickerson *et al.*[149], and 1 Pa according to Sharif-Kashani *et al.*[150] Our values fall well within this range. The dynamic light scattering data is also close to the in vitro values of the vitreous. For the vitreous, the fastest elastic mode corresponds to an elastic diffusion coefficient of 0.6 - 1 x 10^{-11} m^2/s, depending on the position of the scattering center. Assuming that the synthetic networks are incompressible with a Possion's ratio of $v \sim 0.49$, we use our rheological data along with the dynamic scattering results to estimate the friction coefficient, f with Eq. 4.6.2. For the gellan-copolymer interpenetrating gels, we find a range of 0.4-2.2 x 10^{10} Pa s / cm^2 for the friction coefficient, which is in the same order of magnitude as the natural tissue, which has a friction coefficient, $f_{vitreous}$ = 6.4 x 10^{10} Pa s /cm^2 as measured by Matsuura *et al.*[151]

7.4 Conclusions

We present a new synthetic vitreous substitute formulation. The composition of the material, which includes ionizable monomers and fibrous structures is inspired by the natural tissue, to better match the criteria for a therapeutic material. These gels swell due to the added charge density and are reinforced by gellan fibers. The addition of ionizable monomers increases the swelling, or the water content of the gels. This property is crucial to keep the optical clarity and transport properties of the gels similar to the natural vitreous. The MAm-MAA-2%BMAC copolymer gels without gellan are too soft by themselves, and the rheological response does not match stiffness of the natural tissue. We achieve the improved dynamic response of the networks by cross-linking gellan to the copolymer gels. Below 40°C, gellan gels spontaneously undergo a coil-helix transition in the presence of the copolymer. The helices are attractive and provide physical cross-links to the double network. We measure these improved dynamics using both DLS

and rheology. The addition of just 0.045-0.09 w% of thiolated gellan leads to an order of magnitude increase in the modulus, and allows us to fine tune the dynamic response without affecting the underlying porous matrix. The result is a tunable synthetic double-network hydrogel material which fulfills the criteria for a long-term vitreous substitute. Further investigations related to injectability and cytocompatibility *in vivo* of the present material are in progress and will be addressed in future publications.

CHAPTER 8

CONCLUSIONS AND PROPOSED EXPERIMENTS

8.1 Conclusions

We have shown how the two main components of the vitreous are responsible for the physical properties of the tissue. Vision is only possible through macromolecular principles, charged components, and transfer of light and ions. The anionic polysaccharide HA swells to reach an osmotic pressure equilibrium. The volume fraction predictably determines the elasticity and ocular pressure of the vitreous. The second major component, collagen, spontaneously self-assembles into large fibers. The fibers are stabilized by pair-wise electrostatic interactions. The 100-600 nm diameter fibers reinforce the soft HA matrix and provide structural integrity to the vitreous. HA swells to suspend collagen and prevents sedimentation of the microscopic structures. We observe little evidence of enthalpic interaction between collagen and HA. The two components are arranged in a mutually supportive way to provide optical clarity, structural integrity, and porosity to the interior of the eye.

Using the fundamental insights from our systematic investigations, we have engineered a suitable synthetic therapeutic material. We have incorporated charged components such as the ionizable methacrylic acid, and injectable structural components such as associating gellan helixes into a thiol-crosslinked composite. The swelling equilibrium polymer volume fraction, elasticity, and porosity match those of the natural tissue. The synthetic solid material is biocompatible and injectable, and promises to be a better therapeutic material.

There are still remaining challenges. Most notably, the mechanism of vitreous failure is unknown. Insight into the mechanism of vitreous liquefaction and subsequent detachment will contribute to the developments in therapeutic prevention of the disease. As of now, there are two

most probable pathways for vitreous failure. The vitreous may fail in a mechanical way, or phase separate.

Changes in the solvent quality or body homeostasis may lead to thermodynamic instability of the HA-collagen network. At physiological temperatures and salt concentrations, $X_{HA-H_2O} \sim 0.499$, close to a critical value at which phase separation occurs. In the event of phase separation, the tissue will divide into a polymer-rich and a polymer-poor phase, and lead to macroscopic inhomogeneities.[30] In order to investigate the criteria for this process, we propose swelling studies in more complex solutions. Other amino acids and more complex salts change the quality of the solvent and may be responsible for elevating X above the critical value.

The second potential mechanism of vitreous failure is mechanical. As we have shown in Chapter 5, collagen structure depends on the ionic strength of the solution. The origin of the size scale and whether it evolves with either further addition or dilution of the ionic strength is still an open question. We therefore propose neutron and light scattering investigation of collagen fibers embedded in an HA matrix, swollen in different ionic strength conditions. Measuring both the meshsize and the collagen fiber concentration for each case will provide evidence of structural change. If collagen structure and concentration is disrupted, the composite tissue loses its mechanical integrity and becomes prone to tearing and other mechanical failure.

8.2 Neutron scattering

Collagen type II self-assembles into fibers, and in the vitreous the fibers are about 30 nm in diameter so that the overall gel is transparent to natural light. As the tissue ages, problems manifest themselves through a loss of vitreous structure and rigidity. Sebag et al.[3,6] correlated this loss of structure to an appearance of thicker collagen fiber bundles, and an overall increase in the inohomogeneity of the matrix. The HA concentrations remains constant throughout the vitreous,

while the collagen structure and organization is changed. We propose a neutron scattering study to systematically examine how the elasticity and the salt concentration of model vitreous-like composites contribute to the correlation length and structure of collagen fibers. Using the Ornstein-Zernike approximation, the thermodynamic parameters such as the effective ternary χ- parameter will be calculated as a function of salt concentration and HA volume fraction. These results will allow us to have a deeper understanding of the mechanism of the age-related vitreous changes.

We propose to synthesize the hyaluronic acid networks by lightly cross-linking HA. Using triazene coupling we chemically modify the HA carboxylic groups with 0.5 - 2.5% cystamine. For a specific salt concentration, the modulus depends on the cross-linking and can be varied by an order of magnitude, from G'= 2 Pa to G'= 20 Pa. These elasticities mimic the vitreous modulus at the same volume fraction of hyaluronic acid. The collagen fibers are self-assembled in the network in various salt concentration at pH 7.4. The resulting structure and volume fraction greatly depends on the salt concentration in pure water. HA-collagen type II composites can be equilibrated against solution of water and deuterium with different salt concentrations, [I] = 0.05 - 0.5 M.

In the case of a three-component system consisting of HA, collagen fibers, and solvent, the scattering intensity function is:[134]

$$I(\mathbf{q}) = \phi_{HA}\phi_S(\rho_{HA} - \rho_S)^2 S_{HA-HA}(\mathbf{q}) + \phi_{col}\phi_S(\rho_{col} - \rho_S)^2 S_{col-col}(\mathbf{q}) + 2\phi_{HA}\phi_{col}(\rho_{HA} - \rho_S)(\rho_{col} - \rho_S) S_{col-HA}(\mathbf{q}) \qquad (8.2.1)$$

where ϕ_i and ρ_i are the volume fraction and the scattering length density of each component. $S_{HA-HA}(\mathbf{q})$, $S_{col-col}(\mathbf{q})$, and $S_{col-HA}(\mathbf{q})$ are the HA-HA, collagen-collagen, and collagen-HA structure factors, respectively. By swelling the composite network in a D_2O – H_2O mixture, we can tune ρ_S to equal ρ_{HA}, and Eq. 8.2.1 becomes:

$$I(\mathbf{q}) = \phi_{col}\phi_S(\rho_{col} - \rho_S)^2 S_{col-col} \qquad (8.2.2)$$

The only scattering possible in this situation is from the collagen fibers embedded in the matrix. The neutron scattering length density of the HA matrix and collagen fibers are estimated using $SLD = \sum_i b_i \frac{dN_A}{M_w}$. Where b_i is the scattering length of *i*th atom, d is the mass density of the scattering body, M_w is the molecular weight, and N_A is the Avogadro's constant. An HA monomer is composed of C14H21N1O11, and has a specific gravity of 1 g/cm^3. Collagen type II monomers are inherently more complicated since collagen triple helices are composed of more than 4000 amino acid residues. However, about 66% of this sequence has a distinct repeat structure of Glycine-Proline-Hydroxyproline. The composition for this sequence is C12H24N3O7, with a specific gravity of $1.3 - 1.4\ g/cm^3$. The SLD's for the HA matrix and collagen are $1.39 \times 10^{-6}\text{Å}^{-2}$ and $1.53 \times 10^{-6}\text{Å}^{-2}$ respectively. The background HA matrix can be effectively contrast-matched by swelling the gels in a deuterium oxide - water mixture of 0.285:0.715 composition.

If this contrast is too small to observe the collagen in solution, another approach is to swell the composite system in pure D_2O, while keeping the HA volume fraction an order of magnitude lower than the collagen volume fraction. For large molecular weights between cross-links, the volume fraction of HA can be as low as 0.0005. This experiment would require a control, for which we'll systematically increase the HA concentration from 0 to observe any contribution of the elastic component to the total intensity.

8.3 SALS experiments

In tandem, we propose a series of similar light scattering experiments. The collagen-HA composite network is an ideal way to study the effects of changing ionic strength to the structure of pre-formed collagen fibers. The HA network suspends collagen without interacting with the fibers strongly. We propose investigating collagen structure using SALS and concentration for

composite systems in varied ionic strengths. The meshsize measured from SALS experiments is related to the concentration of collagen fibers, and is independent of the radius of gyration:

$$\xi \sim R_g^0 c_{fiber}^{-\frac{1}{2}} \qquad (8.3.1)$$

To investigate any structural changes in the composite, we propose to independently measure both collagen concentration using a calibrated staining technique and the meshsize. The $\xi c_{fiber}^{\frac{1}{2}}$ quantity is expected to be constant if changing the coulombic environment does not influence collagen fiber structure. Any deviation from this expected behavior will provide crucial structural information.

8.4 Calculating *X* in amino acid rich solvents

To investigate the criteria for phase separation, we propose to systematically vary the solvent quality, and measure the gel response. In Chapter 4, we have shown an experimental protocol which may be used to investigate the thermodynamic quantities, X and α, of hydrogels. In water and NaCl solutions, we have not observed phase separation of HA gels due to high ionizability of the backbone of HA. However, the vitreous is swollen in a more complex solution of amino acids, higher-valance salts, and proteins. Animo acid rich solutions may drive the system to phase separate. We propose to systemtally increase the concentration of animo acids and investigate the change in X and α to examine the criteria for phase separation in HA gels.

APPENDICES

APPENDIX A

INFLUENCE OF DIPOLE ORIENTATION ON SOLUTION PROPERTIES OF POLYZWITTERIONS

A.1 Introduction

Polyzwitterions are composed of repeat units having permanent charge pairs, or dipoles. The dipoles, prescribed by the chemical structure, can be oriented towards the backbone of the polymer chain (as in polysulfobetaine), or away from the backbone (as in poly(2-methacryloyloxyethyl phosphorylcholine) (PMPC), **1**). In general, polyzwitterions exhibit unique solution behavior due to these dipoles.[152–155] Since dipole-dipole interactions are electrostatic in nature, the assembly processes with polyzwitterions can be tuned with experimental variables that affect electrostatics, such as ionic strength. In general, the polyzwitterion behavior depends on the dipole density along the chain, the dipole length, identities of the charges of the dipole, and the local dielectric properties.[156–164]

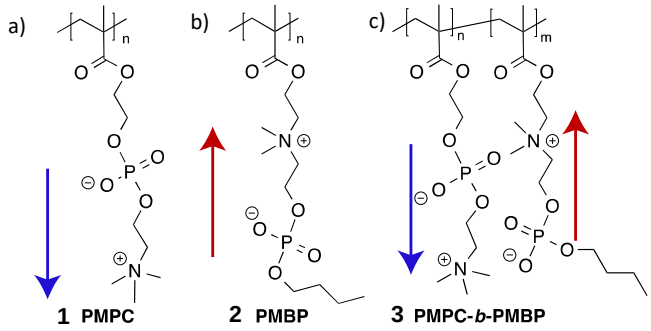

Figure 42.1. Structures of polyzwitterions: PMPC (1), PMBP (2) and PMPC-b-PMBP (3).

There has been extensive characterization of polyzwitterion solutions, for example using viscosity, osmometry, turbidity, light scattering, and phase behavior.[165–171] These studies show that in dilute solutions individual chains of polyzwitterions exhibit chain swelling upon an increase in added salt concentration. Such an effect, called anti-polyelectrolyte effect due to its

reverse trend from uniformly charged polyelectrolyte chains, has attracted significant theoretical modeling and experimental efforts.[101,102,172–174] At lower salt concentrations, the dipoles organize in an anti-parallel manner and upon addition of salt they un-pair due to electrostatic screening and thus the coils open into swollen conformations.

The effect of dipole orientation on the salt responsiveness and association of polyzwitterions in solutions has not yet been studied systematically. The focus of this Appendix is to compare the behavior of two polyzwitterion homopolymers having opposite dipole orientations, as well as the corresponding block copolymer, in which the different dipoles are isolated into separate blocks. Using dynamic light scattering (DLS), we have investigated the solution properties of PMPC (**1**), *n*-butyl choline phosphates (PMBP, **2**), and a PMPC-*b*-PMBP diblock copolymer (**3**),[175] each of which was prepared using controlled polymerization methods. Indeed, dramatic differences in the aqueous structures were found in these three systems, confirming that dipole directionality and functionality combine to impact structure formation in dilute solutions.

A.2 Materials and Methods

A.2.1 Materials

Starting materials, reagents and solvents were purchased from Sigma Aldrich and used without further purification unless otherwise stated. 2-methacryloyloxyethyl phosphorylcholine (MPC) and MBP monomer was prepared according to our previous paper. Chemical analysis was performed using NMR and GPC.[100,175]

A.2.2 Polymer Synthesis

PMPC (**1**) and PMBP (**2**) homopolymers and PMPC-*b*-PMBP (**3)** diblock copolymers were prepared by atom transfer radical polymerization (ATRP) according to our previous paper.

Homopolymerizations were conducted using copper (I) bromide as catalyst, 2,2′-bipyridine (bpy) as ligand and ethyl α-bromoisobutyrate (EBiB) as initiator in a [CuBr]:[bpy]:[EBiB] 1:2:1 molar ratio to give polymers **1** and **2**. PMPC-*b*-PMBP (**3**) was prepared by chain extension of PMPC macroinitiator **1** with MBP monomers. All of the polymers were purified by precipitation in diethyl ether, followed by dialysis in deionized (DI) water. Lyophilization gave the polymer products as white solids. Theoretical molecular weights and number average degrees of polymerizations (D_p) of the PMPC and PMBP homopolymers were estimated from monomer conversion, which was determined by ^{1}H NMR spectroscopy. D_p of the extended MBP chain in PMPC-*b*-PMBP was estimated using the molar ratio of MPC and MBP in the final product by ^{1}H NMR,[175] which is also consistent with the result calculated by MBP monomer conversion. Molecular weights and polydispersities (PDI) were estimated by GPC with refractive index detection, employing 1,1,1-trifluoroethanol (TFE, with 0.02 M sodium trifluoroacetate) as the mobile phase.

A.3 Results and Discussion

We performed static and dynamic light scattering on three polyzwitterion systems: (a) PMPC, where the segmental dipole is directed away from the polymer chain backbone, (b) PMBP, where the segmental dipole is directed towards the chain backbone, and (c) a diblock polymer composed of PMPC and PMBP. Remarkably, we find that both PMBP and its block copolymer with PMPC self-assemble into aggregates, whereas PMPC itself does not produce aggregates under the experimental conditions of the present study.

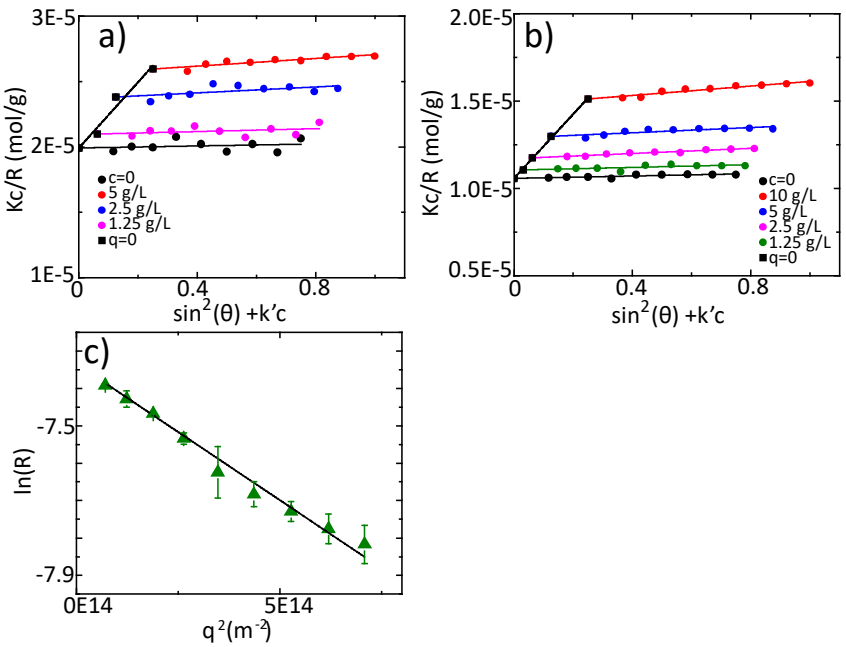

Figure 43.2. Static Light Scattering analysis of polyzwitterions. a) Zimm plot for PMPC107. b) Zimm plot for PMPC 200. c) Guinier Plot for the intensity contribution from RH2 in PMBP164 solutions. Rg values are obtained from the slopes of the linear fits.

The solution behaviors of aqueous PMPC (**1),** with two different chain lengths (PMPC200 and PMPC107, D_p 200 and 107, respectively) were investigated at 20 °C. For PMPC200, the Zimm analysis (see Figure A.2) gives the molecular weight M, R_g, and A_2 as 90,000 g/mol, 9.5 nm, and 4E-6 mol cm^3/g^2. The corresponding values for PMPC107 are 50,000 g/mol, 7.3 nm, and 4E-6 mol cm^3/g^2. The weight averaged molecular weights determined from the Zimm analysis are consistent with the GPC data (75,000 g/mol and 42,000 g/mol, respectively for PMPC200 and PMPC107).

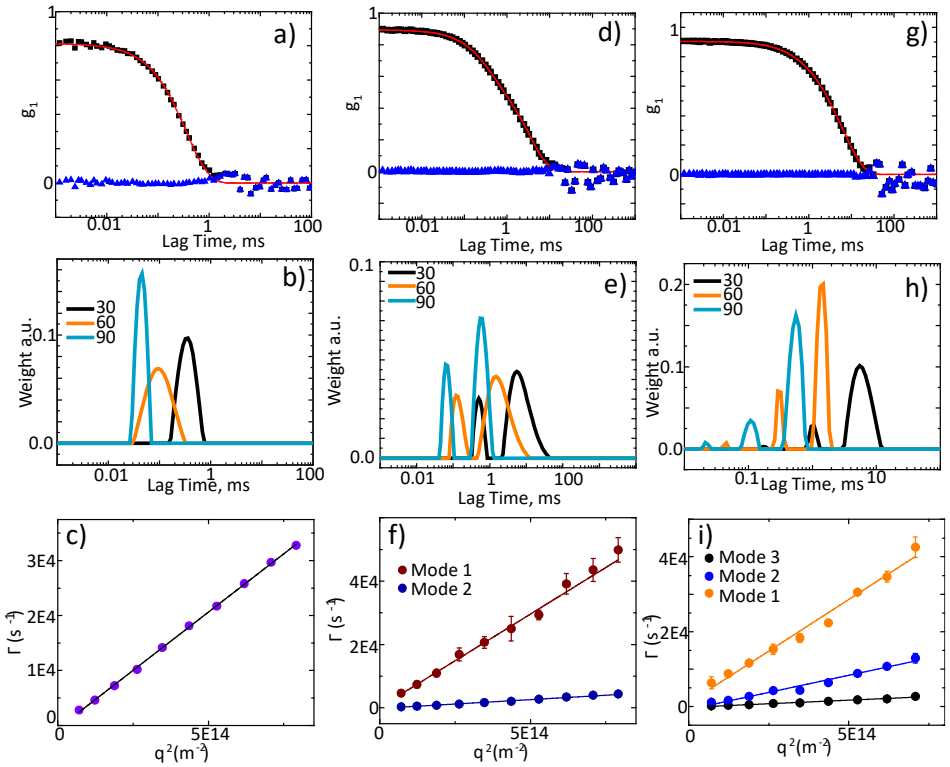

Figure 44.3. Dynamic light scattering analysis by CONTIN and multiple exponentials. a) Correlation function (black) g_1, single-exponential fit (red). The fit agrees well, as shown by the residuals (blue). b) CONTIN analysis of correlation function in a) for three different angles. In agreement with exponential fitting, we observe only one distribution of time scales for each angle. c) Inverse relaxation time Γ vs $q^2$is linear within the errors. From the slope, we calculate the diffusion coefficient. d) Correlation function (black) g_1, double-exponential fit (red). The fit agrees well, as shown by the residuals (blue). e) CONTIN analysis of correlation function in d) for three different angles. In agreement with exponential fitting, we observe two distributions of time scales for each angle. f) Inverse relaxation times Γ vs q^2 are linear within the errors for both modes. From the slope, we calculate the diffusion coefficients. g) Correlation function (black) g_1, triple-exponential fit (red). The fit agrees well, as shown by the residuals (blue). h) CONTIN analysis of correlation function in g) for three different angles. In agreement with exponential fitting, we observe three distribution of time scales for each angle. i) Inverse relaxation times Γ vs q^2 are linear within the errors for all three modes. From the slope, we calculate the diffusion coefficients.

In DLS, both of the above samples clearly exhibit only one diffusive mode (Figure A.3), yielding hydrodynamic radius R_h of 4 ± 0.33 nm and 5 nm, respectively, for PMPC107 and PMPC200. The shape factor, R_g/R_h , is 1.82 and 1.93 for PMPC107 and PMPC200, respectively. This suggests that the chain conformation is close to a swollen excluded volume chain. In fact, the ratio of R_g for these two polymers, $R_g(\mathrm{PMPC200})/R_g(\mathrm{PMPC107})$ is found to be equal to the

ratio $\left(\frac{M(\text{PMPC200})}{M(\text{PMPC107})}\right)^{0.6}$ = 1.4, showing that the size exponent ν for the radius of gyration is 0.6, as expected for a swollen coil in a good solvent.

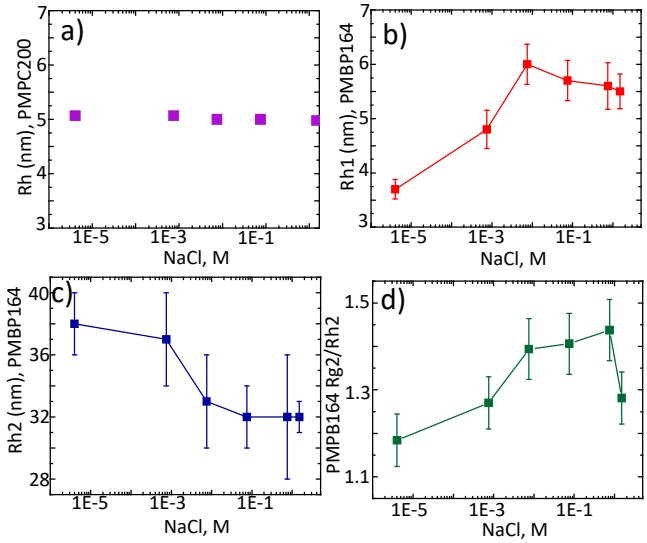

Figure 45.4. Comparison of PMPC and PMBP as a function of salt concentration. a) Hydrodynamic radius of 5 g/L PMPC200. b) R_{h1} of PMBP164 increases with salt concentration. c) Larger size scale R_{h2} of PMBP164 decreases with salt concentration. d) The shape factor, from Guinier analysis, showing more anisotropy at higher salt concentrations.

At 5 g/L concentration in water, we did not observe any PMPC aggregations with added NaCl concentrations from 4E-6 (corresponding to no added salt) to 1.5 M. As shown in Figure A.4, R_h is independent of salt concentration. This clearly suggests that there are no electrostatic effects contributing to the size and shape of PMPC in dilute solutions. In view of the size exponent ν being 0.6 and A_2 being positive, we conclude that PMPC is an unaggregated swollen excluded volume chain without significant intra-chain dipole associations. These results are consistent with the earlier results of Matsuda *et al.*[176]

PMBP (2), with its inverted dipole compared to PMPC, presented distinctly different aqueous solution behavior. Both PMBP164 and PMBP96 (D_p 164 and 96, respectively) form aggregates at 5 g/L concentration in water at 20 °C regardless of salt concentration (4E-6 to 1.5 M). In addition to its inverted dipole, the PMBP zwitterions feature *n*-butyl groups instead of the

methyl groups in PMPC. In principle, this additional hydrophobicity is expected to contribute to the solution structure of PMBP. Also, even for a single chain, intra-chain dipole interactions are expected to be enhanced by an effectively lower dielectric constant arising from the presence of butyl group at every monomer unit.

DLS revealed two distinct modes for both PMBP164 and PMBP96. Extreme care was taken in identifying these two modes to be diffusive, as shown in Figure A.3 (d-f). The resulting hydrodynamic radii Rh1 and Rh2 for PMBP164 at different salt concentrations are given in Table A.1 and Figures A.4b and A.4c. Rh1, corresponding to the un-aggregated polymer, is 3.7 nm for salt-free conditions and it increases continuously to 5.5 nm as the salt concentration is increased to 1.5 M NaCl, exhibiting 'anti-polyelectrolyte' behavior. In contrast, Rh2 is about an order of magnitude bigger, decreasing from 38 nm to 32 nm as the salt concentration is increased from 4E-6 to 1.5 M. In terms of percentage, this decrease is milder than the corresponding increase in Rh1 for the same salt concentration range. These results on PMBP164 are consistent with the results found by Niu *et al.* for polycarboxybetaine.[170]

Similar to the two sizes for PMBP164, salt free solutions of PMBP96 also show two sizes, Rh1 = 2.8 ± 0.5 nm and Rh2 = 33 ± 2 nm. Thus formation of aggregates is a common feature for both of these molecular weights.

The observed salt concentration dependence of Rh1 is consistent with intra-chain dipole-dipole interactions. At low salt concentrations (and presumably low local dielectric constant arising from the butyl group), the dipole-dipole interactions are strong. Addition of salt progressively screens the dipole-dipole interactions. As a result the coil radius increases as the salt concentration increases, as previously recorded in the literature. For the case of aggregates, represented by Rh2, the dipole-dipole interactions are both intra-chain and inter-chain. Since the number of dipolar groups participating in the assembly of aggregates is rather large, considerable

amount of added salt would be required to simultaneously screen all dipole pairs. For the range of salt concentration used in the present study, only a weak effect is seen in the size of the aggregate, again consistent with the conclusions of Niu *et al*.[170]

Table 4.1: Rh and Rg of PMBP164 (5 g/L in water) in varied NaCl salt concentrations

NaCl Conc.	Rh1 (nm)	Rh2 (nm)	Rg2 (nm)	Rg2/Rh2
0.4 μM	3.7 ± 0.2	38 ± 2	45 ± 1.5	1.18 ± 0.06
.75 mM	4.8 ± 0.4	37 ± 3	47 ± 2	1.27 ± 0.06
7.5 mM	6.0 ± 0.4	33 ± 3	46 ± 0.5	1.39 ± 0.07
75 mM	5.7 ± 0.4	32 ± 2	45 ± 0.5	1.40 ± 0.07
0.75 M	5.6 ± 0.4	32 ± 4	47 ± 1	1.47 ± 0.07
1.5 M	5.5 ± 0.3	32 ± 1	41 ± 1	1.28 ± 0.06

The average radius of gyration Rg2 of the aggregates was obtained from Guinier analysis (Figure A.2) and the results at different salt concentrations are included in Table A.1. From Rh2 and Rg2, we have determined the shape factor Rg2/Rh2 as shown in Table A.1 and Figure A.4d. The observed values of Rg2/Rh2 in the range of 1.18-1.47 are consistent with a spherical micro-gel-like aggregates.

Thus the behavior of PMBP is qualitatively different from that of PMPC. First, PMPC shows only one diffusive mode in DLS (corresponding to un-aggregated chains), whereas PMBP shows two distinct diffusive modes (corresponding to un-aggregated chains and aggregates). The hydrodynamic radius of PMPC does not depend on the salt concentration. On the other hand, the hydrodynamic radius of PMBP increases with salt concentration. These observations point to a significantly greater role of dipole-dipole correlations for PMPB relative to that of PMPC.

This behavior could be attributed to the local lower dielectric constant arising from the butyl group at every repeat unit of PMBP and thus enhancing the strength of the dipole pairs. The

dipole pairs, both intra-chain and inter-chain, are also responsible for the aggregate sizes represented by Rh2. The Rh2 depends only weakly on salt concentration. It would be fair to wonder whether the butyl groups play an additional role in forming the aggregates. It appears that this latter effect is weak, because Niu *et al.*[170] have reported observations on polycarboxybetaine, which does not contain any butyl or equivalent group at the side chain end, similar to ours.

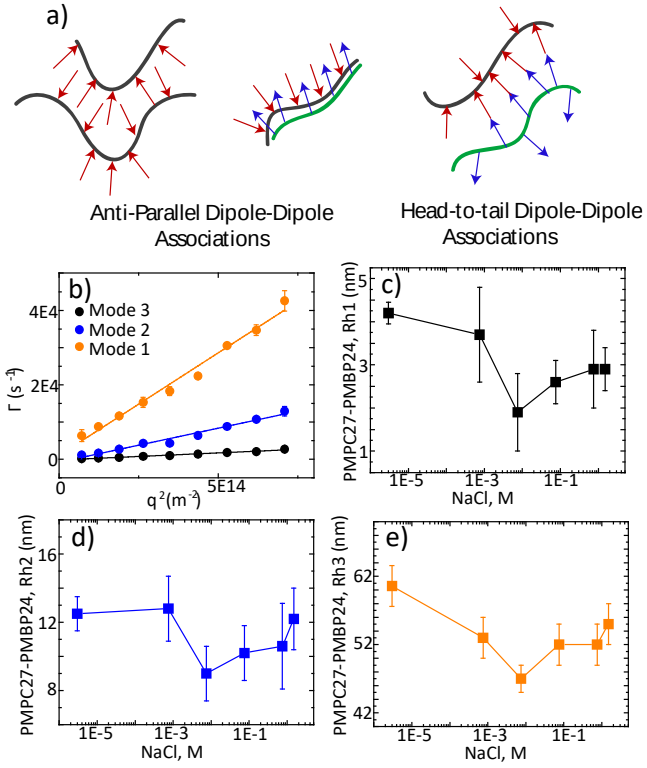

Figure 46.5. DLS of PMPC-*b*-PMBP diblocks in solution as a function of salt concentration. a) Schematic for two possible competing dipole-dipole interactions. The colors indicate PMBP (grey backbone) and PMPC (green backbone). b) Plot of the three distinct inverse decay times, Γ versus the square of the scattering angle q obtained by both CONTIN and multiple exponential analysis. The solid lines are linear fits. c) Rh1. d) Rh2. e) Rh3.

To investigate the interference by PMPC on the aggregation capacity of PMBP, we have studied the aqueous solutions of diblock copolymer PMPC27-*b*-PMBP24 ($D_{p,\,MPC}$ 27 and $D_{p,\,MBP}$ 24) at different NaCl concentrations ($4x10^{-6}$ M to 1.5 M) at 20 °C (Figure A.5). PMPC, being a swollen coil, might be expected to reduce PMBP aggregate size in a diblock copolymer form. Alternatively, the occurrence of inter-block complexation would lead to even larger aggregates.

Such complexation among the opposite dipoles of PMPC and PMBP may be envisaged as either head-to-tail or anti-parallel configurations, as depicted in Figure A.5a. Independent of the details of dipole correlations, we anticipated that the PMPC-block-PMBP copolymers would form a population of aggregates of certain average size in a mixture with unaggregated chains.

Unexpectedly, DLS experiments performed on the zwitterionic diblock copolymer samples gave clear evidence of three diffusive modes. The corresponding hydrodynamic radii for these three modes, Rh1, Rh2, and Rh3 are given in Figure A.5c-e. The values of Rh1, Rh2, and Rh3 are about 3 nm, 11 nm, and 55 nm, respectively. The smallest size is attributable to unaggregated diblock chains. The value of Rh1 is smaller than the values of un-aggregated PMPC and PMBP, in view of the lower molecular weight of the diblock copolymer. The dependence of Rh1 on salt concentration shows a non-monotonic behavior. It is seen from Figure A.5c that Rh1 first decreases as the salt concentration increases, but then it increases again when the salt concentration is increased further. The other two sizes must correspond to different aggregates. It was surprising to observe the two different populations of aggregates, each exhibiting non-monotonic dependence on salt concentration. As the salt concentration increases, the size first decreases and then increases as evident in Figure A.5d and A.5e. We note that Zimm plots and Guinier plots for this diblock copolymer system are not reliable due to the occurrence of three modes.

While dipole interactions are crucial for the formation of self-assembled aggregates, it is unclear how these result in two kinds of aggregates.

A.4 Conclusions

The role of segmental dipolar orientations on the self-assembly of polyzwitterions is investigated for the first time using DLS. For our experimental conditions, the solution properties of PMPC, PMBP, and PMPC-*b*-PMBP are clearly different. While we see no evidence for the

influence of dipolar interactions on the structure of PMPC in solutions of varied NaCl concentrations, dipole-dipole interactions lead to larger aggregate-like structures for PMBP and PMPC-*b*-PMBP. The origin for the presence of these interactions in PMBP solutions and their absence in PMPC solutions is unclear, but is likely due to internal factors such as the presence of hydrophobic groups on the phosphate ion of PMBP. The formation of two distinct aggregate size scales in PMPC-*b*-PMBP solutions was unexpected, and requires further investigation using simulations in conjunction with experiments. The solution properties of these dipole-rich macromolecules depend crucially on the ability of the dipoles to orient, and the local dielectric properties of the associations.

APPENDIX B

SYNTHESIS AND CHARACTERIZATION OF POLY(Mam-co-MAA-co-BMAC) POLYMER

B.1 Synthesis

For copolymerization of MAm, MAA and BMAC we have followed the procedure given in an earlier publication. MAA was distilled at 45 °C under reduced pressure (~ 10 torr) to remove the inhibitor and any impurities. A stock solution of AIBN/DMF (20 mg/mL) was made with 100 mg of AIBN and 5 mL of DMF. MAM (2.84 g, 33 mmol), MAA (0.78 g, 9.1 mmol) and BMAC (0.39 g, 1.35 mmol, 2.7 meq of vinyl groups) were added to a 20-mL glass vial equipped with a magnetic stir bar and were dissolved in 16 mL of DMF. The solution was purged with nitrogen at 22 °C for 20 min to remove the dissolved oxygen. The stock AIBN/DMF solution (0.5 mL, 10 mg) was syringed into the vial and the mixture was purged with nitrogen for another 20 min at 22 °C. The reaction was incubated at 60 °C for 18 h. The obtained solid was suspended in 200 mL of deionized (DI) water. The suspension was transferred to 4 50-mL centrifuge tubes and centrifuged at 2500 rpm for 10 min. The supernatant was decanted. This procedure was repeated three times to remove the DMF and was re-suspended in 200 mL of DI water. A 1 N NaOH solution was added to the suspension to adjust the pH to ~7.75 yielding a viscous mixture. Ten-molar excess of DTT (0.69 g, 4.5 mmol) was added to reduce the disulfide bonds. The mixture was stirred at 22 °C for 18 h and the suspension became clear and less viscous. An aliquot was taken and diluted to ~ 2 mg/mL for gel permeation chromatography (GPC) characterization. A 1 N HCl solution (20 mL) was then added to adjust the pH to ~ 3. A white solid was precipitated and separated via centrifuge (4000 rpm, 6 min). The product was washed four times with a nitrogen-purged 1 mM HCl aqueous solution followed by washing with a 1 mM HCl/ethanol solution. The copolymer was washed with a nitrogen-purged 1 mM HCl

aqueous solution again and lyophilized, yielding a white solid. The disulfide and thiol content in the copolymer was determined by the 2-nitro-5-thiosulfobenzonate (NTSB) assay. The thiol content for the copolymer in our study is 2%. As already described, the liquefied methacrylamide copolymer was exhaustively dialyzed to ensure that the toxic residual methacrylamide monomer is absent.

B.2 Thiolation of Gellan

The reaction for thiolation of gellan is taken from a previous work. A stock solution of gellan 1.33% (w/v) was prepared by dissolving required quantity of gellan (1 g, 1.55 meq of COOH) in 75 mL of water for 2 hours at 70 °C. The pH of the gellan solution was adjusted to 4.5 by adding a 1 N HCl aqueous solution and was cooled to 50 °C. EDC (0.62g, 3.3 mmol), NHS (0.093 g, 0.35mmol) and Cys (0.029 g, 0.26 mmol) were dissolved in 25 mL of water, and this solution was added to the gellan solution at 50 °C with stirring. The reaction mixture was continuously stirred and was cooled to room temperature after 60 minutes, resulting in a gel. Thereafter, the reaction was terminated by adding a 1 N NaOH solution, and the final pH was adjusted to 8-9. The excess EDC, NHS and Cys were removed from the reaction mixture by dialysis (MWCO: 6000-8000) in de-ionized (DI) H2O (three times). Then, the pH of the mixture was adjusted to 7.5 and the disulfide bonds were reduced with 5 molar excess of DTT for 3 hours yielding a solution. The excess DTT was removed by dialysis (MWCO: 6000-8000) in N_2-bubbled 1 mM HCl (4 L, six times). Finally, the samples were analyzed for the degree of thiolation of gellan by 2-nitro-5-thiosulfobenzonate (NTSB) assay.[32] For the gellan used in our investigation 6.4% of the acid groups are thiolated.

B.3 Sol-gel transition temperature

The sol-gel transition characteristic of each formulation of hydrogel was carried out using a Vilastic-3 oscillatory tube rheometer (Vilastic Scientific Inc., Austin, TX). A thermal scan with 5% constant shear strain and 1.0 Hz constant frequency was used to measure the transition point of the hydrogel by cooling the samples from 55 °C to 15 °C, equilibrating within 0.1 °C at each point as described. A 3x molar excess of glutathione was added to the samples during measurement to prevent disulfide cross-linking.

B.3 Chemical characterization

The characterization procedure for the MAm-MAA-BMAC gels is published earlier. The contents of BMAC were measured by ^{1}H NMR spectra. ^{1}H NMR spectra were obtained on a Varian Unity Inova 500 MHz (Palo Alto, CA). Copolymer samples were dissolved in D_2O (8 mg/mL). NaOD was used to enhance the solubility of the copolymers in D_2O. Each sample was scanned for 128 times at 25℃. The contents of BMAC in the copolymers were also tested by a disulfide test as described previously. Cystamine solutions with known concentrations (0.1-1.5 mM) were utilized as the standards.

Gel permeation chromatography (GPC) was performed with the reduced polymers. The GPC system employed a VE 1122 pump with a VE 7510 degasser (Viscotek/Malvern, Houston, TX, USA) that was equipped with a TDA302 triple detector system that measured the refractive index (RI), multi-angle laser light scattering, and viscosity. The column used was a G5000PWXL (Tosoh Biosep, Montgomeryville, PA, USA). Viscotek Omnisec software was used to calculate the RI area, weight-averaged molecular weight, intrinsic viscosity and hydrodynamic radius. Samples (100 µL) were injected at a concentration of 2 mg/mL. The column buffer (pH 7.6) contained 20 mM of sodium phosphate and the flow rate was 0.8 mL/min. The measurements were conducted at 37 °C. The results are shown in Table B.1.

Table 5.1: Rh and Rg of PMBP164 (5 g/L in water) in varied NaCl salt concentrations

mol% BMAC	Initiator:Monomer mole:mole	Mn (kDa)	Mw (kDa)	PDI	Yield %
2	1:770	237	348	1.47	84

BIBLIOGRAPHY

1. Swindle, K. E. & Ravi, N. Recent advances in polymeric vitreous substitutes. *Expert Rev. Ophthalmol.* **2,** 255–265 (2007).

2. Bishop, P. N. Structural macromolecules and supramolecular organisation of the vitreous gel. *Prog. Retin. Eye Res.* **19,** 323–344 (2000).

3. Sebag, J. & Balazs, E. A. Morphology and ultrastructure of human vitreous fibers. *Investig. Ophthalmol. Vis. Sci.* **30,** 1867–1871 (1989).

4. Los, L. I., Van der Worp, R. J., Van Luyn, M. J. A. & Hooymans, J. M. M. Age-related liquefaction of the human vitreous body: LM and TEM evaluation of the role of proteoglycans and collagen. *Investig. Ophthalmol. Vis. Sci.* **44,** 2828–2833 (2003).

5. Balazs, E. A.; Denlinger, J. L. in *The Eye* (ed. Davson, H.) (Academic Press, 1972).

6. Sebag, J. Age-related changes in human vitreous structure. *Graefe ' s Arch. Ophthalmol.* **225,** 89–93 (1987).

7. Flory, P. J. *Principles of Polymer Chemistry*. (Cornell University Press, 1953).

8. Flory, P. J.; Rhener, J. Statistical mechanics of crosslinked polymer networks i: Rubber-like elasticity. *J. Chem. Phys.* **11,** 521–526 (1943).

9. Flory, P. J.; Rhener, J. Statistical mechanics of crosslinked polymer networks ii: Swelling. *J. Chem. Phys.* **11,** (1943).

10. Katchalsky, A. Polyelectrolyte Gels in Salt Solutions. *J. Polym. Sci.* **XV,** 69–86 (1955).

11. Treloar, L. R. G. The Elasticity and Related Properties of Rubbers. *Rubber Chem. Technol.* **47,** 625–696 (1974).

12. Nisato, G., Skouri, R., Schosseler, F. & Munch, J. Elastic Behaviour of Salt-free Polyelectrolyte. 133–146 (1995).

13. Nisato, G., Schosseler, F. & Candau, S. J. Swelling equilibrium properties of partially charged gels: the effect of salt on the shear modulus. *Polym. Gels Networks* **4,** 481–498 (1996).

14. Horkay, F. *et al.* Osmotic swelling of polyacrylate hydrogels in physiological salt solutions. *Biomacromolecules* **1,** 84–90 (2000).

15. Hulmes, D. J., Wess, T. J., Prockop, D. J. & Fratzl, P. Radial packing, order, and disorder in collagen fibrils. *Biophys. J.* **68,** 1661–70 (1995).

16. Hulmes, D. J. S. Building Collagen Molecules, Fibrils, and Suprafibrillar Structures. *J. Structrual Biol.* **137,** 2–10 (2002).

17. Wood, G. C. & Keech, M. K. The formation of fibrils from collagen solutions 1. The effect of experimental conditions: kinetic and electron-microscope studies. *Biochem. J.* **75,** 588–598 (1960).

18. Engel, J. & Bächinger, H. P. Structure, stability and folding of the collagen triple helix. *Top. Curr. Chem.* **247,** 7–33 (2005).

19. Kadler, K. E., Holmes, D. F., Trotter, J. A. & Chapman, J. A. Collagen fibril formation. *J. Biochem.* **316,** 1–11 (1996).

20. Wenger, M. P. E., Bozec, L., Horton, M. A. & Mesquida, P. Mechanical properties of collagen fibrils. *Biophys. J.* **93,** 1255–63 (2007).

21. Van Der Rijt, J. A. J., Van Der Werf, K. O., Bennink, M. L., Dijkstra, P. J. & Feijen, J. Micromechanical testing of individual collagen fibrils. *Macromol. Biosci.* **6,** 699–702 (2006).

22. Christiansen, D. L., Huang, E. K. & Silver, F. H. Assembly of type I collagen: Fusion of fibril subunits and the influence of fibril diameter on mechanical properties. *Matrix Biol.* **19,** 409–420 (2000).

23. Buehler, M. J. Nature designs tough collagen: explaining the nanostructure of collagen fibrils. *Proc. Natl. Acad. Sci. U. S. A.* **103,** 12285–12290 (2006).

24. Roeder, B. A., Kokini, K., Sturgis, J. E., Robinson, J. P. & Voytik-Harbin, S. L. Tensile Mechanical Properties of Three-Dimensional Type I Collagen Extracellular Matrices With Varied Microstructure. *J. Biomech. Eng.* **124,** 214 (2002).

25. Cooper, a. Thermodynamic studies of the assembly in vitro of native collagen fibrils. *Biochem. J.* **118,** 355–365 (1970).

26. Keech, M. K. the Formation of Fibrils From Collagen Solutions. *J. Biophys. Biochem. Cytol.* **9,** 193–209 (1961).

27. Wallace, D. G. The relative contribution of electrostatic interactions to stabilization of collagen fibrils. *Biopolymers* **29,** 1015–1026

28. Venugopal, M. G. *et al.* Electrostatic interactions in collagen-like triple-helical peptides. *Biochemistry* **33,** 7948–7956 (1994).

29. Li, Y., Asadi, A., Monroe, M. R. & Douglas, E. P. pH effects on collagen fibrillogenesis in vitro: Electrostatic interactions and phosphate binding. *Mater. Sci. Eng. C* **29,** 1643–1649 (2009).

30. De Gennes, P. G. *Scaling Concepts in Polymer Physics*. (Cornell University Press, 1979).

31. Scott, J. E. Proteoglycan-fibrillar collagen interactions. *Biochem. J.* **252,** 313–323 (1988).

32. Morozova, S., Hamilton, P., Ravi, N. & Muthukumar, M. Development of a vitreous substitute: Incorporating charges and fibrous structures in synthetic hydrogel materials. *Macromolecules* **49,** 4619–4626 (2016).

33. Baino, F. Towards an ideal biomaterial for vitreous replacement: Historical overview and future trends. *Acta Biomater.* **7,** 921–935 (2011).

34. Chirila, T. V., Tahija, S., Hong, Y., Vijayasekaran, S. & Constable, I. J. *Synthetic Polymers as Materials for Artificial Vitreous Body: Review and Recent Advances*. *J Biomater Appl* **9,** (1994).

35. Chirila, T. V., Hing, Y., Dalton, P. D., Constable, A. J. & Refojo, M. F. The use of hydrophilic polymers as arfificial vitreous. *Prog. Polym. Sci.* **23,** 475–508 (1998).

36. Donati, S. *et al.* Vitreous substitutes: The present and the future. *Biomed Res. Int.* **2014,** (2014).

37. Kleinberg, T. T., Tzekov, R. T., Stein, L., Ravi, N. & Kaushal, S. Vitreous Substitutes: A Comprehensive Review. *Surv. Ophthalmol.* **56,** 300–323 (2011).

38. Lloyd, A. W., Faragher, R. G. A. & Denyer, S. P. Ocular biomaterials and implants. *Biomaterials* **22,** 769–785 (2001).

39. Stefánsson, E. Physiology of vitreous surgery. *Graefe's Arch. Clin. Exp. Ophthalmol.* **247,** 147–163 (2009).

40. Tanaka, F. *Polymer Physics: Applications to Molecular Association and Thermoreversible Gelation*. (Cambridge Univesity Press, 2011).

41. Skouri, R., Schosseler, F., Munch, J. P. & Candau, S. J. Swelling and Elastic Properties of Polyelectrolyte Gels. *Macromolecules* **28,** 197–210 (1995).

42. Oppermann, W. Swelling Behavior and Elastic Properties of Ionic Hydrogels. 159–170 (1992).

43. Zaroslov, Y. D., Philippova, O. E. & Khokhlov, A. R. Change of Elastic Modulus of Strongly Charged Hydrogels at the Collapse Transition. *Macromolecules* **32,** 1508–1513 (1999).

44. Barrat, J.-L., Joanny, J.-F. & Pincus, P. On the scattering properties of polyelectrolyte gels. *J. Phys. II* **2,** 1531–1544 (1992).

45. Rubinstein, M., Colby, R. H., Dobrynin, A. V. & Joanny, J.-F. Elastic modulus and equilibrium swelling of polyelectrolyte gels. *Macromolecules* **29,** 398–406 (1996).

46. Joosten, J. G. H., McCarthy, J. L. & Pusey, P. N. Dynamic and static light scattering by aqueous polyacrylamide gels. *Macromolecules* **24,** 6690–6699 (1991).

47. Tanaka, T., Hocker, L. O. & Benedek, G. B. Spectrum of light scattered from a viscoelastic gel *. *J. Chem. Phys.* **59,** 5151–5159 (1973).

48. Schosseler, F., Ilmain, F. & Candau, S. J. Structure and properties of partially neutralized poly(acrylic acid) gels. *Macromolecules* **24,** 225–234 (1991).

49. Råsmark, P. J., Koňák, Č., Štěpánek, P. & Elvingson, C. Fast internal dynamics in polyelectrolyte gels measured by dynamic light scattering. *Polym. Bull.* **54,** 335–342 (2005).

50. Anbergen, U. & Oppermann, W. Elasticity and swelling behavior of chemically crosslinked cellulose ethers in aqueous systems. *Polymer (Guildf).* **31,** 1854 (1990).

51. Gelman, R. a & Piez, K. a. Collagen fibril formation in vitro. A quasielastic light-scattering study of early stages. *J Biol Chem* **255,** 8098–8102 (1980).

52. Bella, J., Eaton, M., Brodsky, B. & Berman, H. M. Crystal and molecular structure of a collagen-like peptide at 1.9 A resolution. *Science (80-.).* **266,** 75–81 (1994).

53. Orgel, J. P. R. O. *et al.* The in situ supermolecular structure of type I collagen. *Structure* **9,** 1061–1069 (2001).

54. Antipova, O. & Orgel, J. P. R. O. In situ D-periodic molecular structure of type II collagen. *J. Biol. Chem.* **285,** 7087–7096 (2010).

55. White, S. W., Hulmes, D. J., Miller, A. & Timmins, P. A. Collagen-mineral axial relationship in calcified turkey leg tendon by X-ray and neutron diffraction. *Nature* **266,** 421–425 (1977).

56. Ottani, V., Martini, D., Franchi, M., Ruggeri, A. & Raspanti, M. Hierarchical structures in fibrillar collagens. *Micron* **33,** 587–596 (2002).

57. Brodsky, B. & Persikov, A. V. Molecular structureof the collagen triple helix. *Adv. Protein Chem.* **70,** 302–333 (2005).

58. Hofmann, H., Fietzek, P. P. & Kuhn, K. Comparative analysis of the sequences of the three collagen chains α1(I), α2 and α1(III): Functional and genetic aspects. *J. Mol. Biol.* **141,** 293–314 (1980).

59. Jones, Y. & Miller, A. Analysis of structural design features in collagen. *J. Mol. Biol.* **218,** 209–219 (1991).

60. Chan, V. C., Ramshaw, J. A. M., Kirkpatrick, A., Beck, K. & Brodsky, B. Positional preferences of ionizable residues in Gly-X-Y triplets of the collagen triple-helix. *J. Biol. Chem.* **272,** 31441–31446 (1997).

61. Katz, E. P. & David, C. W. Energetics of intrachain salt-linkage formation in collagen. *Biopolymers* **29,** 791–798

62. Li, S.-T., Golub, E. & Katz, E. P. Electrostatic side chain complementarity in collagen fibrils. *J. Mol. Biol.* **98,** 835–839 (1975).

63. Kadler, E. & Prockops, J. Assembly of Collagen Fibrils de Nouo by Cleavage of the Type I PC- Collagen with Procollagen C-Proteinase. *J. Biol. Chem.* **260,** 15696–15701 (1987).

64. Holmes, D. F. & Kadler, K. E. The 10+4 microfibril structure of thin cartilage fibrils. *Proc. Natl. Acad. Sci. U. S. A.* **103,** 17249–54 (2006).

65. Silver, F. H. & Birk, D. E. Molecular structure of collagen in solution: comparison of types I, II, III and V. *Int. J. Biol. Macromol.* **6,** (1984).

66. Birk, D. E. & Silver, F. H. Collagen fibrillogenesis in vitro: comparison of types I, II, and III. *Arch Biochem Biophys* **235,** 178–85 (1984).

67. Lee, S. & Piez, K. A. Type II collagen from lathyritic rat chondrosarcoma: preparation and in vitro fibril formation. *Coll. Relat. Res.* **3,** 89–103 (1983).

68. Cassel, J. Collagen aggregation phenomena. *Biopolymers1* **4,** 989–997 (1966).

69. Cassel, J. M. & Christensen, R. G. Volume change on formation of native collagen aggregate. *Biopolymers* **5,** 431–437 (1967).

70. Leikin, S., Rau, D. C. & Parsegian, V. a. Direct measurement of forces between self-assembled proteins: temperature-dependent exponential forces between collagen triple helices. *Proc. Natl. Acad. Sci. U. S. A.* **91,** 276–280 (1994).

71. Engel, J. & Prockop, D. J. Does bound water contribute to the stability of collagen [1]. *Matrix Biol.* **17,** 679–680 (1998).

72. Silver, F. H. A Molecular Model for Linear and Lateral Growth of Type I Collagen Fibrils. *Coll. Relat. Res.* **2,** 219–229 (1982).

73. Weinstock, a, King, P. C. & Wuthier, R. E. The ion-binding characteristics of reconstituted collagen. *Biochem. J.* **102,** 983–988 (1967).

74. Li, J., Suo, Z. & Vlassak, J. J. A model of ideal elastomeric gels for polyelectrolyte gels. *Soft Matter* **10,** 2582–90 (2014).

75. Venugopal, M. G., Ramshaw, J. A. M., Braswell, E., Zhu, D. & Brodsky, B. Electrostatic interactions in collagen-like triple-helical peptides. *Biochemistry* **33,** 7948–7956 (1994).

76. Tokita, M. & Tanaka, T. Friction coefficient of polymer networks of gels. *J. Chem. Phys.* **95,** 4613 (1991).

77. Suri, S. & Banerjee, R. Biophysical evaluation of vitreous humor, its constituents and substitutes. *Trends Biomater. Artif. Organs* **20,** 72–77 (2006).

78. Suri, S. & Banerjee, R. Inducing tissue specific tolerance in autoimmune disease with tolerogenic dendritic cells. *Clin. Exp. Rheumatol.* **33,** 97–103 (2015).

79. Jansson, P. & Lindber, B. Structural Studies of Gellan Gum, an Extracellular Polysaccharide elaborated by Pseudomonas elodea. *Carbohydr. Res.* **124,** 134–139 (1983).

80. Fialho, A. M. *et al.* Occurrence, production, and applications of gellan: Current state and perspectives. *Appl. Microbiol. Biotechnol.* **79,** 889–900 (2008).

81. Dentini, M. *et al.* Synthesis and physicochemical characterization of gellan gels. *Macromolecules* **34,** 1449–1453 (2001).

82. Gunning, a P., Kirby, a R., Ridout, M. J., Brownsey, G. J. & Morris, V. J. Investigation of Gellan Networks and Gels by Atomic Force Microscopy. *Macromolecules* **29,** 6791–6796 (1996).

83. Du, H., Hamilton, P., Reilly, M. & Ravi, N. Injectable in situ Physically and Chemically Crosslinkable Gellan Hydrogel. *Macromol. Biosci.* **12,** 952–961 (2012).

84. Swindle, K. E., Hamilton, P. D. & Ravi, N. In situ formation of hydrogels as vitreous substitutes: Viscoelastic comparison to porcine vitreous. *J. Biomed. Mater. Res. - Part A* **87,** 656–665 (2008).

85. Hyder A. Aliyar, †, Paul D. Hamilton, ‡ and & Nathan Ravi*, †,‡,§. Refilling of Ocular Lens Capsule with Copolymeric Hydrogel Containing Reversible Disulfide. 204–211 (2004). doi:10.1021/BM049574C

86. Aliyar, H. a. Synthesis of Polyacrylamide Nanogels by Intramolecular Disulfide Cross-linking. *J. Bioact. Compat. Polym.* **20,** 169–181 (2005).

87. Swindle-Reilly, K. E. *et al.* Rabbit study of an in situ forming hydrogel vitreous substitute. *Investig. Ophthalmol. Vis. Sci.* **50,** 4840–4846 (2009).

88. Liang, J., Struckhoff, J. J., Du, H., Hamilton, P. D. & Ravi, N. Synthesis and characterization of in situ forming anionic hydrogel as vitreous substitutes. *J. Biomed. Mater. Res. - Part B Appl. Biomater.* **0,** 1–13 (2016).

89. Carri, G. A. & Muthukumar, M. Attractive interactions and phase transitions in solutions of similarly charged rod-like polyelectrolytes. *J. Chem. Phys.* **111,** 1765–1777 (1999).

90. Muthukumar, M. *Polymer Translocation*. (CRC Press, 2011).

91. Muthukumar, M. Counterion adsorption theory of dilute polyelectrolyte solutions: Apparent molecular weight, second virial coefficient, and intermolecular structure factor. *J. Chem. Phys.* **137,** 1–13 (2012).

92. Hua, J., Mitra, M. K. & Muthukumar, M. Theory of volume transitions in polyelectrolyte gels. *J. Chem. Phys.* **136,** 134901 (2012).

93. Soumpasis, D. Debye–Hückel theory of model polyelectrolytes. *J. Chem. Phys.* **69,** 3190 (1978).

94. Kornyshev, A. A., Lee, D. J., Leikin, S. & Wynveen, A. Structure and interactions of biological helices. *Rev. Mod. Phys.* **79,** 943–996 (2007).

95. Skoog, D. A., West, D. M., Hollar, F. J. & Crouch, S. R. *Fundamentals of Analytical Chemistry 9th Edition*. (Brooks Cole, 2013).

96. Tanford, C. *Physical Chemistry of Macromolecules*. (John Wiley & Sons, Inc, 1961).

97. Doty, P. & Ehrlich, G. Polymeric electrolytes. *Annu. Rev. Phys. Chem.* **3,** 81–108 (1952).

98. Debye, P. & Hückel, E. 'Zur Theorie der Elektrolyte. I. Gefrierpunktserniedrigung und verwandte Erscheinungen' [The theory of electrolytes. I. Lowering of freezing point and related phenomena]. *Phys. Zeitschrift* **24,** 185–206 (1923).

99. Jackson, J. D. *Classic Electrodynamics*. (John Wiley & Sons, Inc, 1999).

100. Morozova, S., Hu, G., Emrick, T. & Muthukumar, M. Influence of Dipole Orientation on Solution Properties of Polyzwitterions. *ACS Macro Lett.* **5,** 118–122 (2016).

101. Dobrynin, A. V., Colby, R. H. & Rubinstein, M. Polyampholytes. *J. Polym. Sci. Part B Polym. Phys.* **42,** 3513–3538 (2004).

102. Higgs, P. & Joanny, J. Theory of polyampholyte solutions. *J. Chem. Phys.* **94,** 1543–1554 (1991).

103. Tanaka, T. *et al.* Phase Transitions in Ionic Gels. *Phys. Rev. Lett.* **45,** 1636–1639 (1980).

104. Horkay, F., Tasaki, I. & Basser, P. J. Effect of monovalent-divalent cation exchange on the swelling of polyacrylate hydrogels in physiological salt solutions. *Biomacromolecules* **2,** 195–199 (2001).

105. Donnan, F. G. 'Theorie der Membrangleichgewichte und Membranpotentiale bei Vorhandensein von nicht dialysierenden Elektrolyten. Ein Beitrag zur physikalisch-chemischen Physiologie' (The theory of membrane equilibrium and membrane potential in the presence of a non-dial. *Zeitschrift für Elektrochemie und Angew. Phys. Chemie* **17,** 572–581 (1911).

106. Doty, P. & Steiner, R. F. Light Scattering and Spectrophotometry of Colloidal Solutions. *J. Chem. Phys.* **18,** 1211 (1950).

107. Chu, B. Laser Light Scattering. *Annu. Rev. Phys. Chem.* **21,** 145–174 (1970).

108. Berne, B. J. & Pecora, R. *Dynamic Light Scattering*. (Courier Dover Publications, 2000).

109. Debye, P. Light scattering in solutions. *J. Appl. Phys.* **15,** 338–342 (1944).

110. Raman, C. V. A new radiation. *Proc. Indian Acad. Sci. - Sect. A* **37,** 333–341 (1953).

111. Debye, P. & Anacker, E. W. Micelle shape from dissymetry measurements. *J. Phys. Chem.* **55,** 644–655 (1951).

112. Carr, M. E. & Hermans, J. Size and density of fibrin fibers from turbidity. *Macromolecules* **11,** 46–50 (1978).

113. Zimm, B. H. The Scattering of Light and the Radial Distribution Function of High Polymer Solutions. *J. Chem. Phys.* **16,** 1093 (1948).

114. Zimm, B. H. Molecular Theory of the Scattering of Light in Fluids. *J. Chem. Phys.* **13,** 141–145 (1945).

115. Debye, P. Molecular-Weight Determination by Light Scattering. *J. Phys. Colloid Chem.* **18,** 18–32 (1946).

116. Mohr, B. G., Dobson, C. M., Garman, S. C. & Muthukumar, M. Electrostatic origin of in vitro aggregation of human ??-crystallin. *J. Chem. Phys.* **139,** (2013).

117. Kent, M. S., Tirrell, M. & Lodge, T. P. Solution Properties of Polymer Mixtures. *Macromolecules* **25,** 5383–5397 (1992).

118. Horkay, F., Basser, P., Hecht, A. & Geissler, E. Chondroitin Sulfate in Solution: Effects of Mono-and Divalent Salts. *Macromolecules* **45,** 2882–2890 (2012).

119. Horkay, F., Hecht, A.-M. & Geissler, E. Small Angle Neutron Scattering in Poly(vinyl alcohol) Hydrogels. *Macromolecules* **27,** 1795–1798 (1994).

120. Provencher, S. W. CONTIN: A general purpose constrained regularization program for inverting noisy linear algebraic and integral equations. *Comput. Phys. Commun.* **27,** 229–242 (1982).

121. Rochas, C. & Geissler, E. Measurement of Dynamic Light Scattering Intensity in Gels. 3–8 (2014).

122. Geissler, E. & Hecht, A. M. Dynamic Light Scattering from Gels in a Poor Solvents. *Le J. Phys.* **39,** 955–960 (1978).

123. Shibayama, M., Fujikawa, Y. & Nomura, S. Dynamic Light Scattering Study of Poly (N-isopropylacrylamide-co-acrylic acid) Gels. *Macromolecules* **29,** 6535–6540 (1996).

124. Shibayama, M. & Okamoto, M. Dynamic light scattering study on gelatin aqueous solutions and gels. *J. Chem. Phys.* **115,** 4285 (2001).

125. Norisuye, T., Tran-Cong-Miyata, Q. & Shibayama, M. Dynamic Inhomogeneities in Polymer Gels Investigated by Dynamic Light Scattering. *Macromolecules* **37,** 2944–2953 (2004).

126. Okamoto, T. Sol-gel transition of polysaccharide gellan gum. *Carbohydr. Polym.* **30,** 149–153 (1996).

127. McCoy, J. L. & Muthukumar, M. Dynamic Light Scattering Studies of Ionic and Nonionic Polymer Gels with Continuous and Discontinuous Volume Transitions. *J. Polym. Sci. Part B Polym. Phys.* **45,** 1390–1398 (2007).

128. Xue, J. Z., Pine, D. J., Milner, S. T., Wu, X. I. & Chaikin, P. M. Nonergodicity and light scattering from polymer gels. *Phys. Rev. A* **46,** 6550 (1992).

129. Fang, L. Q. & Berne, B. J. Dynamic Light-Scattering by Permanent Gels - Heterodyne and Nonergodic Medium Methods of Data Evaluation. *Macromolecules* **25,** 6897–6903 (1992).

130. Stuhrmann, H. B. Small-angle scattering of X-rays. *Progress In Crystal Growth And Characterization* **18,** 1–19 (1989).

131. Shibayama, M. *et al.* Small-Angle Neutron Scattering Study on Uniaxially Stretched Poly(N -isopropylacrylamide)−Clay Nanocomposite Gels. *Macromolecules* **38,** 10772–10781 (2005).

132. Chien, J. C. W. & Chang, E. P. Small-Angle Light Scattering of Reconstituted Collagen. *Macromolecules* **3321,** 610–617 (1972).

133. Prabhu, V. M., Muthukumar, M., Wignall, G. D. & Melnichenko, Y. B. Dimensions of polyelectrolyte chains and concentration fluctuations in semidilute solutions of sodium–poly(styrene sulfonate) as measured by small-angle neutron scattering. *Polymer (Guildf).* **42,** 8935–8946 (2001).

134. Higgins, J. S. & Benoit, H. C. *Polymers and Neutron Scattering*. (Clarendon Press, 1997).

135. Guinier, A. *X -Ray Diffraction In Crystals, Imperfect Crystals, and Amorphous Bodies*. (W. H. Freeman & Company, 1963).

136. Ornstein, L. & Zernike, F. Accidental deviations of density and opalescence at the critical point of a single substance. *Proc. Akad. Sci.(Amsterdam)* **XVII,** 793–806 (1914).

137. Casassa, E. F. Light Scattering from Very Long Rod-Like Particles and an Application to Polymerized Fibrinogen. *J. Chem. Phys.* **23,** 596 (1955).

138. Broersma, S. Rotational Diffusion Constant of a Cylindrical Particle. *J. Chem. Phys.* **32,** 1626–1631 (1960).

139. Ying, Q. & Chu, B. Overlap concentration of macromolecules in solution. *Macromolecules* **20,** 362–366 (1987).

140. Katchalsky, A., Lifson, S. & Eisenberg, H. Equation of Swelling for Polyelectrolyte Gels. *J.Polym.Sci.* **7,** 571–574 (1951).

141. Bergman, K., Elvingson, C., Hilborn, J., Svensk, G. & Bowden, T. Hyaluronic Acid Derivatives Prepared in Aqueous Media by. *Biomacromolecules* **8,** 2190–2195 (2007).

142. Borke, T., Winnik, F. M., Tenhu, H. & Hietala, S. Optimized triazine-mediated amidation for efficient and controlled functionalization of hyaluronic acid. *Carbohydr. Polym.* **116,** 42–50 (2015).

143. Timasheff, S. N. On the Mechanism of alpha-Chymotrypsin Dimerization. *Arch. Biochem. Biophys.* **132,** 165–169 (1969).

144. Hill, T. L. Approximate Calculation of the Electrostatic Free Energy of Nucleic Acids and Other Cylindrical Macromolecules. *Arch. Biochem. Biophys.* **57,** 229–239 (1955).

145. Lovelady, H. H., Shashidhara, S. & Matthews, W. G. Solvent specific persistence length of molecular type I collagen. *Biopolymers* **101,** 329–335 (2014).

146. Askeland, D. R., Fulay, P. P. & Wright, W. J. *Science and Engineering of Materials*. (CL Engineering, 2010).

147. Zimberlin, J. A., McManus, J. J. & Crosby, A. J. Cavitation rheology of the vitreous: mechanical properties of biological tissue. *Soft Matter* **6,** 3632 (2010).

148. Zimmerman, R. L. In vivo measurements of the viscoelasticity of the human vitreous humor. *Biophys. J.* **29,** 539–44 (1980).

149. Nickerson, C. S., Park, J., Kornfield, J. A. & Karageozian, H. Rheological properties of the vitreous and the role of hyaluronic acid. *J. Biomech.* **41,** 1840–1846 (2008).

150. Sharif-Kashani, P., Hubschman, J. P., Sassoon, D. & Pirouz Kavehpour, H. Rheology of the vitreous gel: Effects of macromolecule organization on the viscoelastic properties. *J. Biomech.* **44,** 419–423 (2011).

151. Matsuura, T. *et al.* Dynamic light scattering study on the calf vitreous body. *Macromolecules* **37,** 7784–7790 (2004).

152. Lowe, A. B. & McCormick, C. L. Synthesis and Solution Properties of Zwitterionic Polymers Synthesis and Solution Properties of Zwitterionic Polymers †. *Chem. Rev.* **102,** 4177–4190 (2002).

153. Kudaibergenov, S., Jaeger, W. & Laschewsky, A. Polymeric betaines: Synthesis, characterization, and application. *Adv. Polym. Sci.* **201,** 157–224 (2006).

154. Laschewsky, A. Structures and synthesis of zwitterionic polymers. *Polymers (Basel).* **6,** 1544–1601 (2014).

155. Gitlin, I., Carbeck, J. D. & Whitesides, G. M. Why are proteins charged? Networks of charge-charge interactions in proteins measured by charge ladders and capillary electrophoresis. *Angew. Chemie - Int. Ed.* **45,** 3022–3060 (2006).

156. Mary, P., Bendejacq, D. D., Labeau, M. P. & Dupuis, P. Reconciling low- and high-salt solution behavior of sulfobetaine polyzwitterions. *J. Phys. Chem. B* **111,** 7767–7777 (2007).

157. Shao, Q. *et al.* Differences in cationic and anionic charge densities dictate zwitterionic associations and stimuli responses. *J. Phys. Chem. B* **118,** 6956–6962 (2014).

158. Izumrudov, V. A., Zelikin, A. N., Zhiryakova, M. V, Jaeger, W. & Bohrisch, J. Interpolyelectrolyte reactions in solutions of polycarboxybetaines. *J. Phys. Chem. B* **107,** 7982–7986 (2003).

159. Izumrudov, V. A., Domashenko, N. I., Zhiryakova, M. V. & Davydova, O. V. Interpolyelectrolyte reactions in solutions of polycarboxybetaines, 2: Influence of alkyl spacer in the betaine moieties on complexing with polyanions. *J. Phys. Chem. B* **109,** 17391–17399 (2005).

160. Bohrisch, J., Grosche, O., Wendler, U., Jaeger, W. & Engelhardt, H. Electroosmotic mobility and aggregation phenomena of model polymers with permanent cationic groups. *Macromol.Chem.Phys.* **201,** 447–452 (2000).

161. Bohrisch, J., Schimmel, T., Engelhardt, H. & Jaeger, W. Charge interaction of synthetic polycarboxybetaines in bulk and solution. *Macromolecules* **35,** 4143–4149 (2002).

162. Bonte, N. & Laschewsky, A. Zwitterionic polymers with carbobetaine moieties. *Polymer (Guildf).* **37,** 2011–2019 (1996).

163. Favresse, P. & Laschewsky, A. New poly(carbobetaine)s made from zwitterionic diallylammonium monomers. *Macromol. Chem. Phys.* **200,** 887–895 (1999).

164. Wielema, T. A. & Engberts, J. B. F. N. Zwitterionic polymers I. Synthesis of novel series of poly(vinylsulphobetaines). Effect of structure of polymer on solubility in water. *Eur. Polym. J.* **23,** 947–950 (1987).

165. Huglin, M. B. & Rego, J. M. Influence of a Salt on Some Properties of Hydrophilic Methacrylate Hydrogels. *Macromolecules* **24,** 2556–2563 (1991).

166. Huglin, M. B. & Radwan, M. a. Unperturbed Dimensions of a Zwitterionic Polymet hacry late. *Polym. Int.* **26,** 97–104 (1991).

167. Schulz, D. N. *et al.* Phase behaviour and solution properties of sulphobetaine polymers. *Polymer (Guildf).* **27,** 1734–1742 (1986).

168. Salamone, J. C., Volksen, W., Olson, A. P. & Israel, S. C. Aqueous solution properties of a poly(vinyl imisazolium sulphobetaine). *Polymer (Guildf).* **19,** 1157 (1978).

169. Soto, V. M. M. & Galin, J. C. Poly(sulphopropylbetaines): 2. Dilute solution properties. *Polymer (Guildf).* **25,** 254 (1984).

170. Niu, A., Liaw, D. J., Sang, H. C. & Wu, C. Light-scattering study of a zwitterionic polycarboxybetaine in aqueous solution. *Macromolecules* **33,** 3492–3494 (2000).

171. Liaw, D.-J. & Huang, C.-C. Dilute solution properties of poly(3-dimethyl acryloyloxyethyl ammonium propiolactone). *Polymer (Guildf).* **38,** 6355–6362 (1997).

172. Georgiev, G. S. *et al.* Self-assembly, antipolyelectrolyte effect, nonbiofouling properties of polyzwitterions. *Biomacromolecules* **7,** 1329–1334 (2006).

173. Bredas, J. L., Chance, R. R. & Silbey, R. Head-head interactions in zwitterionic associating polymers. *Macromolecules* **21,** 1633–1639 (1988).

174. Tsonchev, S., Troisi, A., Schatz, G. C. & Ratner, M. A. All-atom numerical studies of self-assembly of zwitterionic peptide amphiphiles. *J. Phys. Chem. B* **108,** 15278–15284 (2004).

175. Hu, G., Parelkar, S. S. & Emrick, T. A facile approach to hydrophilic, reverse zwitterionic, choline phosphate polymers. *Polym. Chem.* **6,** 525–530 (2015).

176. Matsuda, Y., Kobayashi, M., Annaka, M., Ishihar, K. & Takahara, A. Dimension of Poly(2-methacryloyloxyethyl phosphorylcholine) in Aqueous Solutions with Various Ionic Strength.pdf. *Chem. Lett.* **35,** 1310–1311 (2006).